

POST-FAILURE BEHAVIOR OF WESTERLY GRANITE
AT ELEVATED TEMPERATURES

by

TENG-FONG WONG

Sc.B., Brown University
(1973)

M.S., Harvard University
(1976)

SUBMITTED IN PARTIAL FULFILLMENT
OF THE REQUIREMENTS FOR THE
DEGREE OF

DOCTOR OF PHILOSOPHY

at the

MASSACHUSETTS INSTITUTE OF TECHNOLOGY

November 1980

(i.e. February, 1981)

Signature of Author Signature redacted
Department of Earth and Planetary
Sciences, November 11, 1980

Certified by Signature redacted
Thesis Supervisor

Accepted by Signature redacted
Chairman, Department Graduate Committee

ARCHIVES
MASSACHUSETTS INSTITUTE
OF TECHNOLOGY

APR 2 1981

LIBRARIES

POST-FAILURE BEHAVIOR OF WESTERLY GRANITE
AT ELEVATED TEMPERATURES

by

TENG-FONG WONG

Submitted to the Department of Earth and Planetary Sciences
on November 11, 1980 in partial fulfillment of the
requirement for the degree of Doctor of Philosophy

ABSTRACT

Failure and post-failure behavior of Westerly granite were investigated at pressures up to 400 MPa and temperatures up to 700°C in an internally heated gas apparatus. 95 experiments were performed. For dry samples, the effects of temperature and strain rate on the failure stress are not significant relative to that of pressure. Some preliminary data indicate that the effect of water can be more pronounced at elevated temperature than at room temperature. At pressures above 80 MPa, crack morphology changes induced by thermal cracking has no effect on fracture strength.

Wawersik's manual control technique was adapted to high temperature, and a range of class I and II post-failure behavior was observed. Temperature was shown to be a stabilizing factor. Preliminary post-creep failure experiments show that the post-failure behavior depends on loading history. The behavior is more stable at a lower differential stress and a slower strain rate. The data are analyzed in terms of subcritical crack growth by stress corrosion. In light of previous room temperature post-failure and creep results and our analysis, we suggest that details of the post-failure curves are sensitive to statistical variation among samples.

Scanning electron microscope (SEM) observations were made on two suites of ion-thinned samples deformed at 400 MPa, 350°C and 250 MPa, 150°C. The latter suite includes 5 samples retrieved at different stages in the post-failure region. The pre-failure samples in both suites show numerous transgranular cracks at low angles (<15°) to maximum compression direction, similar to previous room temperature observation. We did, however, also observe many high-angle (>15°) transgranular cracks. The latter occurs in the feldspars and biotite as an array of parallel cracks with step-like propagation paths, suggesting that they are along cleavage planes. Similar features can not be seen in quartz, which does not have an easy cleavage.

The deformation in post-failure samples are localized. Typically a localized zone is comprised of a set of almost coplanar shear cracks at angles of 15° to 45° to maximum compression direction along favorably oriented grain boundaries or cleavages of feldspars and biotite. Elsewhere, axial crack arrays in quartz and microcline extend over entire grains forming slender columns. In plagioclase, complex crack networks link up with the pores. The crack arrays and networks interrupt the shear cracks, and act as "barriers" to the joining up of the shear cracks. A through-going fault is formed by coalescence of arrays and networks with the shear cracks, accompanied by extensive crushing into fine-grained gouge.

We conclude that elastic anisotropy and pore, as well as grain scale inhomogeneity can influence the development of stress-induced cracks. Consequently, the four minerals in Westerly granite behave differently during faulting, the failure mechanisms being dependent on both mineralogy and grain orientation. An attempt to isolate one single dominating mechanism as responsible for brittle faulting may not be a useful approach for this rock.

Values of the shear fracture energy \bar{G} were determined from the post-failure data following an integration scheme recently suggested by Rice. Values of \bar{G} so determined are of the order 10^4 Jm^{-2} . They compare more favorably with seismologically inferred \bar{G} values than laboratory measurements obtained in a tensile mode. Analysis of our data together with previous room temperature post-failure data show that the influence of temperature, pressure, and rock type can change \bar{G} by an order of magnitude.

On the basis of stereological analysis of our crack density data obtained under the SEM, we estimate the energy input for microcracking by multiplying the stress-induced crack surface area per unit volume and the tensile single crystal specific surface energy. We show that the microscopic observations are useful in supplying an independent estimate of a lower bound on the energy required for fracture.

From energetic consideration, we demonstrate how the four types of measurements: the estimation of shear fracture energy from seismological data, the laboratory study of post-failure behavior in triaxial compression, the measurement of tensile fracture energy of single crystal minerals, and the SEM observation of stress-induced microstructures should be related, and in what ways the different measurements should constrain one another.

Thesis supervisor: William F. Brace
Title: Professor of Geology

TABLE OF CONTENTS

	Page
TITLE PAGE	i
ABSTRACT	ii
TABLE OF CONTENTS	iv
ACKNOWLEDGEMENTS	vi
LIST OF TABLES	vii
LIST OF FIGURES	viii
INTRODUCTION	1
CHAPTER 1. EFFECTS OF TEMPERATURE AND PRESSURE ON FAILURE AND POST-FAILURE BEHAVIOR OF WESTERLY GRANITE	
Introduction	5
Apparatus and Procedure	7
Observation:	
Failure data	10
Post-failure data	12
Discussion:	
Effects of strain rate and moisture	14
Comparison with previous high temperature fracture data	18
Effects of temperature and pressure	20
Effect of thermal cracking	23
Post-failure behavior at elevated temperatures	24
Post-creep failure behavior and effect of loading history	27
The question of reproducibility	31
Conclusion	35
References	49
CHAPTER 2. MICROMECHANICS OF FAULTING IN WESTERLY GRANITE	
Introduction	55
Experimental procedure	57
Observation:	
Unstressed samples	64
The pre-failure samples	65
The samples close to failure	72
The post-failure samples	79
Discussion	
Influence of anisotropy on development of stress-induced cracks	85
The influence of pores in plagioclase	89
The effects of pressure and temperature ..	92
The micromechanics of faulting	95
The question of localization	100
Conclusion	101
References	112

CHAPTER 3. SHEAR FRACTURE ENERGY OF WESTERLY GRANITE FROM POST-FAILURE BEHAVIOR	
Introduction	118
Theory:	
Inelastic energy dissipation in pre- failure region	121
Determination of \underline{G} from post-failure curves	122
Estimation of the energy for stress- induced cracking	127
Determination of \underline{G} of earthquakes	129
Results:	
Pre-failure data	130
Post-failure data	131
Seismologically inferred values	135
Discussion:	
The role of microcracking in pre- and post-failure deformation	136
Comparison of laboratory measurements and seismologically inferred values of the shear fracture energy \underline{G}	138
Conclusion	142
References	164
APPENDIX. 1) Theoretical Analysis of The Effect of Anisotropy on Internal Stresses	104
2) A Summary of Useful Stereological Concepts.	145

ACKNOWLEDGMENT

I owe my greatest thanks to Bill Brace who suggested the problem. He allowed me the freedom to explore its various aspects, and provided patient guidance and valuable insights in all phases of this work. I would like to thank Joe Walsh for a number of key suggestions, and for being always ready to check my calculations. I am also indebted to Jim Rice for having formulated an elegant theory, and for several helpful discussions.

Conversations with and comments by K.Aki, Y.Caristan, B.Evans, D.Pollard and W.Wawersik were especially useful. Jock Hirst was particularly helpful and prompt in maintaining and repairing the high pressure equipments. He also helped in several of the post-failure experiments. I must also thank Madge Slavin for her patient handling of office details.

Kim Jones of the Harvard MRL electron microscopy facility has taught and helped me a lot on SEM work.

Lastly, I thank my wife, Kam-ling, for her patience and help throughout the preparation of this thesis.

LIST OF TABLES

Page

CHAPTER 1

Table 1-1	Failure stress at 400 MPa	37
Table 1-2	Other failure stress data	38

CHAPTER 2

Table 2-1	Pressure, temperature and stress conditions under which the SEM specimens were deformed ...	108
Table 2-2	Crack density data of three specimens deformed under different pressure, temperature condition	109
Table 2-3	The calculated induced stresses	110

CHAPTER 3

Table 3-1	Fracture energy G : A. Seismological estimate ..	150
	B. Laboratory:tension	150
Table 3-2	Laboratory measurement of shear fracture energy G	151
Table 3-3	Crack density data at 50 MPa, room temperature	153
Table 3-4	Crack density data at 250 MPa, 150°C	154
Table 3-5	Orientation dependence of crack intersections per unit length of 6 samples	155

LIST OF FIGURES

Page

CHAPTER 1

Figure 1-1	Specimen assembly and furnace	39
Figure 1-2	Variation of the fracture and frictional strength of Westerly granite ("vacuum dry") with temperature up to 700°C at constant pressure	40
Figure 1-3	Comparison of data on failure stress of Westerly granite at temperature and pressure	41
Figure 1-4	Comparison of pressure dependence of failure stresses at 150°C and at room temperature	42
Figure 1-5	Post-failure curves at a constant pressure of 250 MPa	43
Figure 1-6	Post-failure curves at a constant pressure of 80 MPa	44
Figure 1-7	Creep curve of a sample at 250 MPa, 350°C and at differential stress of about 97% of peak stress	45
Figure 1-8	Comparison of post-failure and post-creep failure behavior at 250 MPa, 350°C	46
Figure 1-9	Behavior of samples under creep and followed by fast loading at 350°C and at pressures of 80 MPa and 250 MPa	47
Figure 1-10	Post-failure behavior of a sample loaded along an irregular envelope below the failure envelope at 250 MPa, 350°C	48

CHAPTER 2

Figure 2-1	Axial stress-strain curve showing the stress history of the P-series samples	58
Figure 2-2	Axial stress-strain curve showing the stress history of the H-series samples	60
Figure 2-3	Axial stress-strain curve showing the stress history of the T-series samples	63
Figure 2-4	High-angle cleavage cracks in microcline	67
Figure 2-5	Complicated pattern of cracking in a microcline grain	69

	Page
Figure 2-6	An axial crack array in quartz 71
Figure 2-7	Shear cracks in a plagioclase grain 73
Figure 2-8	An axial crack array in microcline 74
Figure 2-9	Pore-emanated cracks in plagioclase 76
Figure 2-10	A set of cleavage cracks in biotite 77
Figure 2-11	Coalescence of a crack array in quartz and a crack network in plagioclase with a grain boundary to form a throughgoing fault 81
Figure 2-12	Coalescence of an axial crack array in microcline to form part of an incipient fault 82
Figure 2-13	A complex crack network in plagioclase 84
Figure 2-14	The calculated induced stresses 87
 CHAPTER 3	
Figure 3-1	a) Localization of an initially intact sample stress triaxially 159 b) Transformation of post-failure data to infer shear stress versus relative slip relation used in "slip-weakening " model 159
Figure 3-2	Slip-weakening model 160
Figure 3-3	Variation of shear fracture energy \underline{G} with temperature at constant pressure 161
Figure 3-4	Roses of the number of crack intersections per unit length for three pre-failure samples 162
Figure 3-5	Roses of the number of crack intersections per unit length for two post-failure samples 163

Brittle fracture is a fundamental process in rock mechanics. The traditional approach is to characterize the fracture event in a rock by the maximum stress a sample can sustain, namely, the failure stress. Studies of the post-failure behavior in the past decade show that the point of failure signals the initiation of a complex fracture process, and that a spectrum of post-failure behavior of different degree of stability can be observed by using a sufficiently stiff test machine or appropriate loading technique.

Both the failure and post-failure behavior have been investigated quite thoroughly at room temperature. The effects of confining pressure, strain rate, pore fluid, sample size and shape, and loading path have all been considered in varying degree of detail. To have a better understanding of crustal processes, it is of interest to consider the brittle fracture process in some detail under geologically interesting conditions. Crustal temperatures may reach 400°C or more, and yet only a few studies have been performed on fracture strength at elevated temperatures, and to our knowledge, no high temperature investigation of post-failure behavior has been made.

The experimental work reported in Chapter 1 is an effort to fill some of the gaps in this respect. In total 95 experiments were performed. We explored in some detail the effects of temperature and pressure on the fracture strength. A preliminary study of the effect of strain rate and pore water was also performed. We considered the dependence of

2

post-failure behavior on temperature, pressure and loading history. We attempt a systematic comparison of our results with those of previous work. The experimental data are interpreted in a conventional framework: the failure stress is taken to be the single quantity of physical interest, and the observed post-failure behavior is categorized based on whether the unloading stiffness is positive or negative.

It is well known that cracks and pores control the mechanical behavior in rocks. In spite of the advances made in electron microscope observations in the past decade of pre-existing and stress-induced microstructures, no clear picture has evolved concerning the micromechanics of faulting. In Chapter 2, we report on the first systematic scanning electron microscope study of a complete suite of samples deformed through the post-failure region. The samples were deformed at elevated temperatures; the temperature stabilizes the post-failure deformation and therefore it is easier to retrieve the samples. Furthermore, we show in Chapter 2 that several mechanisms which are known to be insignificant at room temperature are activated at high temperature, and we have been able to identify and observe in some detail a variety of failure mechanisms. These mechanisms are dependent on mineralogy and grain orientations. We attempt to interpret some of the observations by simple micromechanical models.

The ability to stabilize post-failure deformation hinges on resolving some delicate machine design problems.

It is not surprising therefore, that much of the attention has been focussed on the interaction problem between the sample and test machine, and that post-failure behavior is classified on the basis of the gross stiffness of a faulted sample. An important conclusion of our microscopic work in Chapter 2 is that brittle fracture is a localization process. Once a sample reaches the failure stress and strength begins to drop, the key physical processes take place principally along an incipient fault. The localized nature of post-failure deformation has to be taken into consideration in an analysis of the mechanics of faulting.

It turns out that, if we take such an approach, the post-failure behavior falls into the category of "slip-weakening" behavior, the analysis of the mechanics of which has been worked out in a number of recent theoretical work. Following Rice, we show in Chapter 3 how the parameter \underline{G} can be determined from post-failure stress-strain data. \underline{G} , the shear fracture energy, is a fundamental fracture mechanics quantity widely used in recent fault mechanics models. We show in Chapter 1 that post-failure curves are not uniquely determined by the two variables of stress and strain, and that the details are sensitive to time-dependent effects and sample variability. Until we have a thorough understanding of the interaction of all four variables (stress, strain, time, and sample statistics), \underline{G} probably is the most appropriate quantity

for characterizing the post-failure behavior, and definitely has more physical significance than the gross stiffness.

Similarly due to the lack of detailed knowledge concerning the faulting process of earthquakes, seismologists have spent a lot of effort on the estimation of \underline{G} rather than on the formidable task of understanding the detailed seismic source mechanism. In Chapter 3, we compare the experimental data for initially intact and pre-fractured samples with some of the seismologically inferred values of \underline{G} .

We also show how from energetic considerations, the macroscopic stress-strain data in Chapter 1, the microscopic crack density data in Chapter 2, and the measurements of fracture energy from different sources (single crystal and rock measurements, seismological estimates) should be related. Constraints on the energy budget for both pre- and post-failure deformation are discussed on the basis of these considerations.

The three chapters are intended to be read as separate units. Each chapter has a general introduction to the problem, a section on experimental procedure, a section on theory where appropriate, a discussion of results, a conclusion and a bibliography.

CHAPTER 1

EFFECTS OF TEMPERATURE AND PRESSURE ON FAILURE AND
POST-FAILURE BEHAVIOR OF WESTERLY GRANITE

INTRODUCTION

Brittle fracture of crustal rock is unquestionably one of the most studied processes in the laboratory. The failure stress or fracture strength is traditionally taken as the single parameter that is sufficient to characterize the fracture process; its dependence on confining pressure, strain rate, pore fluid, sample size and shape, and loading path have all been extensively investigated, and most of results were comprehensively reviewed by Paterson [1978]. Such studies, though essentially empirical in approach, provide much of the basis for applied rock mechanics in engineering and mining, as well as for the analysis of geologic faulting.

In order to have a better understanding of crustal processes, it is desirable to consider in greater detail the mechanics of brittle rock deformation. Even if one takes a phenomenological approach, to formulate a reasonable constitutive relation requires quite detailed knowledge of both pre- and post-failure behavior [Rudnicki & Rice, 1975] over the range of crustal pressure and temperature. In contrast to the vast number of studies on the effect of pressure carried out at room temperature, the combined effect of temperature and pressure on failure and post-failure behavior is

relatively unknown. We decided therefore to investigate this problem in some detail for one of the most studied rocks, Westerly granite.

It is generally accepted that in the brittle regime, the failure stress is relatively insensitive to temperature. The classic work of Griggs et al [1960] remains the major source of data, although the experiments were performed at only one pressure (500 MPa). With recent interests in rock mechanics application at high temperature environment for radioactive waste disposal and geothermal projects, it would be useful to be able to extrapolate to a lower pressure range. Studies on ceramics [Paterson & Weaver,1974], sedimentary rocks [Handin & Hager,1958], and serpentinite [Raleigh & Paterson,1963] show that as long as one stays in the brittle field, the temperature dependence of the failure stress is minimal, and is about the same at different fixed pressures. Recent data show, however, that extensive thermal cracking can occur at low pressure [van der Molen,1979; Wong & Brace,1979]. Would thermal cracking result in a stronger temperature dependence at the lower pressure range? The room temperature data suggest that effects of both strain rate and pore fluid are small [Brace & Jones,1974]. To what extent can we expect this to hold at high temperature?

Some post-failure studies have been done on silicate rocks under pressure [Wawersik & Brace,1971; Hojem et al., 1975; Rummel et al.,1978], but to our knowledge the effect

of temperature on post-failure behavior has not been investigated. Griggs et al's [1960] data indicate that the effect of temperature is to stabilize the post-failure response, and Wawersik & Brace [1971] show that for pressures up to 150 MPa at room temperature, both Westerly granite and Frederick diabase exhibit the unstable class II behavior. What are the roles of temperature and pressure on the transition from class II to class I behavior?

In an attempt to clarify some of these questions, we carried out a total of 95 experiments on the failure and post-failure deformation of Westerly granite at temperatures up to 700°C and pressures up to 400 MPa. The effects of temperature and pressure, and in lesser detail, the effects of strain rate and pore fluid were examined, and the results are presented below.

APPARATUS AND PROCEDURE

The apparatus and sample configuration are similar to those used by Goetze [1971] and Stesky et al [1974]. Two sample sizes were used. The specimens used at higher pressures and temperatures where we expected the failure process to be unstable were 35 mm long and 19 mm in diameter, and were jacketed directly with .32 mm thick annealed copper tube (Figure 1). Spacers of tungsten carbide were placed adjoining the specimen to smooth out the temperature distribution; they were followed

by polycrystalline alumina (Lucalox). A thermocouple reached the base of the sample through a hollow plug and an axial hole in the carbide and alumina spacers.

With the above set-up, the amount of fault displacement accompanying the instability may be sufficient to rupture the copper jacket if an unstable failure occurs; the pressure medium, which is argon at high pressure and temperature, will then rush in and blow the thermocouple out. Therefore, for pressure and temperature conditions at which such danger existed, the sample diameter was reduced to 16 mm, and a combination of graphite sleeve (1.3 mm thick) and copper jacket was used. As discussed by Brace & Byerlee [1970] and Stesky et al [1974] the graphite "blunts" the edge of the fault, and allows a sliding displacement up to about 2.5 mm. The graphite sleeve can support a finite differential stress [Paterson & Edmond, 1972], and the copper and graphite together contribute an error of about 5 MPa in the confining pressure and a maximum systematic error of 50 MPa in the failure stress [Stesky, 1975].

The sample was heated by an internally wound furnace surrounding the copper jacket. To minimize convection in the argon pressure medium, powdered boron nitride was placed between the copper jacket and the furnace wall. The temperature profile along the axis of the specimen was described by Goetze [1971] and Stesky et al [1974] for each of the

sample configurations; the maximum difference in temperature is about 25° at 700°C and less at lower temperatures. The temperature quoted for the experiments below are values at the bottom of the specimen recorded by the thermocouple.

Pressure was monitored with a Heise gauge, and maintained constant to within 1 MPa. All experiments were performed "drained" with the bottom end vented to atmosphere. The axial load was measured with an external load cell with a probable error of about 2%. The displacement was measured outside the pressure vessel with a differential transformer (DCDT) mounted between the moving piston and the fixed lower platen. Measurements were accurate to within 1%. Elastic distortion of the loading system was $.25 \text{ GNm}^{-1}$ ($2.5 \times 10^5 \text{ kg/cm}$); this was subtracted from the apparent displacement recorded from the DCDT for calculation of the axial strain.

The axial force was provided by a piston driven at a constant displacement rate by a ball-screw mechanism. For the fracture experiments, two displacement rates ($1.1 \times 10^{-2} \text{ mm s}^{-1}$ and $9.5 \times 10^{-4} \text{ mm s}^{-1}$) were used. The actual values of the strain rates change as the axial load is increased. For example, at 400 MPa and 600°C initial Young's modulus of the sample was 50 GPa, and hence the initial strain rates for a graphite-sleeved sample were $1.4 \times 10^{-4} \text{ s}^{-1}$ and $1.3 \times 10^{-5} \text{ s}^{-1}$ respectively; as the stress increased, the sample became softer and took up a larger proportion of the imposed deformation, such that at peak stress Young's modulus was essentially zero, and the corresponding strain rates had increased

to $3.1 \times 10^{-4} \text{ s}^{-1}$ and $2.7 \times 10^{-5} \text{ s}^{-1}$. For convenience, we shall refer to these strain rates simply as 10^{-4} s^{-1} and 10^{-5} s^{-1} respectively.

For the post-failure studies, the technique developed earlier [Wawersik & Brace, 1971] was used. Before failure, the piston advanced with the constant displacement rate of $9.5 \times 10^{-4} \text{ mm s}^{-1}$ (strain rate of about 10^{-5} s^{-1}). At and beyond the failure stress, the load was applied with the same rate with the operator closely watching the force-displacement display, and the load was quickly reduced manually as soon the strength showed sign of dropping. By repeating the process, one obtained from the envelope of these loading-unloading cycles a smooth curve in the post-failure region. Except for the experiments at high temperatures (above 420°C at 400 MPa, and 550°C at 250 MPa) for which the sample failed stably, the post-failure curves given here were from stress-strain envelopes obtained by this procedure.

OBSERVATION

Failure data

At a pressure up to 400 MPa and a temperature up to 700°C the differential stress supported by a sample always attained a maximum value, after which the sample either experienced a stable stress drop, or else fractured catastrophically. This

maximum value, defined to be the failure stress, was determined for Westerly granite in three series of experiments at fixed pressures (400 MPa, 250 MPa, and 80 MPa).

The samples deformed at 400 MPa were cored from the same block, but in an attempt to examine possible influence of moisture, two different procedures for sample preparation were used: the "room dry" samples were left exposed to laboratory atmosphere after being ground to the desired dimensions, whereas the "vacuum dry" samples (together with the graphite sleeves) were dried overnight *in vacuo* at about 80°C. Two strain rates were used (10^{-4} s^{-1} and 10^{-5} s^{-1}). Data for the "vacuum dry" samples were compiled in Table 1, and a comparison of the "room dry" and "vacuum dry" data is made in Figure 3. Also included in the same figure are data from Stesky et al [1974] at the same pressure for samples with "room dry" graphite sleeves, and data from Griggs et al [1960] and Tullis & Yund [1977] at 500 MPa.

Two series were deformed at the lower pressures of 250 MPa and 80 MPa. The data are compiled in Table 2 and plotted in Figure 2. To investigate the pressure dependence at a fixed temperature, additional runs were made at different pressures with temperature fixed at 150°C (Table 2). The data are compared with room temperature fracture data of Byerlee [1967] in Figure 4. Note that the data compiled in Table 2 are all for "vacuum dry" samples deformed at a single strain rate of 10^{-5} s^{-1} .

To explore the effects of thermal cracking, we performed three fracture experiments on samples pre-heated overnight in a furnace at room pressure. One sample was heated to 300°C and deformed to 400 MPa and 422°C; two samples were heated to 400°C and then deformed at room temperature and pressures of 80 MPa and 250 MPa respectively. Strain rate was 10^{-5} s^{-1} . The data are included in Tables 1 and 2, and Figure 2.

Post-failure data

Samples cored from a single block were used to study the post-failure behavior at two pressures (250 MPa and 80 MPa). All samples were pre-dried *in vacuo*. Data for four different temperatures at 250 MPa are shown in Figure 5. The two samples at 550°C and 668°C unloaded in a stable manner, but the manual control procedure discussed above had to be used at 150°C and 350°C to obtain the other two post-failure curves. Similiar data at 80 MPa, all obtained by manual control, are shown in Figure 6. A room temperature curve at 80 MPa obtained by Wawersik & Brace [1971] is also included for comparison.

In a preliminary attempt to explore time-dependent effects, four creep tests were performed at differential stress at or above 90% of the failure stress. The samples were all pre-dried *in vacuo*. Loading was at a rate of 10^{-5} s^{-1} up to a predetermined differential stress level, at which point the piston was stopped; the stress was maintained constant to within 1% as recorded on a chart recorder, and the piston reactivated whenever the stress had

relaxed below this range. (Because of experimental error and sample variability, the ratio of the creep stress to the failure stress can not be precisely determined. Some of the numbers quoted below were estimated by comparing the shape of the curves.)

The load-displacement curves of the creep tests are shown in Figures 8 and 9. The displacement shown is from the DCDT record directly, and it includes the elastic distortion of the testing machine. At 350°C and 250 MPa, a sample deformed at 10^{-5} s^{-1} failed explosively; the post-failure curve obtained by manual control (Figure 8) was almost vertical, indicating that if the sample stiffness was slightly higher, the unloading would have been stable. The testing system itself therefore acted as a sensitive reference for slight increases in the post-failure softening slope, and it was for this advantage that we chose this temperature and pressure for most of the creep tests.

One sample (PFW17) was allowed to creep at about 97% of the failure stress. The creep curve showed the typical primary, secondary, and tertiary stages (Figure 7). At some point along the tertiary creep stage, the relaxation was so fast that even with piston activated, the stress could not be restored to the fixed value, and it dropped to the residual value stably at a strain rate of 10^{-5} s^{-1} (Figure 8). No manual control was necessary to maintain stability during

the post-creep failure deformation; the unloading slope was therefore clearly gentler than the previous post-failure curve (of PFW 16) obtained by manual control. A second creep test (PFW 27) was first performed at 93% of the failure stress; the steady state creep rate was too slow, so the stress was increased to about 96% and held fixed again. The steady state creep rate was slower ($2 \times 10^{-7} \text{ s}^{-1}$) than before ($3 \times 10^{-6} \text{ s}^{-1}$), and the sample unloaded with a post-creep failure slope even gentler than PFW17 (Figure 8).

Two other tests at 350°C and pressures of 80 MPa and 250 MPa respectively were terminated before the tertiary creep stage was reached; the load was applied again at strain rate of 10^{-5} s^{-1} and both the specimens failed explosively at a differential stress close to that in the constant displacement rate experiments (Figure 9).

DISCUSSION

Effects of strain rate and moisture

Experiments were performed at different temperatures and a fixed pressure of 400 MPa to examine the possible influence of strain rate and moisture on the failure stress. The "vacuum dry" samples were deformed at two different strain rates and with different jacketing arrangements (Table 1). We have three sets of duplicate experiments at 350°C, 420°C,

and 550°C. If we consider all the 10^{-5}s^{-1} data in Figure 2 there seems to be a trend for the "vacuum dry" graphite-sleeved sample data (dark squares) to be slightly higher than those "vacuum dry" samples jacketed directly with copper (dark circles). If true, this is consistent with our previous error analysis that the graphite sleeve is capable of supporting a finite differential stress and can result in a systematic error. If one examines the copper-jacketed sample data in Figure 2 closely, one can also argue for a tendency for the 10^{-4}s^{-1} data (open circles) to be slightly higher than the 10^{-5}s^{-1} data (dark circles). Nevertheless, both effects, if real, would be within the experimental error. We conclude, therefore, that any strain rate sensitivity of the failure stress is also within our experimental error which, according to our error analyses and reproducibility, should be about 4% of the peak stress.

Brace & Martin[1968] examined the room temperature fracture strength of Westerly granite at 150 MPa over three decades of strain rate, and their "dry" data show an increase of about 10% in fracture strength for three orders of magnitude increase in strain rate. Our results here for "vacuum dry" samples indicate that the increase at elevated temperatures would at most be about the same; therefore, the strain rate sensitivity of the failure stress of Westerly granite is not strongly dependent on temperature up to about 600°C.

We made a parallel series of experiments on "room dry" samples. Though cored from the block, these samples presumably had more water trapped in cracks and pores since they had not been pre-dried *in vacuo*. These "room dry" samples were all directly jacketed in cooper without graphite sleeves. Most experiments were at 10^{-5} s^{-1} except three (220°C , 420°C , and 600°C) which were deformed at 10^{-4} s^{-1} . The data shown in Figure 3 indicate that effect of strain rate is also within experimental error. The reproducibility of the failure stress measurements are comparable for the two series, but the data began to diverge at about 200°C , with the "room dry" data (dark circles) consistently lower than the "vacuum dry" data (dark squares). The difference in the temperature range 400°C - 700°C is from 20% to 30% of the "vacuum dry" values.

Such a pronounced discrepancy is rather unexpected from room temperature data. Although Mizutani et al [1977] showed that the uniaxial strength of Ralston intrusive in a water saturated atmosphere is lower by about 40% when compared with a sample deformed at the same strain rate but under vacuum (10^{-8} torr), the effect is expected to be much smaller for samples pre-dried *in vacuo* but exposed to room atmosphere during the deformation process. At pressures to 69 MPa (10 ksi) Wawersik & Brown [1973] reported that strength of water saturated samples of Westerly granite is lower than the air dry data by about 10% at 10^{-5} s^{-1} ; at a higher pressure of 150 MPa and over three decades of strain rate (10^{-3} - 10^{-6} s^{-1}), Brace & Martin [1968] did

not observe any difference in strength between water saturated and "vacuum dry" Westerly granite within experimental error, which should be about 3%. We have no means of quantitatively estimating the water content in our "room dry" samples, but it is definitely less than that in water saturated samples, and yet we observed a substantial effect of up to 30% at elevated temperatures.

Our temperature and pressure range is probably too low for possible mechanisms such as "hydrolytic weakening" [Griggs, 1967] to be operative. The experiments were done by applying the confining pressure first, and then the temperature; if water was trapped in pores closed by pressure, the subsequent increase in temperature might then induce a high pore pressure, and the corresponding effective pressure decrease would result in a lower failure stress. To achieve such a large pore pressure effect, the permeability had to be low up to the point of failure.

On the other hand the strength reduction is also consistent with a "chemical" effect. Crack growth in quartz was shown to increase with partial pressure of water [Martin, 1972]. Crack tips in "room dry" samples have better access to water vapour, and therefore at a given differential stress and temperature, can extend at a faster rate. An unstable configuration can be reached at a lower stress, and hence the "room dry" samples would have lower failure stresses, the decrease being more pronounced at elevated temperatures because stress corrosion crack growth also increases with temperature .

It is clear from our preliminary data that the effect of water on strength is more complicated at elevated temperatures. However, lacking further experimental data, a more involved discussion of possible mechanisms would most probably be mere speculation. More experimental work under controlled conditions on the effects of water and pore pressure is necessary before we can clarify the roles played by water.

Comparison with previous high temperature fracture data

To our knowledge there were three previous studies on failure of Westerly granite at elevated temperatures, all at pressures higher than or equal to 400 MPa. Stesky et al [1974] performed seven fracture runs at 400 MPa and 10^{-5} s^{-1} . They used a set-up similar to ours, but their data at temperatures above 300°C consistently fell between our "vacuum dry" and "room dry" data. Their samples were "vacuum dry", but the graphite sleeves were "room dry". The discrepancy between the two sets of data can not be explained by variability from block to block: we performed two runs with "room dry" graphite sleeves, and the measurements are closer to Stesky et al's data than to our other data. Our measurements (at 400°C and 500°C) together with Stesky et al's data are plotted in Figure 3 as the "room dry graphite" data. The graphite we used has a porosity of about 25% and probably the strength reduction has to do with water squeezed out of the pores at temperature and subsequent weakening of the rock due to a pore pressure or a chemical effect.

Griggs et al [1960] reported ten experiments at 500 MPa (Figure 3). They used a gas apparatus, and the strain rate was $5 \times 10^{-4} \text{ s}^{-1}$, except for a sample at 500°C which was deformed at $2 \times 10^{-5} \text{ s}^{-1}$. The latter sample failed at 1.19 GPa, which fell between the two 10^{-4} s^{-1} data points at the same temperature (Figure 3), suggesting that the strain rate sensitivity was within experimental error.

One usually expects the failure stress to increase with confining pressure, and its pressure dependence to decrease with temperature. In this sense, Griggs et al's data do not agree with our "vacuum dry" data since above 400°C , their data are consistently lower although the confining pressure was higher. Sample variability can not explain the lower strength in samples from Griggs et al's block, since their measurements at 25°C is on the high side of existing room temperature fracture data [Ohnaka, 1973]. On the other hand, our "room dry" data seem to agree well with the trend at 500 MPa indicated by Griggs et al's data. The latter work did not report the drying procedure, but we know that the samples were not vented to the atmosphere. If the samples were not pre-dried *in vacuo*, they are closer to our "room dry" samples in water content, and the agreement is understandable. It should be reiterated, however, that the role of water needs to be explored more thoroughly before drawing further conclusions.

A third set of data were by Tullis & Yund [1977a,b] deformed at 500 MPa and 10^{-6} s^{-1} . The samples were dried by

heating to 300°C at room pressure. As shown in Figure 3, their data are lower than all the rest at 400 MPa or 500 MPa. It was pointed out that at temperatures below 700°C, the solid medium apparatus can not resolve the difference between the frictional sliding stress and the fracture stress [Tullis & Yund, 1977a]. It is unclear which quantity the data represent, and therefore no meaningful comparison can be made.

Effects of temperature and pressure

To explore the effects of temperature and pressure without possible complications of water, we performed three series of experiments at fixed pressures on "vacuum dry" samples (Figure 2). At a fixed confining pressure, the failure stress decreases with temperature. For the pressures we considered, the reduction in strength is relatively small, all within 20% at temperatures up to about 500°C beyond which, however, an accelerated downward trend was observed. Qualitatively, clear cut faults were observed in post-failure samples even at the higher temperatures, but the localized zones appeared to be wider at higher temperatures.

Temperature tends to stabilize post-failure behavior. At a fixed pressure, stable post-failure deformation without manual control is possible if temperature is increased to a point at which the softening slope equals the machine unloading stiffness. The transition temperatures for stable failure were above 660°C at 80 MPa, 450°-550°C at 250 MPa, and 350°-420°C at 400 MPa for our set-up, and 25°-300°C at 500 MPa for

Griggs et al's [1960] set-up. Comparing these transition temperature values, one would conclude that the effect of confining pressure is to stabilise the post-failure behavior. (Note that Griggs et al's result would not be relevant for this comparison if their testing system was much stiffer than ours).

A similar indication of this influence of the pressure is observed by considering the temperatures at which sharp changes occur in slope of the strength versus temperature curves in Figure 2: these temperatures characterize the transition from a regime of strong pressure dependence of failure stress to a regime of reduced pressure dependence and enhanced temperature sensitivity. As is evident from Figure 2, the effect of an increased pressure is to shift the transition to a lower temperature. Microscopic mechanisms responsible for such a transition from the brittle to "semi-brittle" field were studied in detail by Paterson & Weaver [1970] for polycrystalline MgO, and a review of relevant work in metallurgy and ceramics science was recently given by Carter & Kirby [1978]. Additional microstructural studies are needed to clarify the question of the extent to which some of these proposed "semi-brittle" mechanisms are applicable to crustal rocks at the temperature and pressure conditions of interest.

The effect of pressure is customarily interpreted in term of the Mohr-Coulomb criterion [Handin, 1969; Mogi, 1974; Paterson, 1978], and it is generally assumed that the criterion

holds for brittle fracture in general. To test possible temperature dependence, we performed a series of runs on samples from a single block at a fixed temperature of 150°C. The variation with pressure at 150°C is compared with the corresponding pressure dependence at room temperature (Byerlee, 1967) in Figure 4. Owing to block to block variability, the strength of our samples were higher than Byerlee's by about 50 MPa, but the pressure dependence was almost identical for the two sets of data at different temperatures. Mohr-Coulomb criterion has been applied to the analysis of fresh geologic fault [e.g. McGarr & Pollard, 1979] and of bounds on *in situ* stresses [Zoback & Zoback, 1980]; our data indicate that the extrapolation to elevated temperatures is justified. There are, however, several limiting factors rendering this criterion to be not very useful for placing bounds on crustal stresses in general; this question was recently discussed in some detail by Brace [1979].

The frictional strength data of Stesky et al [1974] at 400 MPa and 250 MPa are also outlined in Figure 3 for comparison, and as expected the frictional strength is in general lower than the fracture strength at temperatures up to 600°C, the implications of which were discussed in detail by Stesky et al [1974] and Stesky [1978]. No attempt was made to deform the samples to high strain since quite extensive qualitative observations and microscopic work have been made on faulted Westerly granite [Tullis & Yund, 1977b; Stesky, 1978].

Recent measurements of the thermal expansion of crystalline rocks under pressure [van der Molen, 1979; Wong & Brace, 1979] indicate that thermal cracking occurs when a rock is heated at sufficiently low pressures, and that the extent of thermal cracking increases with temperature at a given pressure. Can thermal cracking be responsible for the decrease in failure stress with temperature at a fixed confining pressure? The data shown in Figure 2 seem to argue against this: if thermal cracking is the mechanism responsible for strength reduction, we expect the failure stress to show a sharper decrease with temperature at lower pressures when the thermal cracking is more extensive. We do not detect this trend in our data; as a matter of fact, the 80 MPa data show a slightly smaller percentage decrease in strength with temperature.

As shown in Figure 2, the data of all three pre-heated samples agree with the "vacuum dry" data within experimental error. Judging from Simmons & Cooper's [1978] thermal cracking data, a large proportion of the thermally induced cracks in our pre-heated sample should still be open at a pressure of 80 MPa, and yet the failure stresses for the pre-heated and "vacuum dry" samples are identical. Failure stress is evidently not affected by the difference in initial crack morphology. Similar effect of thermal cracking on fracture strength was recently reported by Bauer & Johnson [1979] and Kurita et al [1980].

The experiment on a pre-heated sample at 422°C indicates that for "dry" deformation at high temperature, if the failure strength is the only parameter of interest, then pre-heating to 300°C serves the same purpose as drying *in vacuo*. The microscopic observation of the stressed samples, however, is complicated by thermal cracks induced by the pre-heating at room pressure [Sprunt & Brace, 1974; Bauer & Johnson, 1979]. Kurita et al [1980] also reported that for a sample pre-heated to 200°C, although no reduction in strength was observed at 150 MPa, the dilatant strain at failure was significantly higher.

Post-failure behavior at elevated temperatures

The post-failure behavior of rock was quite actively investigated in the past decade, and a number of papers has been published on the various aspects from stiff machine design to complete stress-strain curves, an incisive review of which was recently given by Paterson [1978]. Most of these studies interpreted the post-failure behavior in term of the classification proposed by Wawersik [Wawersik & Fairhurst, 1970] who showed that the post-failure response of certain rock types is so unstable that the load-displacement curves can actually turn over so far as to take on a positive slope. Wawersik categorized this type of behavior as class II, in contrast to the more stable class I behavior with persistently negative post-failure slope. Whereas class I behavior can be observed in a stable manner by using a sufficiently stiff machine, class II rocks will fail

explosively even if the stiffness is infinitely high, unless steps are taken to servo-control the testing machine either mechanically by a feedback loop [Hudson et al,1972] or manually [Wawersik & Brace,1971].

Up to now most investigations are on class I rocks in uniaxial compression. To our knowledge three groups have published results on post-failure behavior of silicate rocks in triaxial compression. Hojem et al [1975] studied the post-failure behavior of Witwatersrand quartzite at pressures up to 28 MPa by using an unusually stiff machine, and Rummel et al [1978] studied Fichtelgebirge granite at pressures up to 300 MPa using servo-control feedback; both rocks belong to class I within the range of pressures they considered. Class II behavior of Westerly granite and Frederick diabase was studied by Wawersik & Brace [1971] at pressures up to 150 MPa using manual control. As discussed by Paterson [1978], it is desirable that the displacement signal for servo-control feedback changes monotonically throughout an experiment, and for class II behavior the choice of such an optimum signal is difficult. The lateral strain has been used by Hudson et al [1971] and Sano [1978] as the feedback signal with variable degree of success in uniaxial compression of class II rocks. It is difficult to adapt similiar techniques in triaxial compression at elevated temperatures. As discussed above, we therefore chose to consider the post-failure behavior by adapting Wawersik's technique to high temperatures.

We attempted 19 post-failure experiments. 10 were

successful; the rest ended in unstable failure. Several experiments were deliberately terminated before the complete post-failure curves were obtained so as to retrieve the stress samples for scanning electron microscope observation [Chapter 2]. The results in Figures 5 and 6 show that at a fixed pressure, an increase in temperature results in an increase of the post-failure strain and a decrease in stress drop. Therefore the overall post-failure slope is gentler at higher temperatures. Nevertheless, the initial unloading behavior at lower pressures and temperatures still belongs to the unstable class II₂ (Figure 6).

The effect of pressure, however, can not be so simply generalized. There seems to be a trend for the higher pressure samples to experience slightly larger post-failure strain, but no systematic trend on stress drop was observed. Similarly Rummel et al's [1978] room temperature data on a class I granite over a comparable range of pressure seem not to exhibit any systematic dependence on pressure. Wawersik & Brace [1971] reported that at the highest pressure (150 MPa) the post-failure response was the most unstable; no general conclusion can be made of this observation since it can be due to either a sharper stress drop or a smaller post-failure strain during initial unloading at the higher pressure.

Post-creep failure behavior and effect of loading history

We performed four creep tests, the data of which are shown in Figures 7,8 and 9. Several aspects of the data are worth noting. First, they show that the observation by Wawersik [Wawersik & Brace,1971; Wawersik,1973] that the post-failure curve represents an approximate bounding curve for creep strain also applies at elevated temperatures. Some of the data (especially PFW 27) show larger creep strain at failure, but judging from similiar creep strain at failure data at room temperature [Wawersik & Brown,1973; Kranz,1980], this type of scatter is to be expected. Second, the post-failure curve is dependent on the loading history. The behavior is more stable at a lower fixed differential stress and strain rate.

The experiments were all done at a temperature of 350°C. Judging from transmission electron microscope studies of Westerly granite [Tullis & Yund,1977b; Stesky,1978], dislocation activity should not be significant at the pressure, temperature, and strain rate of our experiments. It is reasonable to assume that the creep mechanisms operative are brittle and similiar to those at room temperature [Wawersik,1973; Wawersik & Brown,1973; Kranz,1980].

One mechanism commonly proposed to explain brittle creep is stress corrosion. A detailed review of possible microscopic processes responsible for the phenomenon was recently given by Wiederhorn [1978]. The influence of

temperature, stress, and moisture on corrosion rate was studied by Martin [1972], and data on explicit relationship between the stress intensity factor (K_1) and crack velocity (v) in regime I was given recently by Atkinson [1979]. The effect of stress corrosion on the failure stress was qualitatively discussed in several articles [Martin, 1972; Rice, 1979a; Scholz & Koczynski, 1979; Rudnicki, 1980]. Rice's analysis is particularly pertinent here since he shows how earlier work of Wawersik & Brace [1971] similar to those shown in Figure 9 can be interpreted within a stress corrosion framework. We shall not repeat the details, but discuss below how the analysis can be extended to interpret some of our new results.

If stress corrosion is a significant mechanism, then the critical stress intensity factor K_{1c} should increase with crack velocity v (except possibly in the so called "regime II, where it remains constant [Wiederhorn, 1978]). If we make the plausible assumption that local microcrack K_1 values increase with the imposed differential stress, we can take that at rapid loading (say, at 10^{-5} s^{-1}) a higher threshold differential stress for significant crack growth is required. Of course, in this case once the critical value is reached, the crack growth proceeds at a relatively fast velocity. At a slower loading (say, creep at 10^{-7} s^{-1}) the reverse is true. A simplistic model can be formulated by assuming that a high critical stress intensity factor K_r

for rapid crack growth applies in our experiments at 10^{-5} s^{-1} , whereas a smaller critical value K_{S} for slow crack growth applies for the creep tests.

Because the creep deformation involves extensive crack growth at the smaller K_{S} , we can assume that relatively little crack growth is involved in constant displacement rate tests at fast loading until the failure stress is reached. Rice [1979a] suggested that the pre-failure sample in the latter case can, in this sense, be characterized as an "iso-crack network": the crack configuration is relatively unchanged and the local K_{I} values increase mainly owing to the higher imposed stress, and no significant crack growth occurs until the high K_{r} value is reached close to failure. At the post-failure stage, each time the failure envelope is reached, rapid crack growth modifies the "crack network", and subsequently a lower imposed stress is sufficient for the local stress intensity to reach K_{r} . The unloading and reloading are both rapid and at stresses below this new threshold, hence no significant crack growth results from the stress cycle, except at the end of the cycle when the post-failure envelope is reached again. An "iso-crack network" is therefore associated with each of the unloading-loading cycles.

Kranz & Scholz [1977] suggested that a "critical dilatant volume" exists at failure; within Rice's framework, this implies that a specimen at the failure point can

be characterized by an "iso-crack network" independent of the loading history. If we accept this assumption, then the difference in post-failure response shown in Figure 8 is to be interpreted as a manifestation of the stress dependence : at the same unloading rate, a sample characterized by the same "iso-crack network" fails more stably if the imposed stress level is lower. On the other hand, one can also argue that the slow creep deformation results in a crack configuration intrinsically different from that of fast loading. Paterson [1978], for example, suggested that the slower deformation rate may result in a "more generalized proliferation of cracking"; in which case, difference in post-failure behavior can also be attributed to changes in the "crack network" variable.

To resolve the question, more systematic experimental and microscopic work are necessary. Rice [1979b] has demonstrated how post-failure behavior may be interpreted by a slip-weakening model with two variables (shear stress and relative slip on the localized zone); our data here show that at a fixed temperature and pressure the post-failure behavior can not be uniquely characterized with such two variables if time-dependent effects are included. Various "strain softening" models for earthquake instability have been proposed in recent years, as reviewed by Stuart [1980]. What are the implications of the type of subtle changes in softening behavior we observed on these theoretical formulations? What are the microscopic mechanisms

behind the observed dependence on loading history and to what degree does it extend to other rock types? There definitely exists a need to explore these questions in greater detail.

The question of reproducibility

The manual control technique used by Wawersik and by us in this study may be suspect because of the possible influence of artificial effects of the operator. Wawersik & Brace [1971] investigated the question of reproducibility by performing a total of 25 uniaxial experiments on Westerly granite, and the two limiting curves were shown in their Figure 3 to demonstrate the degree of reproducibility. Hudson et al [1971] tried to obtain the complete uniaxial curve for a class II granite using servo-control feedback, but the radial strain gauge, the signal of which was used for feedback, broke half way and hence no complete post-failure curve is available for comparison. Sano [1978] used a modified approach and succeeded in obtaining the complete curves for the class II Oshima granite. Judging from the three curves shown (Oshima 450, 451 and 452) the reproducibility in Sano's study was not better than that of Wawersik & Brace [1971].

Our technique involves a number of unloading-loading cycles. Cyclic fatigue studies show that very large number of fast (1 Hz) loading cycles [Haimson, 1978] or a relatively small number of stress cycles at slower loading rate (1 MPas^{-1}) [Scholz & Koczyński, 1979] can have significant effect on the

fracture strength. Haimson [1978] emphasized the similiarity between dynamic fatigue and static creep, and from our discussion above, if stress corrosion is the mechanism, then each of our unloading-loading cycle will involve one "iso-crack network" and should not cause undue influence on reproducibility as long as the unloading and loading rates are relatively fast and if the strength envelope is reached for each of the cycles. We performed an experiment to dramatize the effect when these are violated (Figure 10). The sample PFW15 was loaded and unloaded with a large number of cycles (about 50) along an irregular envelope below the failure envelope at 10^{-5} s^{-1} . As expected, the curve traced out is intermediate between the post-failure (at constant strain rate) and post-creep failure curves.

The idea of an "iso-crack network" being preserved during an unloading-loading cycle is, of course, only an approximation. Each cycle involves hysteresis, possibly owing to energy dissipation mechanisms such as friction [Walsh, 1965; Scholz & Koczyński, 1979]. We judge from our data, however, that the hysteresis was within measurement error. This contribution from hysteresis should increase with the number of cycles, and precaution still needs to be made to reduce the number of unnecessary cycles.

If the two types of mechanisms discussed above are the sole causes, one would probably expect the reproducibility to improve with pressure. Zoback & Byerlee [1975] and Hadley [1976] observed that at sufficiently high pressures, the

hysteresis loops are stabilized after the first cycle. Haimson [1978] stressed the similiarity between cyclic fatigue and static creep behavior; since the latter mechanism has a rate which decreases with pressure [Wawersik & Brown, 1973; Kranz, 1980], one expects the former to be less significant at high pressure. Even though Scholz & Koczyński [1979] emphasized the possible difference between the two, they also concluded that the effect of pressure is to reduce the fatigue strain.

In contrast to the expected improvement in reproducibility with pressure, Wawersik & Brace [1971] pointed that it actually became worse with pressure, suggesting that a third factor may be involved. One plausible candidate is simply the statistical variability among rock samples. Although Westerly granite shows an unusually small scatter in fracture strenth of only a few percent, the statistical variation in the volumetric strain can be up to 20% [Costantino, 1978]. To reduce the statistical variation, the precaution is usually taken to prepare samples with dimensions more than ten times the grain size. This may be sufficient for pre-failure processes, but in the post-failure stage most of the deformation occurs in a localized zone which, according to microscope observations, can have width as small as one grain size. Hence as a rule of thumb, the zone samples a volume consisting of only about one-tenth the total number of grains in the sample. The statistical variation is therefore expected to wider. If we consider the post-failure process as an ensemble of discrete instability

events (failure of individual grains along the localized zone), then at a high pressure each of the grains fails with a large stress drop and small displacement, thereby exaggerating the variability in load-displacement record. This is consistent with the observation that the gross post-failure slopes of duplicate curves are usually the same, but the qualitative features of discrete, irregular alternations between steeply dropping parts and much flatter parts are highly variable among experiments performed under identical conditions [Wawersik & Brace, 1971; Sano, 1978].

We do not at present have the capability to explore this question further by extending the post-failure experiments to a wider range of sample dimensions, except possibly in an uniaxial configuration. Rice [1979b] has formulated a theory by which the shear fracture energy \underline{G} can be determined by an integral under the post-failure curve [Chapter 3]. \underline{G} is a fundamental fracture mechanics quantity widely used in theoretical fault models. The estimate of \underline{G} obtained by Rice's integration scheme is basically an average of the energy input over the entire localized zone: \underline{G} should therefore be not very sensitive to statistical variation among samples. If further studies conclude that indeed both time-dependent effects and sample variability can in general have significant influence on details of the post-failure stress-strain relation, then a global quantity such as \underline{G} may be the more appropriate parameter to use for characterization of post-failure behavior.

CONCLUSION

A number of general conclusions on the failure and post-failure behavior of Westerly granite can be made on the basis of the present study:

1. In the brittle regime, the failure stress at elevated temperatures depend strongly on pressure. At 150°C, the pressure dependence is almost identical to that at room temperature. Comparatively the temperature dependence of the failure stress is small. For the pressure range (up to 400 MPa) we consider, the reduction of fracture strength due to temperature increase up to 500°C is less than 20% of the room temperature failure stress.
2. At temperature up to 600°C, the strain rate sensitivity of the strength of dry samples is low. Our data indicate a reduction in strength of less than 4% per decade decrease of strain rate.
3. The effect of water on strength reduction is more pronounced at elevated temperatures than at room temperature.
4. At pressures above or equal to 80 MPa, crack morphology change induced by thermal cracking has no consequence on the failure stress value. Furthermore, the slight temperature dependence of brittle fracture strength can not be adequately explained by thermal cracking.
5. The effect of temperature is to stabilize the post-failure behavior. At 80 MPa, 150°C the initial unloading behavior still belongs to the unstable class II; as temperature or pressure is increased, a transition to class I is observed.

6. Post-failure behavior is dependent on loading history. The behavior is more stable at a lower fixed differential stress and a slower strain rate. Analysis of our data in light of published work on room temperature post-failure and creep behavior indicate that details of the post-failure curve are sensitive to statistical variation among samples.

TABLE I

Failure stress at 400 MPa ("vacuum dry")

Sample	T (°C)	Failure stress ($\sigma_1 - \sigma_3$, GPa)	Jacket *	Strain_rate (log s ⁻¹)	Comments
HTW54	20	1.66	G	-5	
HTW50	154	1.62	G	-5	
HTW49	352	1.53	G	-5	
HTW43	353	1.54	G	-5	
HTW48	355	1.50	C	-5	
HTW36	425	1.50	C	-4	
HTW33	426	1.46	C	-5	
HTW47	422	1.49	C	-5	Preheated to 300°C at room pressure
HTW35	499	1.44	G	-5	
HTW46	503	1.43	C	-4	
HTW30	507	1.34	C	-5	
HTW 0	550	1.30	C		Manual loading
HTW44	580	1.26	G	-5	
HTW45	611	1.18	C	-4	
HTW27	660	1.14	C	-5	
HTW28	680	1.03	C	-5	

* G:graphite sleeved and copper jacketed

C:directly copper jacketed

TABLE II

Other failure stress data ("vacuum dry")

Sample	Pressure (σ_3 , MPa)	T (°C)	Failure stress ($\sigma_1 - \sigma_3$, GPa)	Comments
MTW11	250	20	1.34	
MTW12	250	20	1.29	Preheated to 400°C at room pressure
MTW 1	250	155	1.29	
MTW 4	250	302	1.20	
MTW 5	250	455	1.04	
MTW 7	250	551	1.03	
MTW 9	250	611	0.74	
MTW 8	250	668	0.62	Directly jacketed in copper
PFW26	80	20	0.79	
PFW29	80	20	0.81	Preheated to 400°C at room pressure
PFW22	80	150	0.74	
PFW23	80	350	0.70	
PFW28	80	551	0.66	
PFW30	80	659	0.59	
HTW53	50	151	0.71	
HTW52	100	151	0.92	
HTW51	150	153	1.15	

Note: all experiments were performed on graphite-sleeved samples
at 10^{-5} s^{-1} unless otherwise noted.

FIGURE CAPTIONS

Figure 1. Specimen assembly and furnace.

Figure 2. The variation of fracture and frictional strength of Westerly granite ("vacuum dry") with temperature at fixed pressures:

- graphite-sleeved, 10^{-5} s^{-1}
- directly copper-jacketed, 10^{-5} s^{-1}
- directly copper-jacketed, 10^{-4} s^{-1}
- △ directly copper-jacketed, manual loading
- ▼ pre-heated.

Typical error bars are shown.

Figure 3. Comparison of data on failure stresses of Westerly granite at temperature and pressure.

Figure 4. Comparison of pressure dependence of failure stresses at 150°C and at room temperature. Typical error bars are shown.

Figure 5. Post-failure curves of Westerly granite at a constant pressure of 250 MPa. Data for 150° and 350°C were both obtained by manual control.

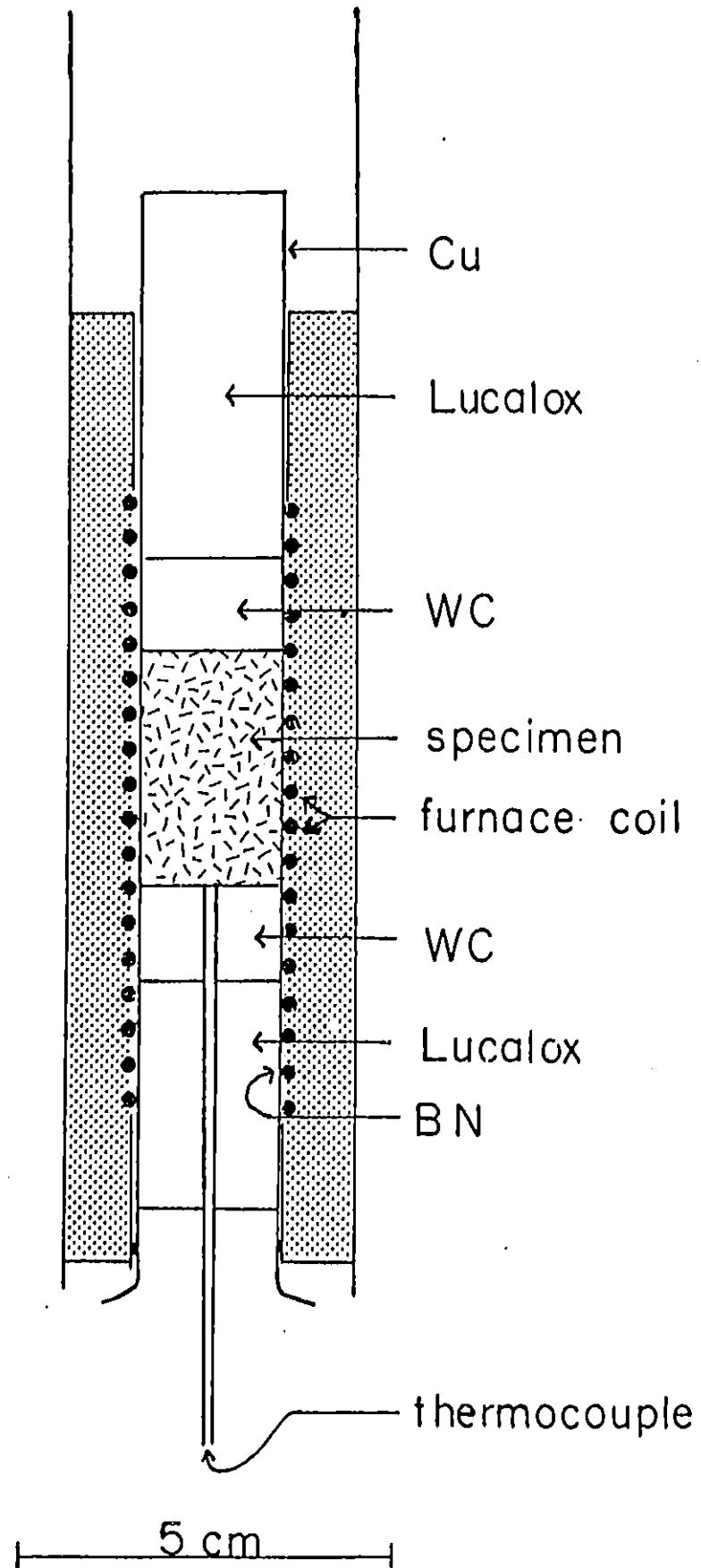
Figure 6. Post-failure curves of Westerly granite at a constant pressure of 80 MPa, all obtained by manual control. The room temperature curve is from Wawersik & Brace [1971].

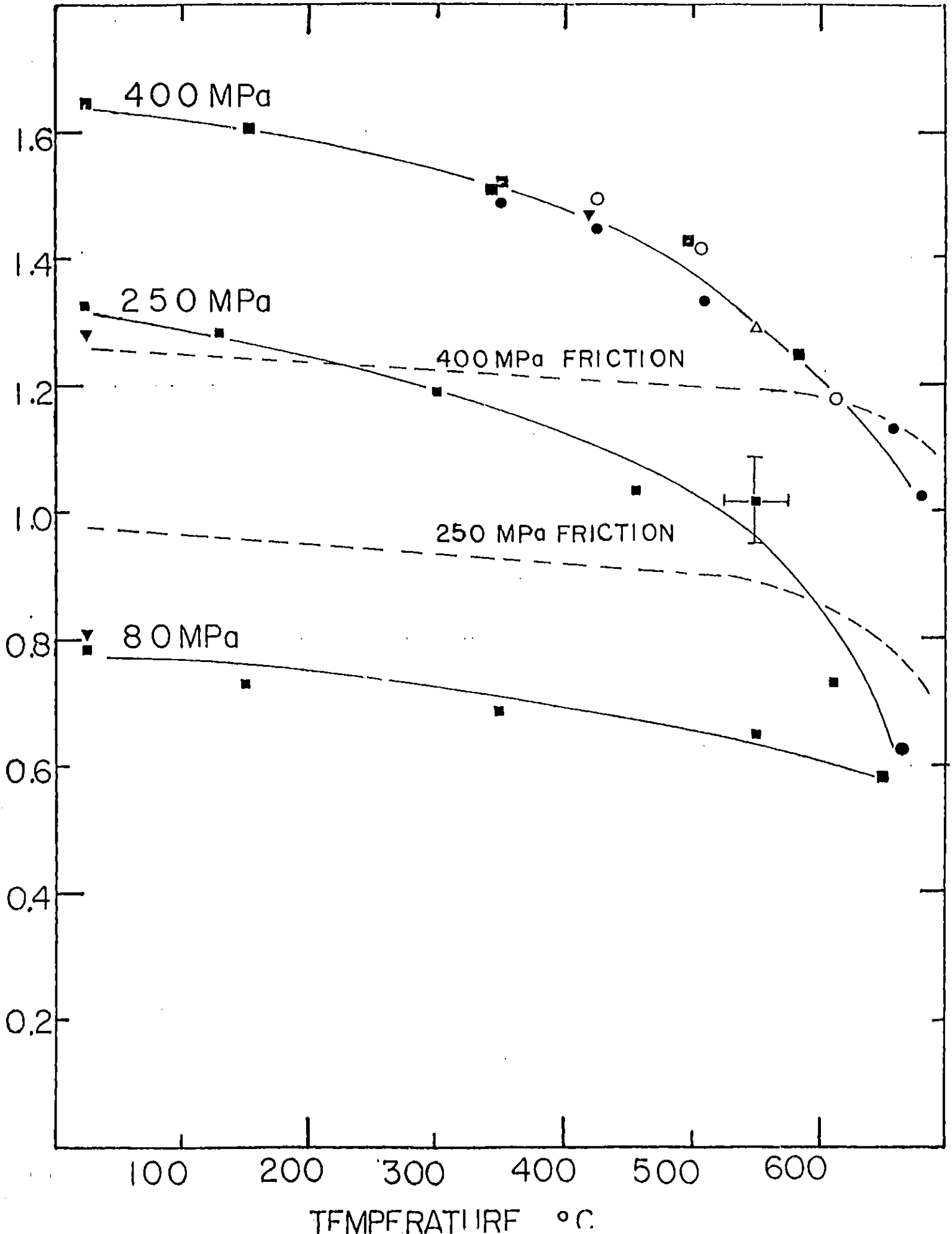
Figure 7. Creep curve of a sample at 250 MPa, 350°C and at a differential stress about 97% of the peak stress.

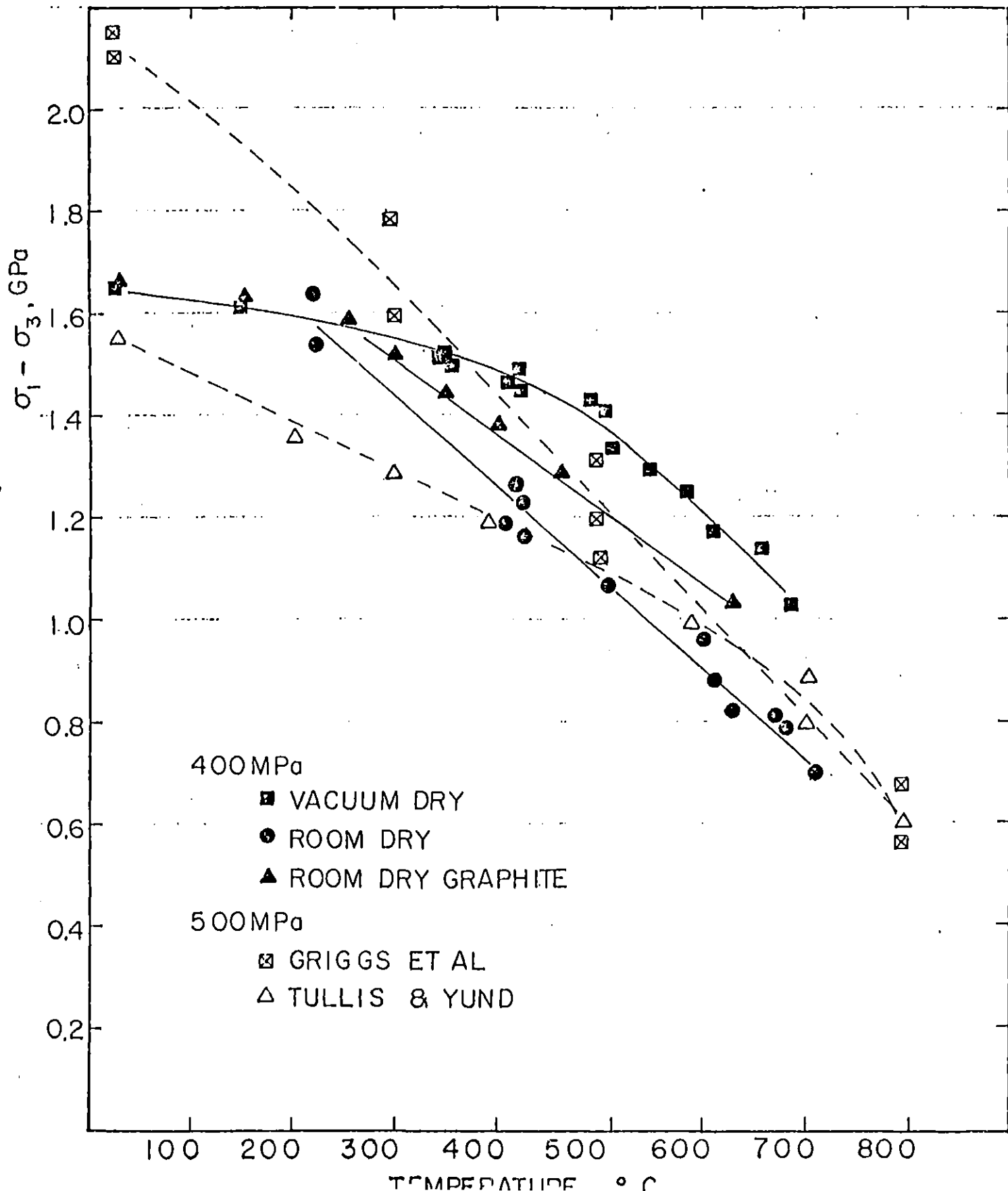
Figure 8. Comparison of post-failure and post-creep failure behavior at 250 MPa, 350°C . Note what is shown is the apparent displacement which includes elastic distortion of the test machine.

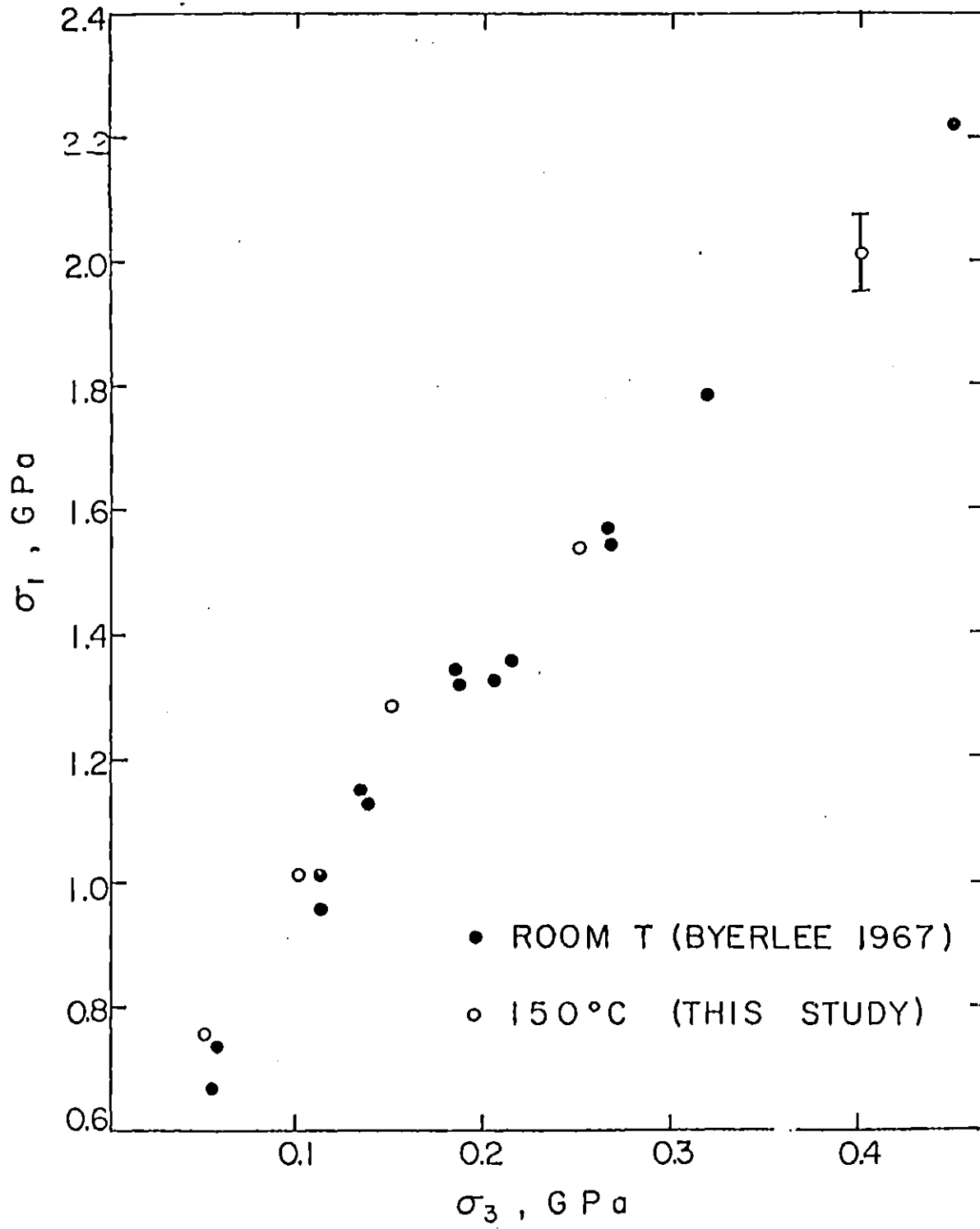
Figure 9. Behavior of samples first under creep and then rapid loading at 350°C , and at pressures of 80 MPa and 250 MPa.

Figure 10. Post-failure behavior of a sample loaded along an irregular envelope below the failure envelope at 250 MPa, 350°C . The two curves for PFW16 and PFW27 in Figure 8 are reproduced here for comparison.









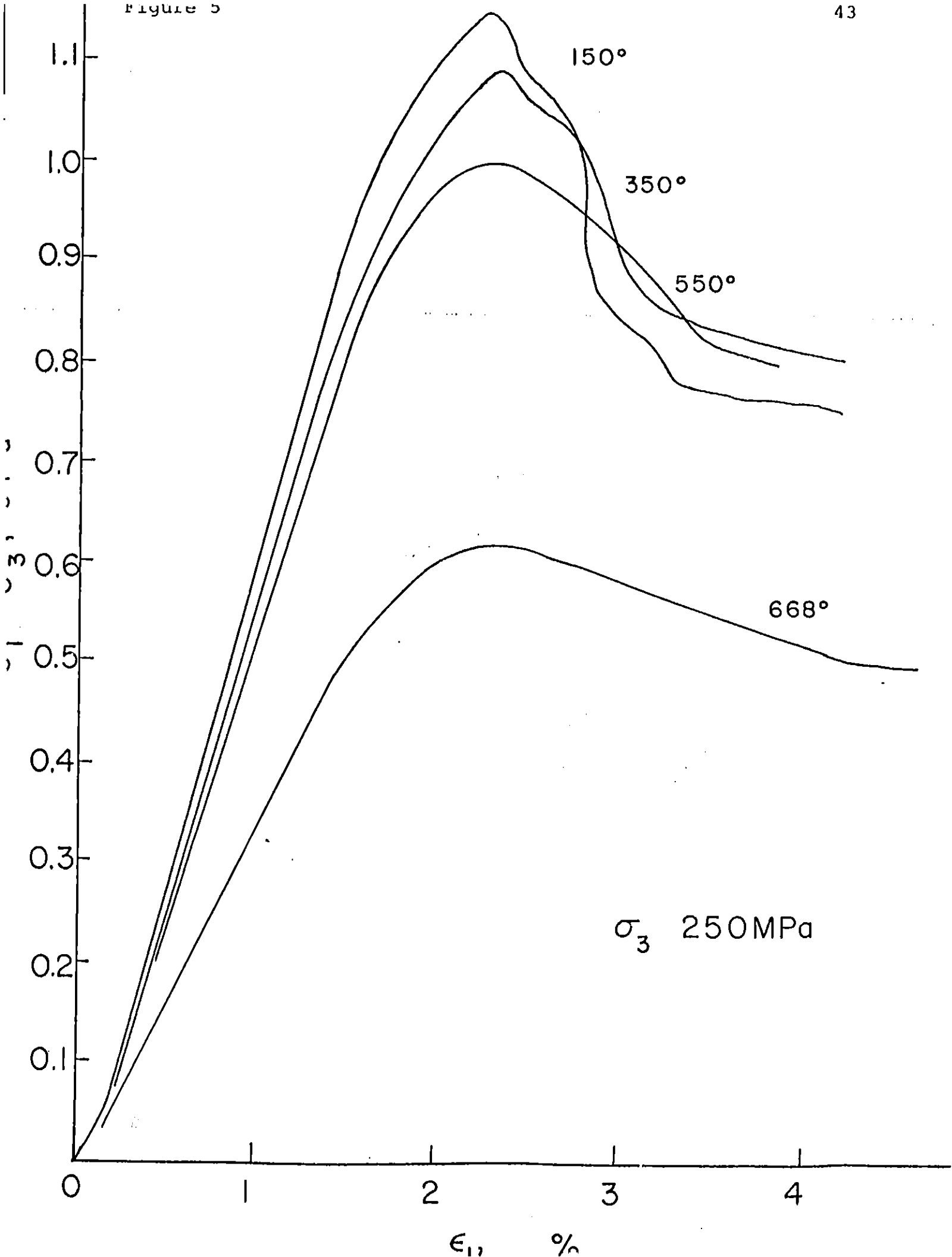
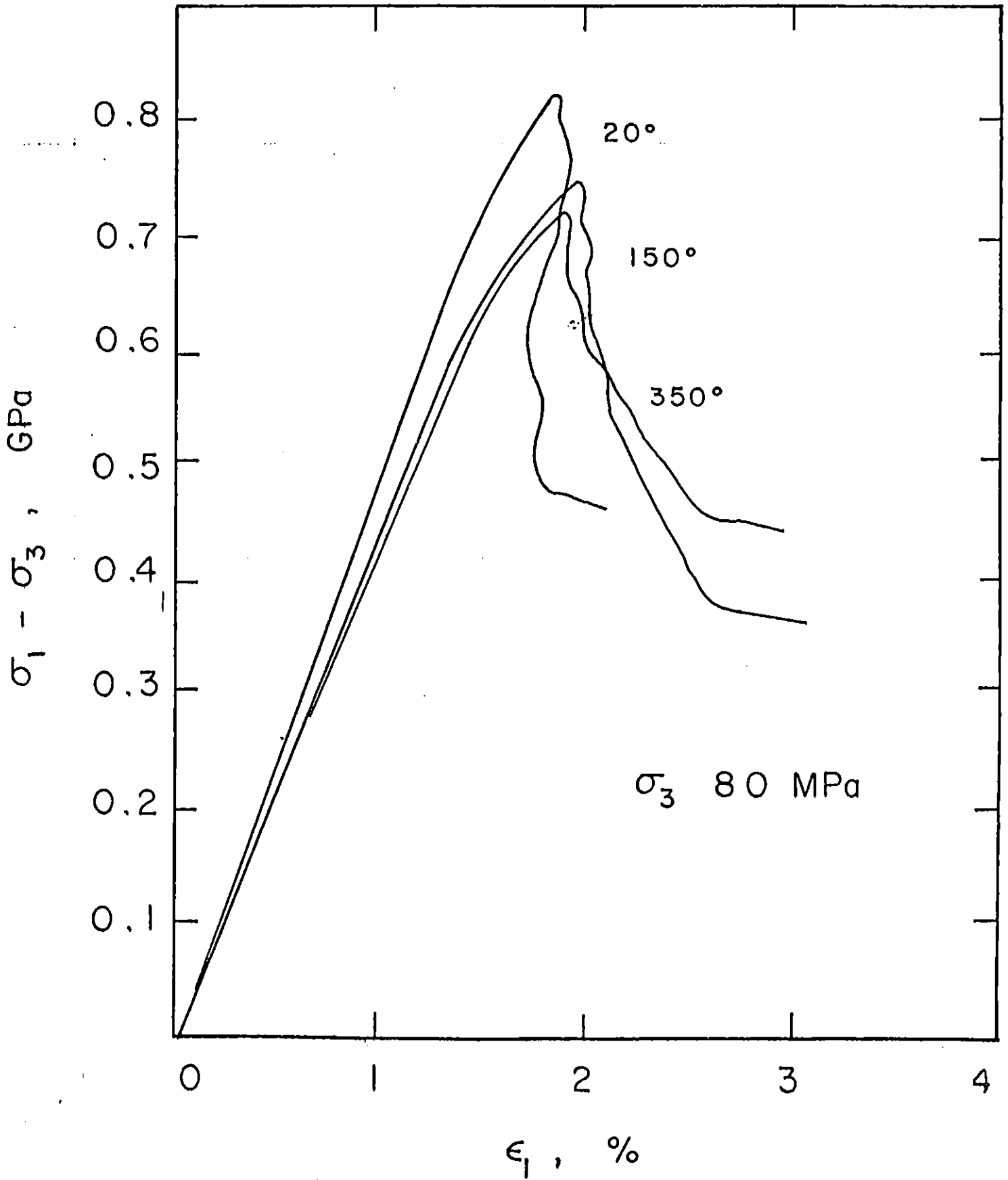


Figure 6



PFW 17 (CREEP)

σ_3 250 MPa

T 350°C

$\epsilon_1, 10^{-3}$
6
4
2

$\dot{\epsilon}$ $3 \times 10^{-6} \text{ s}^{-1}$

UNLOAD AT
 10^{-5} s^{-1} →

T, MINUTES

Figure 7

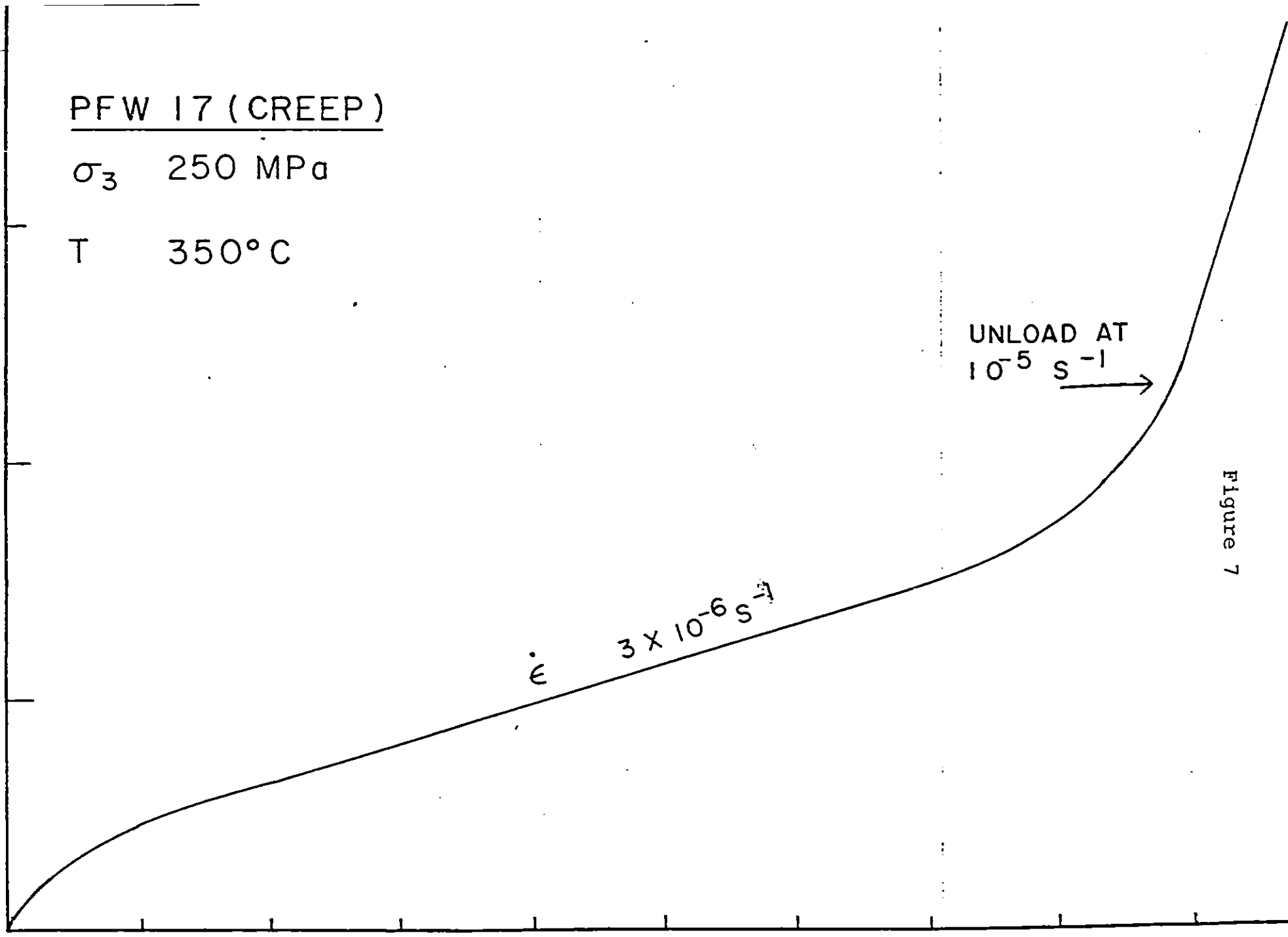


Figure 8

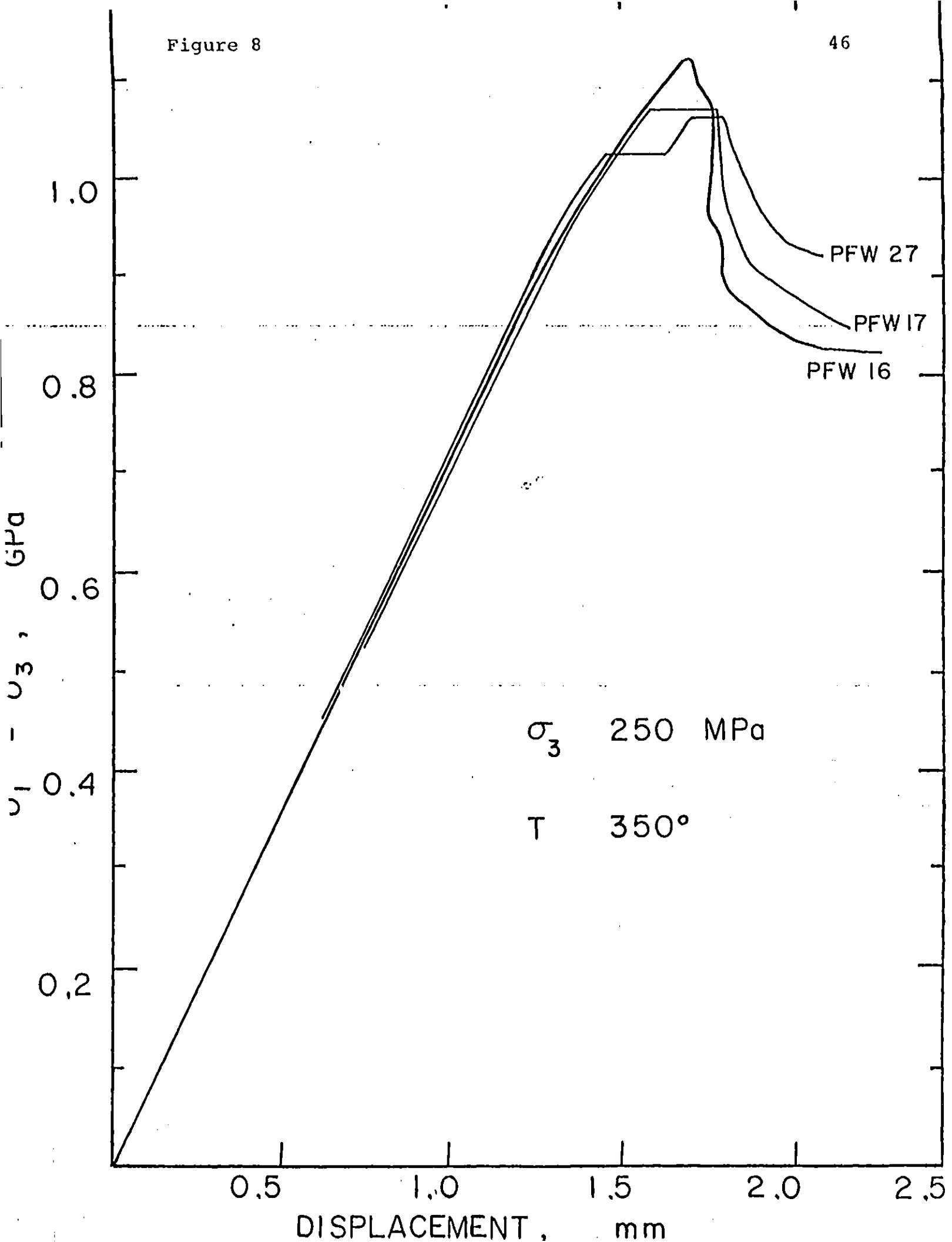
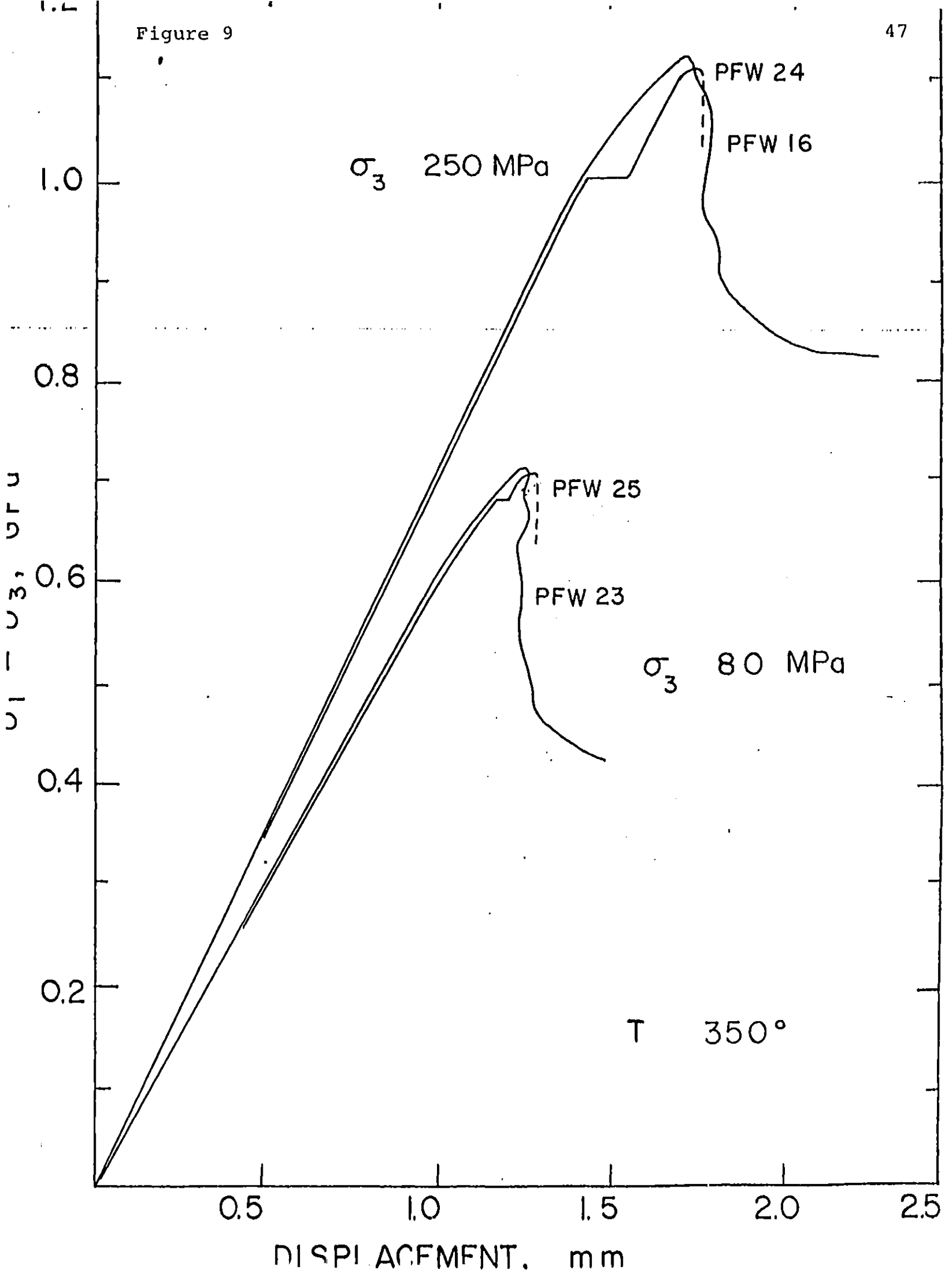
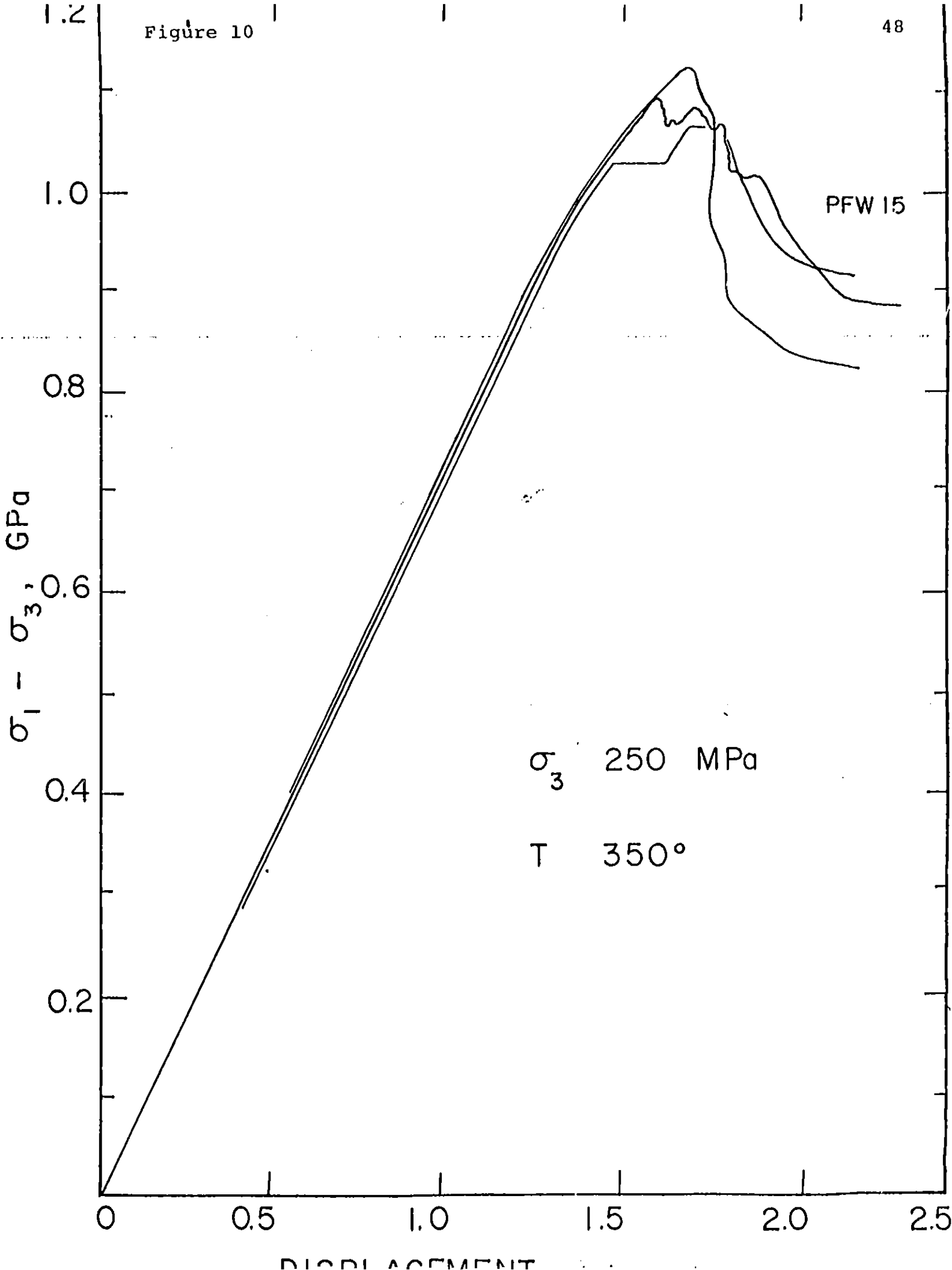


Figure 9





REFERENCES

- Atkinson, B.K., A fracture mechanics study of subcritical tensile cracking of quartz in wet environment, PAGEOGH 117, 1011-1024, 1979.
- Bauer S.J. and B.Johnson, Effects of slow uniform heating on the physical properties of Westerly and Charcoal granites, 20th U.S.Symposium on Rock Mechanics, 1979.
- Brace, W.F., Limits on crustal stress imposed by laboratory experiments, in Proc.U.S.G.S.Conf.IX: Magnitude of deviatoric stresses in the earth's crust and upper mantle 803-821, 1979.
- Brace, W.F. and J.D.Byerlee, California earthquakes - why only shallow focus? Science, 168, 1573-1575, 1970.
- Brace, W.F. and A.H.Jones, Comparison of uniaxial deformation in shock and static loading of three rocks, J.Geophys.Res., 76, 4913-4921, 1971.
- Brace, W.F. and R.J.Martin III, A test of the law of effective stress for crystalline rocks of low porosity, Int.J.Rock Mech.Min.Sci., 5, 415-426, 1968.
- Byerlee, J.D., Frictional characteristics of granite under high confining pressure, J.Geophys.Res., 72, 3639-3648, 1967.
- Carter, N.L. and S.H.Kirby, Transient creep and semi-brittle behavior of crystalline rocks, PAGEOGH, 116, 807-839, 1978.
- Costantino, M.S., Statistical variation in stress-volumetric strain behavior of Westerly granite, Int.J.Rock Mech.Min.Sci., 15, 105-112, 1978.

- Goetze, C., High temperature rheology of Westerly granite, J. Geophys. Res., 76, 1223-1230, 1971.
- Griggs, D. T., Hydrolytic weakening of quartz and other silicates, Geophys. J. Roy. Astro. Soc., 14, 19-31, 1967.
- Griggs, D. T., F. J. Turner, and H. C. Heard, Deformation of rocks at 500° to 800°C, in Rock Deformation Griggs D. and J. Handin ed., G.S.A. Memoir 79, 39-104, 1960.
- Hadley, K., The effect of cyclic stress on dilatancy: another look, J. Geophys. Res., 81, 2471-2474, 1976.
- Haimson, B. C., Effect of cyclic loading on rock, in Dynamic Geotechnical Testing ASTM STP654, 228-245, 1978.
- Handin, J., On the Coulomb-Mohr failure criterion, J. Geophys. Res., 74, 5343-5348, 1969.
- Handin, J. and R. V. Hager, Experimental deformation of sedimentary rocks under confining pressure: tests at high temperature, Bull. Am. Asso. Petro. Geol., 42, 2892-2934, 1958.
- Hojem, J. P. M., N. G. W. Cook and C. Heins, A stiff, two meganewton testing machine for measuring the work-softening behavior of brittle materials, S. Afr. Mech. Eng., 25, 250-270, 1975.
- Hudson, J. A., E. T. Brown and C. Fairhurst, Optimizing the control of rock failure in servo-controlled laboratory tests, Rock Mech., 3, 217-224, 1971.
- Kranz, R. L., The effects of confining pressure and stress difference on static fatigue of granite, J. Geophys. Res., 85, 1854-1866, 1980.
- Kranz, R. L. and C. H. Scholz, Critical dilatant volume of rocks at the onset of tertiary creep, J. Geophys. Res., 82, 4893-4898, 1977.

- Kurita, K., I.C. Getting and H.A. Spetzler, The effect of thermal cycling on volumetric strain, EØS Trans. Am. Geophys. Un., 61, T112, 1980.
- McGarr, A. and D. Pollard, Observations and analysis of structures in exhumed mine-induced faults, in Proc. U.S.G.S. Conf. VIII: Analysis of Active Fault Zones in Bedrock 101-120, 1979.
- Martin, R.J. III, Time dependent crack growth and its application to the creep of rocks, J. Geophys. Res., 77, 1406-1419, 1972.
- Mizutani, H., H. Spetzler, I. Getting, R.J. Martin III, and N. Soga, The effect of outgassing upon the closure of cracks and the strength of lunar analogues, Proc. 8th Lunar Sci. Cong. 1235-1248, 1977.
- Mogi, K., On the pressure dependence of strength of rocks and the Coulomb fracture criterion, Tectonophysics, 21, 273-286, 1974.
- Ohnaka, M., The quantitative effect of hydrostatic confining pressure on the compressive strength of crystalline rocks, J. Phys. Ear., 21, 285-303, 1973.
- Paterson, M.S., Experimental Rock Deformation - The Brittle Field, Springer Verlag N.Y., 1978.
- Paterson, M.S. and J.M. Edmond, Deformation of graphite at high pressures, Carbon, 10, 29-34, 1972.
- Paterson, M.S. and C.W. Weaver, Deformation of polycrystalline MgO under pressure, J. Am. Ceram. Soc., 53, 463-471, 1970.

- Ralieg, C.B. and M.S. Paterson, Experimental deformation of serpentinite and its tectonic implications, J. Geophys. Res., 70, 3965-3985, 1965.
- Rice, J.R., Theory of precursory processes in the inception of earthquake rupture, Gerlands Beitr. Geophysik, 88, 91-127, 1979a.
- Rice, J.R., The mechanics of earthquake rupture, in Proc. of Int. School of Physics "Enrico Fermi" Course LXXVIII on Physics of the Earth's Interior, 1979b.
- Rudnicki, J.W. and J.R. Rice, Conditions for the localization of deformation in pressure sensitive dilatant materials, J. Mech. Phys. Solids, 23, 371-394, 1975.
- Rummel, F., H.J. Alheid and C. Frohn, Dilatancy and fracture-induced velocity changes in rock and their relation to frictional sliding, PAGEOGH, 116, 743-764, 1978.
- Sano, O., Fundamental Study on the Mechanics of Brittle Fracture of Rocks, D. Eng. thesis, Kyoto Univ., 1978.
- Scholz, C.H. and T.A. Koczyński, Dilatancy anisotropy and the response of rock to large cyclic loads, J. Geophys. Res., 84, 5525-5534, 1979.
- Simmons, G. and H.W. Cooper, Thermal cycling cracks in three igneous rocks, Int. J. Rock Mech. Min. Sci., 15, 145-148, 1978.
- Sprunt E.S. and W.F. Brace, Some permanent structural changes in rocks due to pressure and temperature, Advances in Rock Mechanics, Proc. 3rd. Congr. Int. Soc. Rock Mech. Denver, IIA 524-529, 1974.

- Stesky, R.M., The Mechanical Behavior of Faulted Rock at High Temperature and Pressure, Ph.D.thesis, M.I.T., 1975.
- Stesky, R.M., Mechanism of high temperature frictional sliding in Westerly granite, Can.J.Ear.Sci., 15, 361-375, 1978.
- Stesky, R.M., W.F. Brace, D.K. Riley and P-Y.F. Robin, Friction in faulted rock at high temperature and pressure, Tectonophysics, 23, 177-203, 1974.
- Stuart, W.D., Quasi-static earthquake mechanics, Rev. Geophys. Space Phys., 17, 1115-1120, 1979.
- Tullis, J. and R.A. Yund, The brittle-ductile transition for dry Westerly granite as a function of temperature and pressure, in Proc. U.S.G.S. Conf. II: Experimental Studies of Rock Friction with Applications to Earthquake Prediction, 511-542, 1977a.
- Tullis, J. and R.A. Yund, Experimental deformation of dry dry Westerly granite, J. Geophys. Res., 82, 5705-5718, 1977b.
- van der Molen, I., Some Physical Properties of Granite at High Pressure and Temperature, Ph.D.thesis, Aust. Nat. Univ., 1979.
- Walsh, J.B., The effect of cracks on the uniaxial elastic compression of rocks, J. Geophys. Res., 70, 399-411, 1965.
- Wawersik, W.R., Time dependent rock behavior in uniaxial compression, in New Horizons in Rock Mechanics, Hardy, H.R. and R. Stefanko ed., Proc. 14th U.S. Sym. Rock Mech., 85-106, 1973.

- Wawersik, W.R. and W.F. Brace, Post-failure behavior of a granite and a diabase, Rock Mech., 3, 61-85, 1971.
- Wawersik, W.R. and W.S. Brown, Creep Fracture of Rock, Report #UTEC-ME-73-197, Univ. Utah, 1973.
- Wawersik, W.R. and C. Fairhurst, A study of brittle rock fracture in laboratory compression experiments, Int. J. Rock Mech. Min. Sci., 7, 561-575, 1970.
- Wiederhorn, S.M., Mechanisms of subcritical crack growth in glass, in Fracture Mechanics of Ceramics Vol. IV R.C. Bradt ed. Plenum, N.Y., 549-580, 1978.
- Wong, T.F. and W.F. Brace, Thermal expansion of rocks: some measurements at high pressure, Tectonophysics, 57, 95-117, 1979.
- Zoback, M.D. and J.D. Byerlee, The effect of cyclic differential stress on dilatancy in Westerly granite under uniaxial and triaxial conditions, J. Geophys. Res., 80, 1526-1530, 1975.
- Zoback, M.L. and M.D. Zoback, Faulting patterns in North-Central Nevada and strength of the crust, J. Geophys. Res., 85, 275-284, 1980.

CHAPTER 2

MICROMECHANICS OF FAULTING IN WESTERLY GRANITE

INTRODUCTION

Since Brace et al [1] first suggested the use of ion-thinning in the preparation of samples for scanning electron microscope (SEM) observation, numerous attempts have been made in the past decade using this technique to gain further insight into the micromechanics of rock deformation. Detailed studies of the crack and pore morphology of virgin rocks were performed by Sprunt & Brace [2], Montgomery & Brace [3], and Richter & Simmons [4]. Quantitative correlation of SEM data with mechanical and transport properties were considered by Hadley [5] and Brace [6]. Sprunt & Brace [7] looked at the effects of temperature and pressure cycling. The development of stress-induced cracks was studied by Tapponier & Brace [8] on samples deformed in constant displacement rate, whereas Kranz [9,10] made observations on samples deformed in creep, and recently Batzle et al [11] presented results of *in situ* SEM observation in uniaxial compression.

In recent reviews, both Brace [12] and Paterson [13] emphasized that, the studies above notwithstanding, little is known concerning the microscopic mechanisms of faulting, and further work is necessary to clarify this fundamental process. Tapponier & Brace [8] made preliminary observation on post-failure samples from earlier experiments of Wawersik & Brace [14], but since the latter samples were deformed at different pressures, no detailed comparison was possible and

they could only make several general conclusions on features common to all the samples. The most deformed samples obtained by Kranz [10] were at the onset of tertiary creep, and no post-creep failure samples were available for SEM study.

In this study, we attempted to investigate this general problem in some detail with several specific questions in mind. Contradictory observations on the significance of axial versus shear cracking were presented by Hallbauer et al [15] and Friedman et al [16] respectively based on optical microscopy work. Can we resolve this question by making systematic SEM study on a suite of samples deformed stably through the post-failure region and hence get a better picture of the micromechanics of faulting? Recent holography [17] and acoustic emission [18] work seem to indicate that strain localization occurs just before failure, whereas some of the theoretical studies [19] concluded that in general, post-failure localization should be expected in axi-symmetric loading, the latter conclusion being based on bifurcation analysis within a continuum framework. How can this apparent discrepancy be resolved? How should local observations of microstructures be correlated with such a global criterion, and to what extent is a continuum description meaningful for post-failure deformation? Previous SEM work on stress-induced cracks was exclusively on samples deformed at room temperature. What are the combined influence of temperature and pressure on

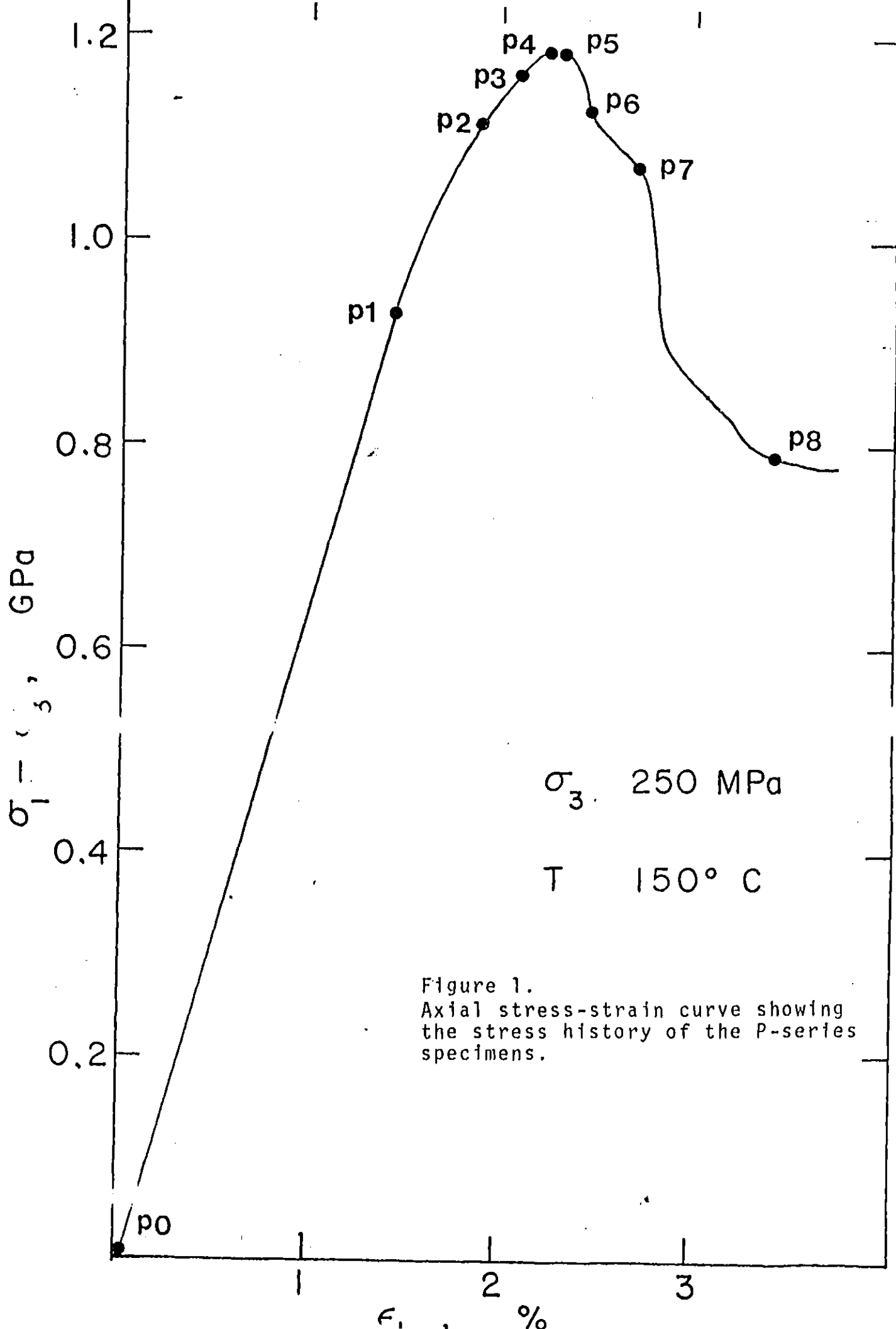
the development of stress-induced microstructures?

We performed SEM observation on two suites of Westerly granite samples deformed at temperature and pressure; some of the specimens of Tapponier & Brace [8] deformed at room temperature were also re-examined. Westerly granite was chosen because its post-failure behavior was investigated in some detail at room temperature [14] and recently at elevated temperatures [20], and the microstructures were also quite well-documented in a number of previous SEM studies [2,3,5,6,7,8].

EXPERIMENTAL PROCEDURE

In spite of the relative success of *in situ* SEM observation under uniaxial tension [21] and compression [11], the adaptation of similar techniques at temperature and pressure is still not feasible. The procedure we followed was therefore that used by Tapponier & Brace [8] and Kranz [8] at room temperature.

The samples, all pre-dried *in vacuo* were prepared as described in [20]. Experiments were performed in an internally heated gas apparatus at a strain rate of 10^{-5} s^{-1} . The temperature and pressure conditions were chosen roughly equivalent to those expected at depths of 8 and 15 km: one suite of samples (P-series) was deformed at 250 MPa and 150°C, and the other (H-series) at 400 MPa and 350°C. Specimens were cored from two blocks of Westerly granite, with each suite from an identical block.



Dimensions of the samples and the values of the differential stress to which they were subjected are tabulated in Table I. Five samples in the P-series were obtained at the post-failure stage by carefully performing manual unloading-loading control, the details of which were given in [14] and [20]. Owing to experimental error and sample variability, the failure stresses are expected to fluctuate by ± 70 MPa. The complete stress-strain curve shown in Figure 1 is that of P8. The other samples (P4-7) might actually have curves with qualitative features different from that of P8 if they had not been retrieved and were deformed stably through the complete post-failure region. We pointed out in [20] that the irregular alternations between steeply dropping and flatter parts of the curves are highly variable among different experiments. Coordinates of P4-7 as shown in Figure 1 are determined on the basis of the relative difference between their final stress values and the peak stresses they actually reached. The relative positions of the two pre-failure samples P2 and P3 are determined by comparing the slope of the curves. Although the stress values shown are different from the absolute values, we believe that Figure 1 is a true representation of the development of different stages of deformation.

We have three samples (P4, P5, H3) which were deformed to stresses close to failure (Figure 1,2). Our fracture

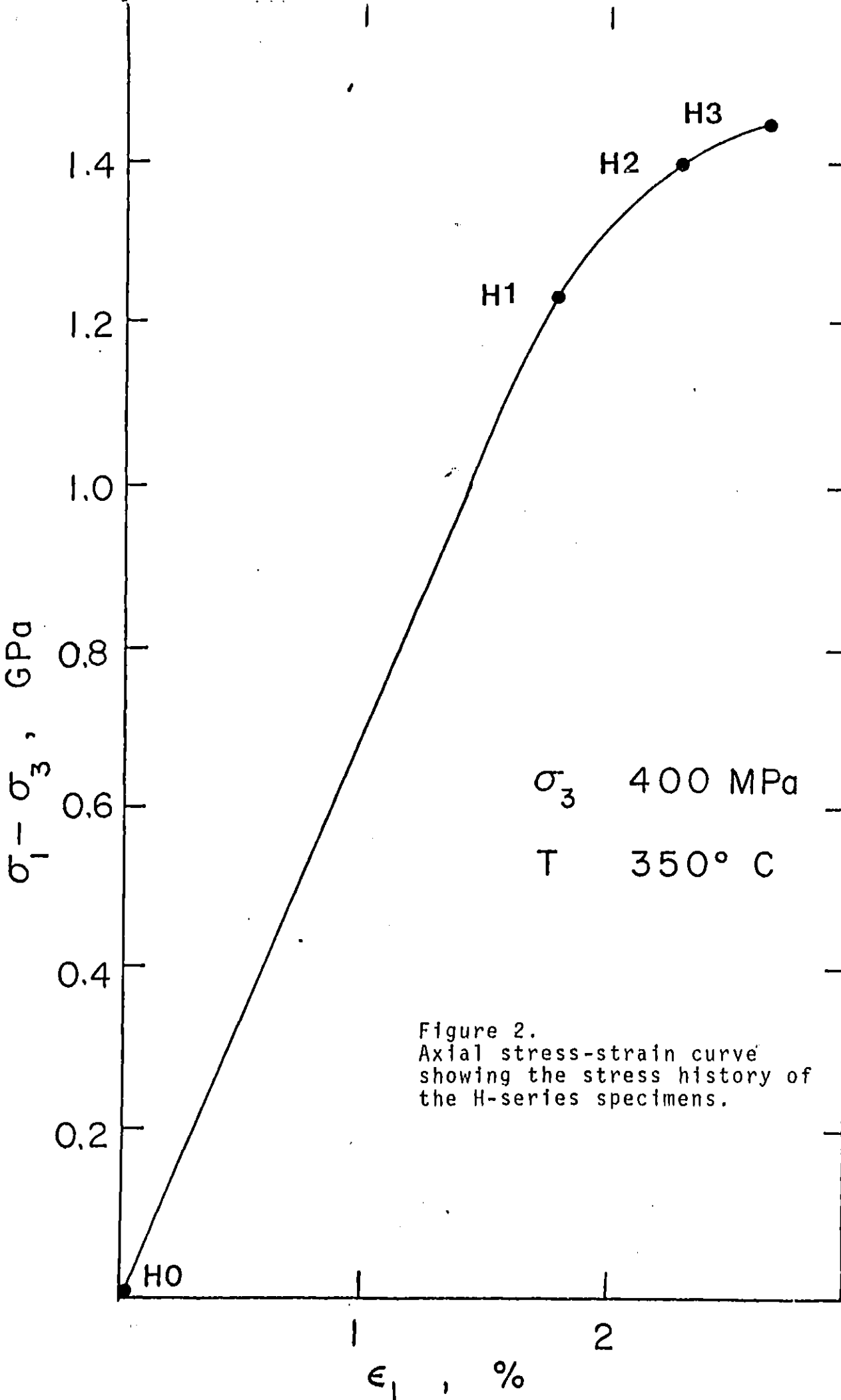


Figure 2.
Axial stress-strain curve
showing the stress history of
the H-series specimens.

experiments [20] show that failure at 250MPa/150°C and 400 MPa/350°C are explosive unless manual unloading-loading cycles are used to control the post-failure deformation. No manual control was used in the H-series, and hence we are sure that H3 was in the pre-failure stage and at a stress slightly lower than the peak value. Two unloading-loading cycles were used for P4: manual control was attempted at a stress which turned out to be slightly lower than the fracture strength, and hence the first cycle was solely to push the stress closer to the failure stress. The subsequent cycle was to check that post-failure stage had indeed been reached. Only one cycle was necessary for P5, which showed a strength drop of about 10 MPa at the first cycle, slightly more than that at the second cycle of P4.

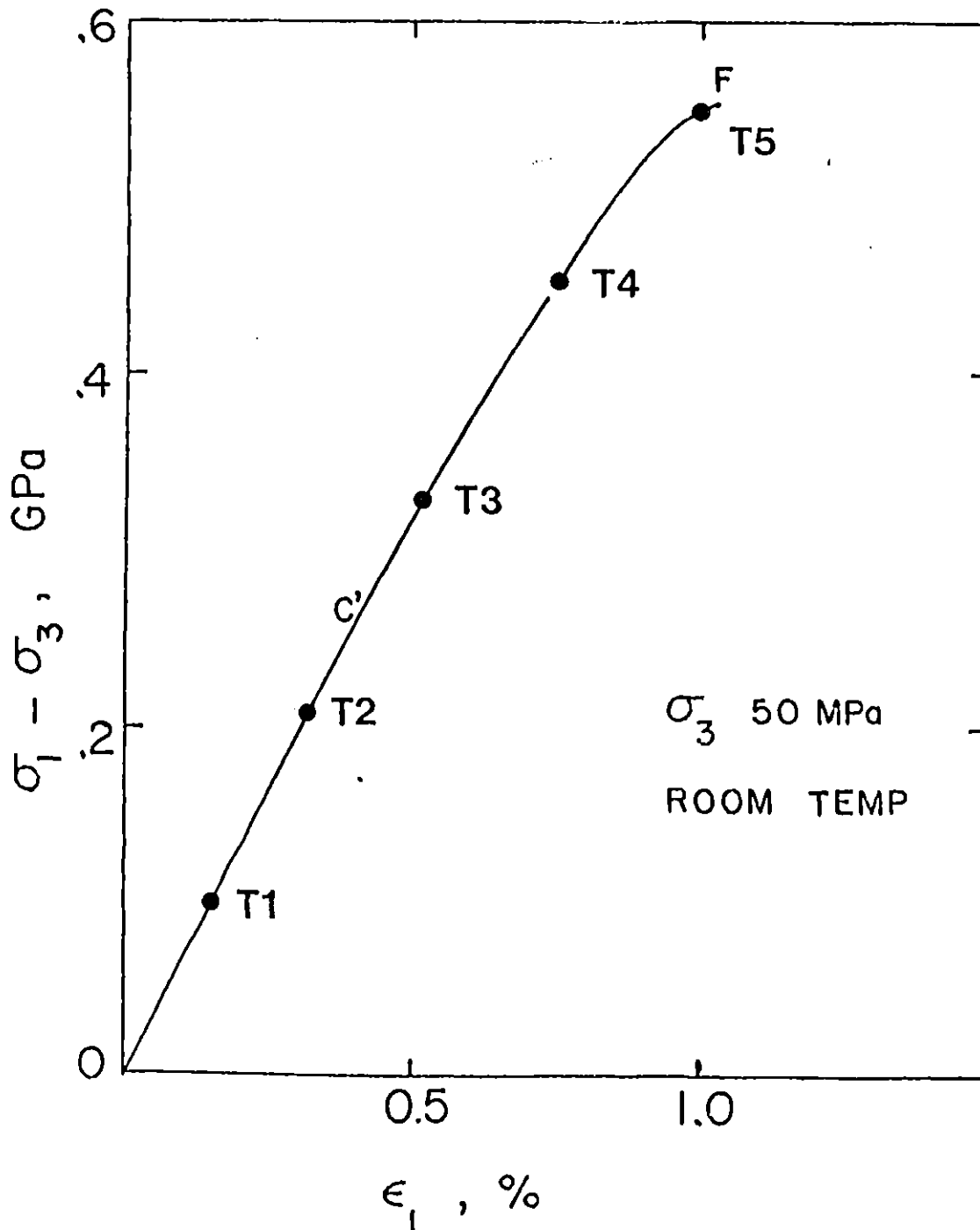
Specimens were obtained in the following way: confining pressure was first applied, and then the temperature was raised. Next the differential stress was applied by advancing the piston or by cyclic unloading-loading in post-failure deformation, and the differential stress was released as soon as the highest stage of deformation desired had been reached. The set-up was then cooled back to room temperature, and finally the confining pressure reduced to atmosphere. The heating and cooling time were both about 30 to 60 minutes; thus the heating and cooling rates were less than 10°C/min. On dismantling the jacketing arrangement, the diameter of the sample was checked for heterogeneity

in deformation. In P4-8, the deformed samples show azimuthal variations in permanent strain, and two conjugate directions almost perpendicular to each other can be located with maximum and minimum transverse elongation. Care was taken to perform sectioning on an axial plane containing the maximum diameter, which also coincides with a plane roughly perpendicular to the incipient fault plane in post-failure samples.

Some of the pre-failure samples (H0,H1,H2,P2,P3) were cored and polished following the methods used in [2] and [8]. The rest of the samples were prepared following a modified scheme outlined in [4]. The latter procedure is different in that a "crack section" of larger diameter (25.4 mm) is made; because the section is sufficiently thick (about 100 μm , three times the thickness of standard thin sections), cracking induced by preparation is expected to be insignificant. The crack section is more convenient for observation of inhomogeneously deformed specimens because it samples about 2/3 of the total area, and preliminary petrographic observation (in transmission and reflection) can be made before the more detailed SEM study.

All the SEM specimens were ion-milled [1] and sputter-coated with about .02 μm of gold-palladium. Observations were made on a JEOL JSM-35 microscope equipped with an X-ray energy dispersive analyser. Accelerating voltage was 20 kV, and the resolution was expected to be about .02 μm .

Figure 3.
Schematic stress-strain curve showing the stress history of the T-series specimens from [8].
C' and F respectively denote the point at the onset of dilatancy and the point of failure.



For quantitative analysis of the microstructures, photo-mosaics extending over 20-40 grains were prepared with the SEM at 150 or 300 magnification. We attempted to estimate the specific crack surface area on three samples: T5 (Figure 3), P3 and H2 by counting the number of crack intersections with test arrays placed at 15° intervals. An array consists of about 50 parallel traverses spaced at 67 μm apart and all placed at a fixed angle with respect to the maximum compression (σ_1) direction.

OBSERVATION

Unstressed samples

The two samples P0 and H0 were each heated in the pressure vessel with temperature and pressure maintained constant for a duration of about one hour. The pressures we used were both higher than the crack closing pressure for Westerly granite as estimated from compressibility data [22]. Judging from theoretical analysis and measurements of thermal expansion under pressure [23,24], one would not expect significant thermal cracking. Sprunt & Brace [7] studied the permanent microstructural changes induced by pressure and temperature cycles under the SEM. What we observed was qualitatively similar to this earlier work.

The bridges found to span some of the larger pre-existing cracks [1] in virgin granites were not as evident

in P0 or H0; probably most of the bridges were crushed as a consequence of the pressure cycle. Isolated μ m-sized cracks could be seen emanating from old cavities. When observed under high magnification, the pre-existing cracks, especially those along grain boundaries, seem to be slightly wider than the counterparts in virgin samples. No significant transgranular cracking was observed.

No attempt was made to quantitatively determine the more subtle effects of pressure and temperature, because too large an area has to be scanned under high magnification for the measurement to be statistically meaningful. In any event, the structural damages of the pressure and temperature cycle would be insignificant relative to those induced by the differential stress discussed below.

The pre-failure samples

In previous SEM work at room temperature [8,9,10], a heavy emphasis was placed on clarifying the relationship between stress-induced cracking and dilatancy. Tapponier & Brace [8] concluded that new cracks first began to appear within 50 MPa of C', the stress at the onset of dilatancy. Although preliminary data of Hadley [25] indicate dilatancy in a gabbro persists to 200 MPa, 400°C it is difficult to measure accurately the volumetric strain at elevated temperature and pressure. We do not have accurate data on C' for Westerly granite at our temperature

and pressure conditions, and the approach we took was therefore to compare our samples with the T-series specimens studied in [8] (Figure 3).

The features observed in our samples P1 and H1 are qualitatively similar to those of T4. The grain boundaries, healed transgranular cracks, and pre-existing cleavage cracks, all of which were categorized as "type A cracks" previously [8], started to widen. Isolated sharp-tipped transgranular cracks can also be observed within the grains.

The samples at the next stage of deformation (P2, P3, H2) have a substantial number of cracks at low angles ($<15^\circ$) to σ_1 with features very similar to those observed in T5. The latter specimen is believed to be very close to failure [8] whereas our samples were all at least about 50 MPa below the peak stress. An increase of transgranular cracks in our three samples over P1 and H1 is very evident. As in T5, the transgranular cracks have sharp tips and typically originate from grain interfaces, pre-existing grain boundary cracks and pores. Most of the minor minerals, especially the biotite, have low-angle cracks associated with them in neighboring grains.

In contrast to T5, our three samples deformed under higher temperatures and pressures have quite a significant number of high-angle ($>15^\circ$) transgranular cracks located in the feldspars. Examples of such features in microcline

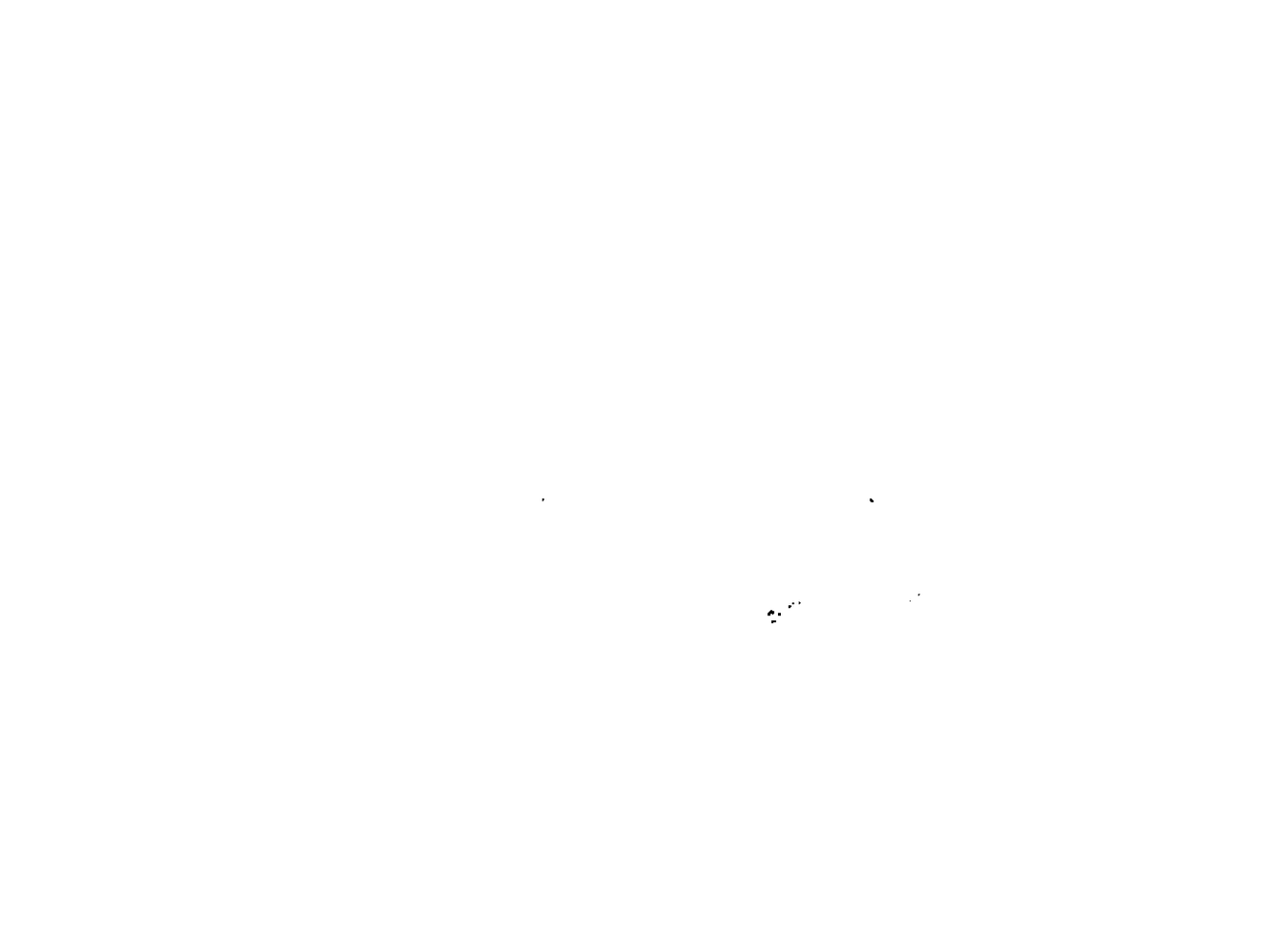
The image area is mostly blank, suggesting the micrograph content is either missing or extremely faint. Only a few small, dark specks are visible in the center-right area.

Figure 4

High-angle cleavage cracks observed in H2. The host mineral is microcline. Note the parallelism of most of the cracks and the step-like propagation paths. Maximum compression was vertical, and the scale bar at the top is 25 μm long.



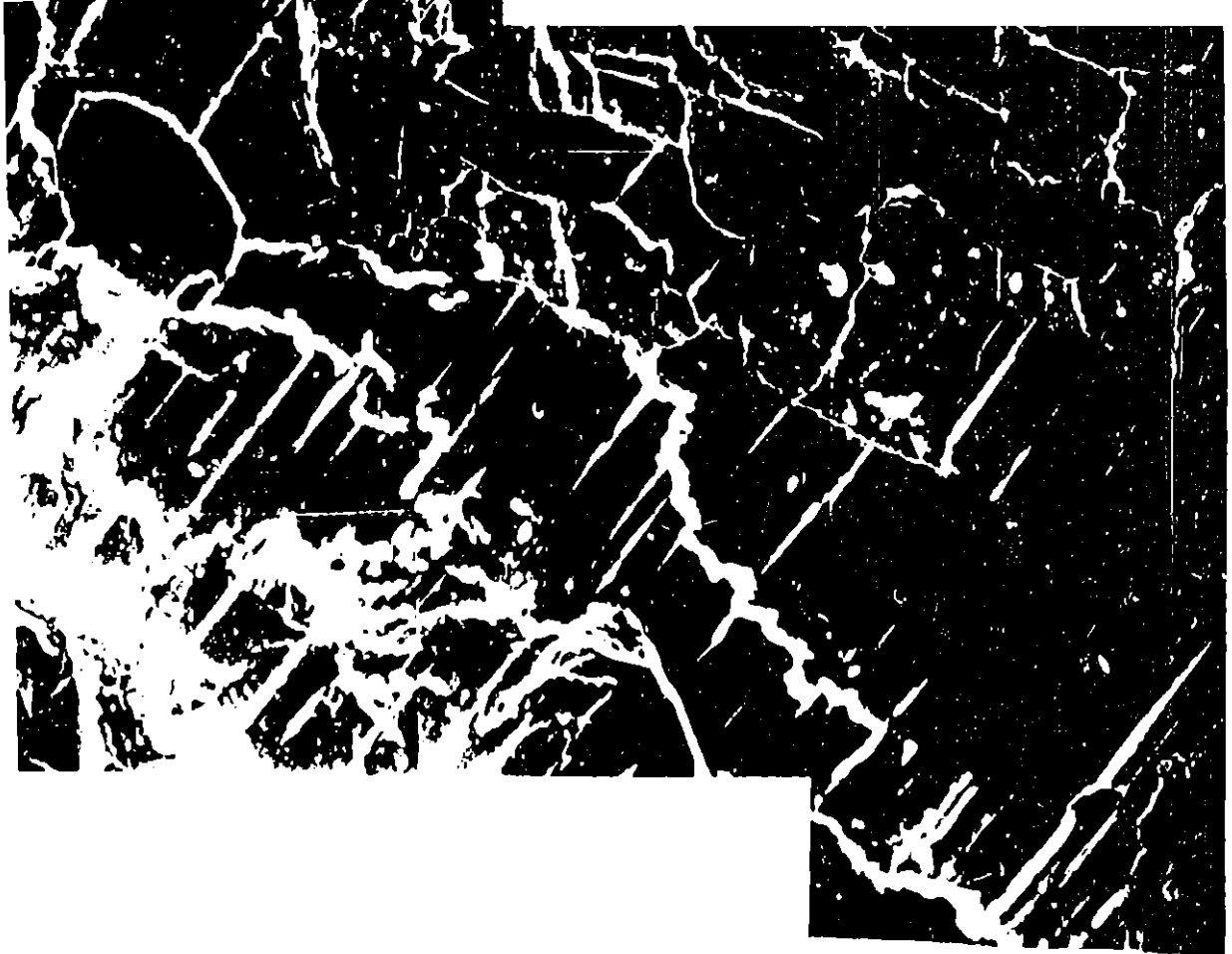
are shown in Figures 4 and 5. The wide range of angles is rather surprising; cracks up to angles of about 60° were observed. The appearance of a parallel array with step-like propagation paths strongly suggests that they are cleavage cracks. We can not find similiar cracks in quartz, which does not have a preferred cleavage [26]. Grain boundaries in P3 and H2 are continuously cracked, similiar to what was observed in T5 [8]. Among the three samples, grain boundaries in H2 have widened the most, to be followed by those in P3 and then T5.

Photo-mosaics at magnifications of 300X and 150X respectively were prepared for H2 and P3. These mosaics together with another one for T5 at 300X prepared by Tapponier & Brace [8] were analyzed following standard stereological procedures [27]: we counted the number of intersections of cracks with test arrays placed at 15° intervals starting from $\theta=0^\circ$. (θ is defined to be the angle between the test array and σ_1 .) The spacing between adjacent traverses in an array was $67\mu\text{m}$.

Since we are mainly interested in the stress-induced cracks, we did not count the pores. The number of intersection points per unit length, denoted by $P_L(\theta)$, at 0° and 90° were previously determined for T5[8], but since this earlier study used a smaller transverse spacing ($25\mu\text{m}$) and included the pores in the count, we expect our corresponding results to be different. It was suggested in [8]

Figure 5

Complicated pattern of cracking observed in a microcline grain in P3. At lower half of the micrograph is a set of cleavage cracks at about 45° to σ_1 ; near the quartz grain (qtz) at the top is a second set of axial cracks. A few of the shorter cracks almost perpendicular to σ_1 were probably formed during unloading. Maximum compression was vertical, and the scale bar at the top is 50 μm long.



that 300X was probably the minimum magnification for sufficient resolution, but since P3 is more deformed than all the T-series samples, we believe that at 150X most of the stress-induced cracks are counted except for some smaller cracks emanating from pores.

We show in [27] on the basis of stereological analysis that our measurements match quite well with the theoretical prediction for a structure with one single preferred orientation (parallel to σ_1). For such an oriented structure, the orientation dependence is determined by two terms: one represents a system of randomly oriented cracks, and the other a set of cracks parallel to the preferred orientation. Expressed in terms of the values of P_L at $\theta=0^\circ$ (P_L^{\parallel}) and at $\theta=90^\circ$ (P_L^{\perp}), the relation for $P_L(\theta)$ is:

$$P_L(\theta) = P_L^{\parallel} + (P_L^{\perp} - P_L^{\parallel}) \sin\theta$$

We least-squared fitted our data to the above equation, and evaluated P_L^{\parallel} and P_L^{\perp} from the regression results. The relevant data are tabulated in Table II.

Two useful parameters can be defined to characterize the average crack density and orientation dependence as seen on the mosaics [27]. The crack length per unit area (L_A) for an oriented structure is given by

$$L_A = P_L^{\perp} + (\pi/2 - 1) P_L^{\parallel}$$

Figure 6

An axial crack array in P5. Two quartz grains are shown, separated by a grain boundary (g). The lighter mineral at the bottom is magnetite. Maximum compression was vertical, and the scale bar at the top is 50 μm long.



and the degree of anisotropy (Ω_{12}) is given by

$$\Omega_{12} = (P_L^\perp - P_L^\parallel) / (P_L^\perp + (\pi/2 - 1)P_L^\parallel);$$

The theoretical values of L_A and Ω_{12} are also shown in Table II. As expected a sample subjected to a high differential stress shows a higher value of L_A . A high Ω_{12} value indicates that orientations close to σ_1 (the low angles) are preferred. Typically, a sample deformed at a higher pressure and temperature shows a lower value of Ω_{12} in agreement with the previous observation of larger number of high-angle cracks in such a sample.

The samples close to failure

The three samples closest to failure (P4, P5, H3) have many common features. Nearly all the quartz grains show some degree of transgranular cracking. Many can be found with arrays of transgranular cracks at low angles, some of which have extended over the whole grain (Figures 6 and 8). A number of crack arrays are found in H3 also, showing that axial cracking can still be significant at pressures up to 400 MPa and temperatures to 350°C.

The cracks in the quartz grains in our samples are more numerous and closely spaced when compared with Figure 7 of Tapponier & Brace [8] which show one of the most intensely cracked area in quartz in the T-series samples. In our three samples, there are also isolated high-angle cracks in quartz which have propagated over

Figure 7

Shear cracks in a plagioclase grain in P5. The cracks form two conjugate sets at about 45° to σ_1 . The large crack at the center forms part of a localized zone. Maximum compression was vertical and the black scale bar at the top is 50 μm long.

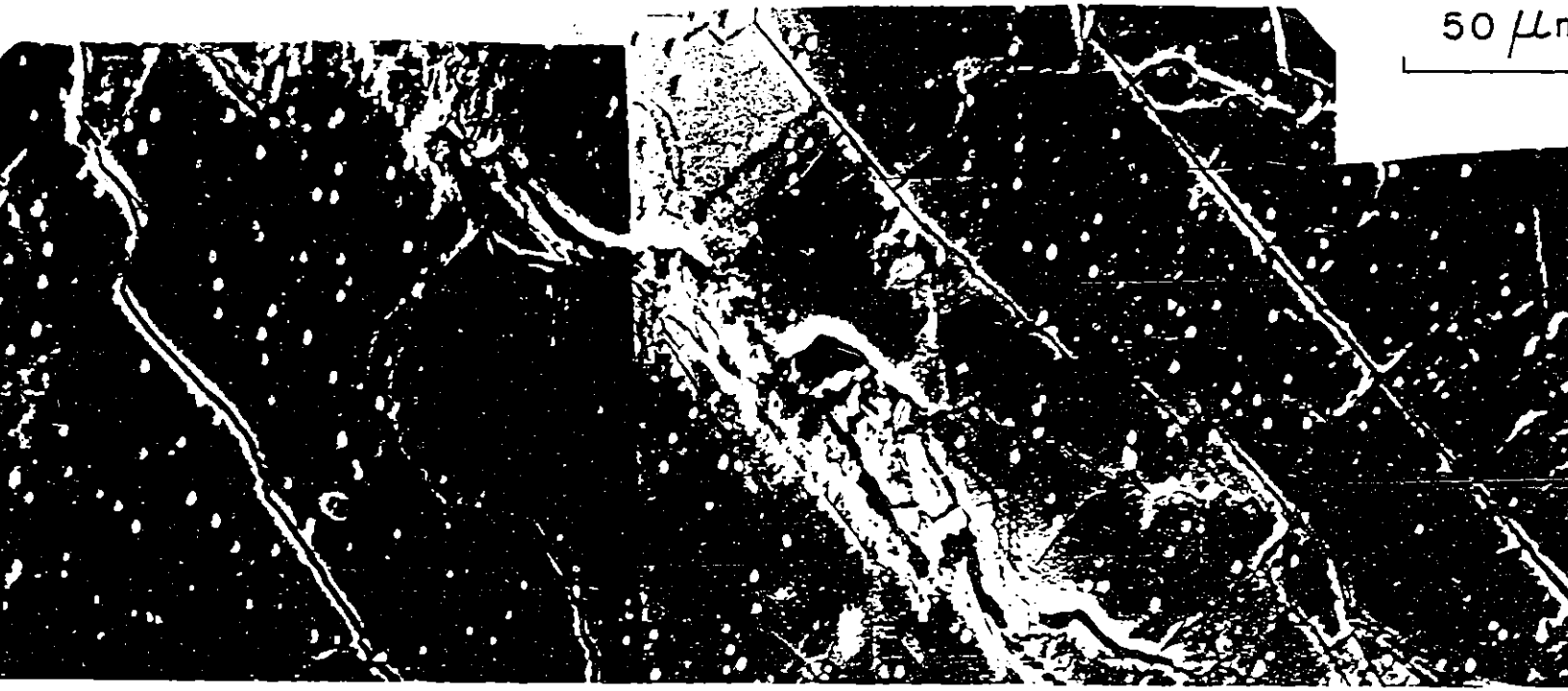


Figure 8

Axial crack arrays in microcline (mi) and quartz (qtz) observed in P5. Mineral at the top is plagioclase (pg). The high-angle crack in the quartz grain is a pre-existing crack that has extended. Maximum compression was vertical, and the scale bar at the top is 50 μm long.



the entire grain (Figure 8), most of which apparently result from extension of pre-existing cracks.

The deformation in the feldspars seem to be dependent on grain orientation. The high-angle cracks discussed above tend to be much longer than those in P3 and H2, with some traversing the whole grain; most probably they have extended along the preferred cleavage planes (Figure 7). In microcline, a significant number of grains have arrays of axial cracks (Figure 8) similar to those in quartz. Most of these arrays are along cleavages and are even more closely spaced than their counterparts in quartz. Similar features are not observed in plagioclase; instead the pores which are relatively abundant in this mineral [3] tend to lengthen and networks of thin cracks can be seen joining them together (Figure 9).

The biotite grains in H-series samples seem to be more highly deformed than their counterparts in the P-series. Isolated cases of folding started to be observed in H2, and one case of kinking was found in H3. The situation is different for the P-series: no kinking was detected up to P5, and folding started in P4. In H3, P4 and P5 high-angle cleavage cracks extending over the entire grain were also observed (Figure 10).

Because of the complexity of the crack arrays and networks and the variety of cracking observed in these

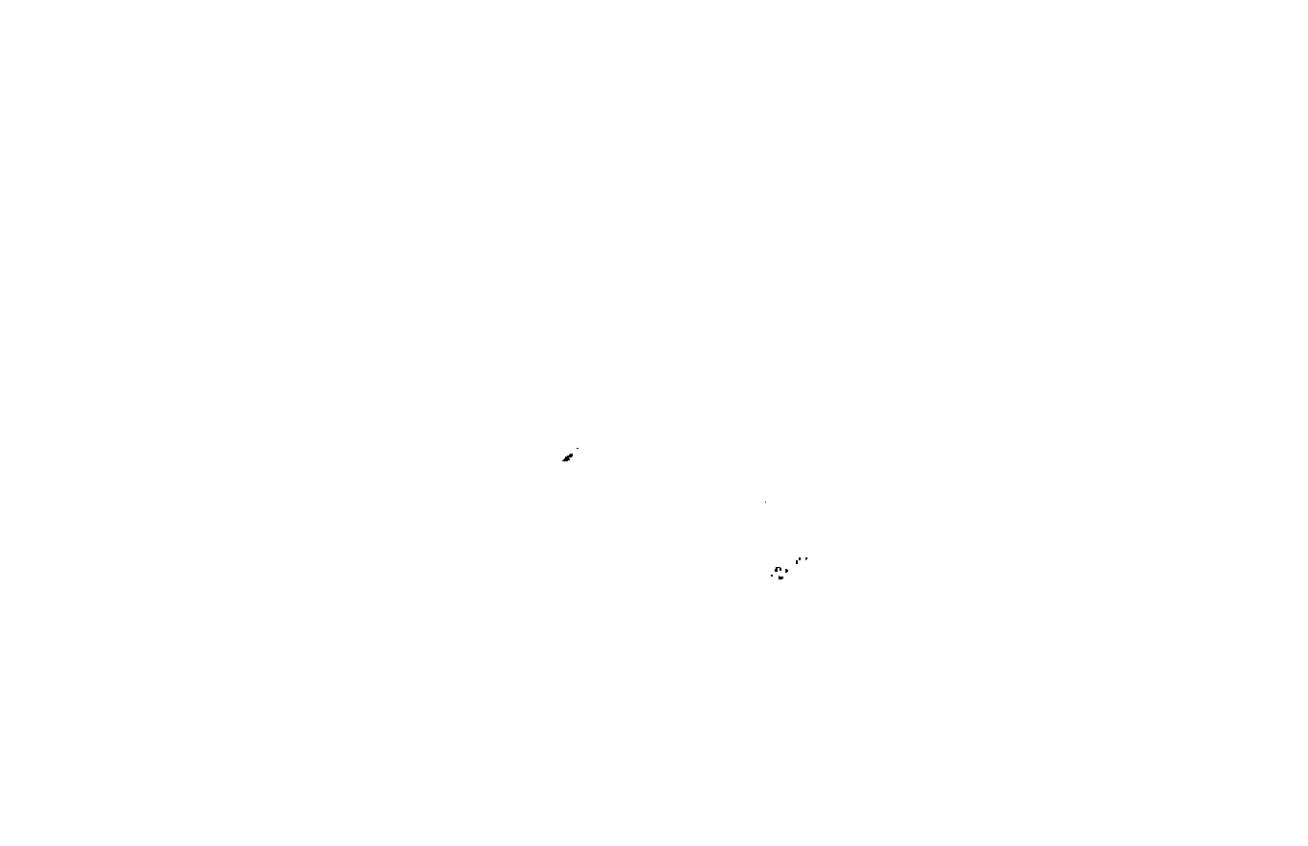
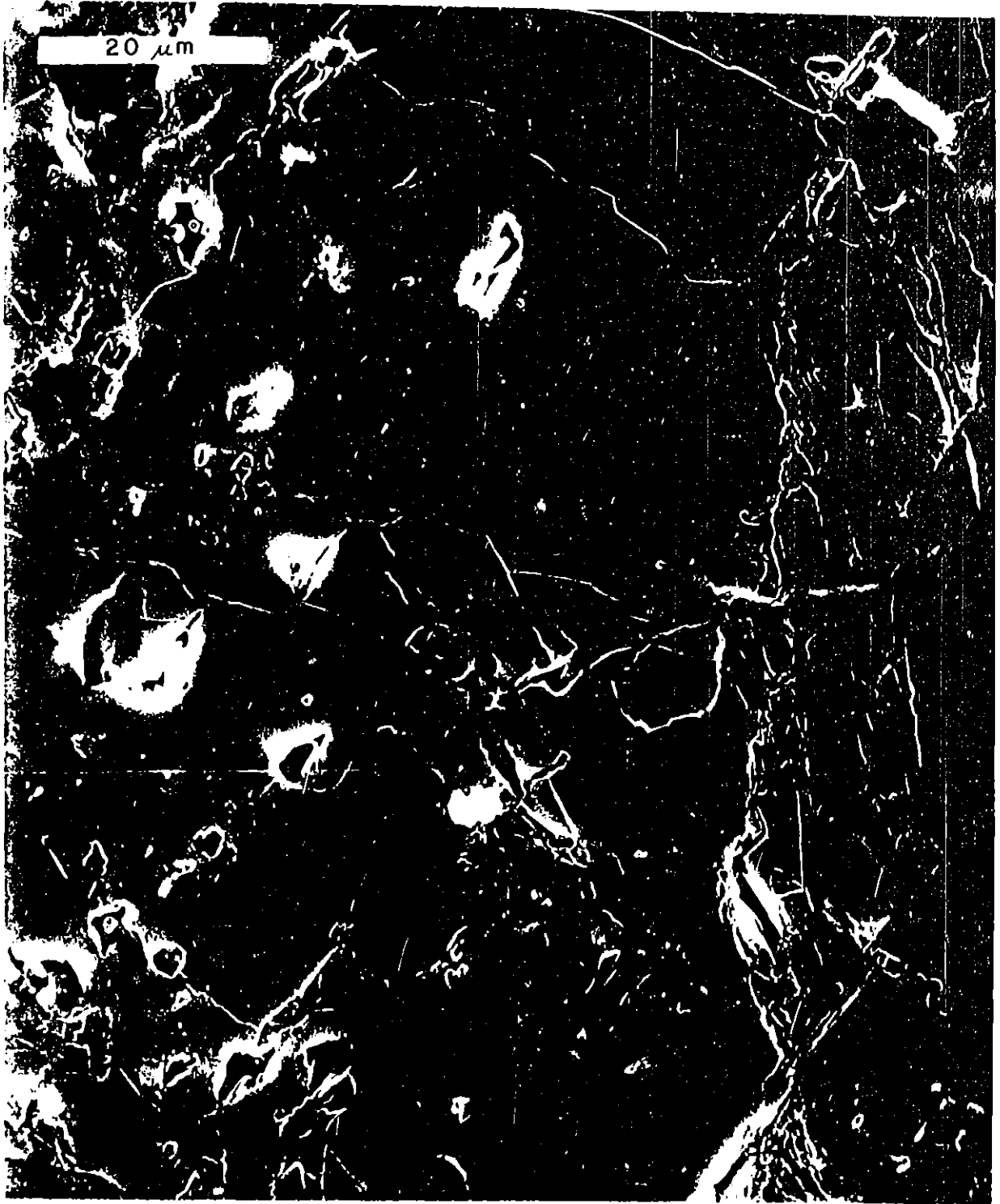
The image is a micrograph showing a plagioclase grain. It features a network of cracks that appear to have originated from pores. The cracks are most densely packed on the right side of the grain. A scale bar is located at the top of the image, indicating a length of 20 micrometers. The grain is labeled 'H3'.

Figure 9

Pore-emanated cracks in a plagioclase grain in H3. Note the dense crack network on the right. Maximum compression was vertical, and the scale bar at the top is 20 μm long.



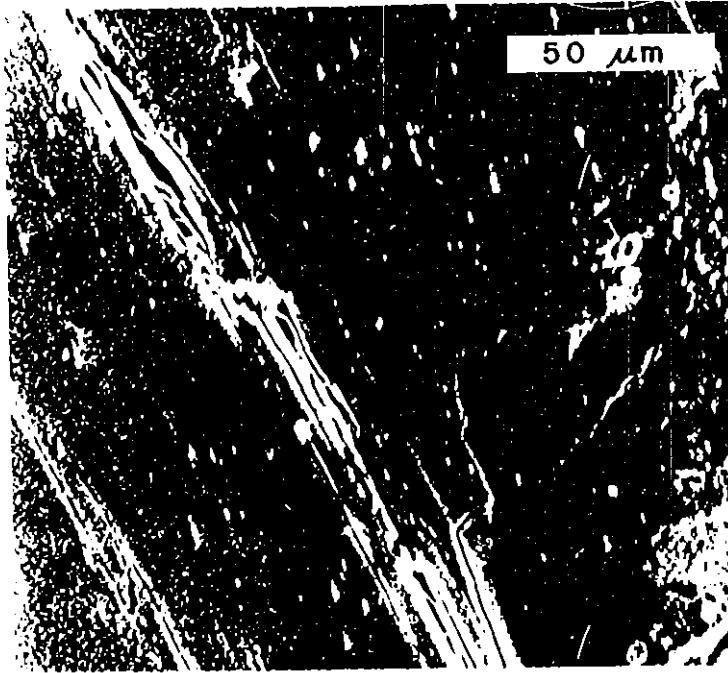
samples, it is difficult to quantitatively estimate the relative intensity of each type of cracking. We can only offer an overall qualitative impression. More and longer high-angle cracks were seen in H3. Many closely spaced axial crack arrays similar to Figure 8 were observed in microcline in P4, especially in grains neighboring the biotite. Intensive cracking in quartz such as in Figure 6 was not very common in P4, but a lot of axial cracks started to be observed in P5. In comparison, H3 seems to have fewer axial crack arrays. Many of the heavily cracked areas in plagioclase were crushed during the polishing process, and the delicate features joining up the pores in many areas can not be resolved under the SEM even after ion-thinning. It is therefore difficult to generalize on the relative extent of the type of crack network (such as Figure 9) among the samples.

In addition to the grain boundary cracks, almost all of which have widened and formed a network continuous over the entire sample, intergranular cracking over two adjacent grains were commonly observed in our three samples closest to failure. Several combinations are possible: a high-angle crack joining up with an axial crack array or network; two high-angle cracks joining, with or without a grain boundary in between; and two crack arrays or networks joining along a common grain boundary.



Figure 10

A set of cleavage cracks in biotite observed in P5. The mineral on the right is plagioclase. Maximum compression was vertical, and the scale bar at the top is 50 μm long.



We attempted to scan the samples at low magnifications of about 100X to locate areas with intergranular cracking extending over more than two grains. None was evident in H3; in P4 and P5 several such localized zones could be observed, and the details will be discussed in the next section.

The post-failure samples

Extensive intergranular cracking and localized deformation are evident in samples deformed further into the post-failure region. P4 has several areas with intergranular cracking extending over three or four grains, at angles roughly $\pm 30^\circ$ to σ_1 . The most extensive localized zone is comprised of 2 grain boundaries, 3 crack arrays in microcline, and 1 cleavage crack in biotite. The total length is about 2.3 mm. The continuous cracking was stopped at one end by a microcline grain with several short axial cracks, and at the other end by a biotite with (001) cleavage planes almost perpendicular to σ_1 .

In P5, two almost parallel localized zones are evident even under visual observation. The longer one extends over 4 grain boundaries, 3 microcline crack arrays, and 1 plagioclase cleavage crack (Figure 7). It was stopped at one end by a relatively uncracked quartz grain, and at the other end by a second quartz grain with a complex crack array similar to that in Figure 6. The total length is about 3.9 mm.

In P6, P7 and P8 several roughly parallel localized zones are evident visually. Some are longer than the others. Two outstanding zones each extending over about 10 mm can be seen in P6; the zones form an *en echelon* pattern with a separation of about 2 mm, and a small amount of overlap. In P7 and P8, only one prominent zone spanning over the entire sample (i.e. about 30 mm long) is observed in each specimen.

Our SEM observations on these samples clearly show that most of the micromechanical processes occurred along the localized zones. For a region two to three grains away from such a zone, the microstructures are qualitatively similar to features seen in P4 or P5 discussed above. We shall concentrate below on SEM observation of the localized deformation.

In general a localized zone consists of a set of almost collinear cracks at 15° to 45° to σ_1 , interrupted by axial crack arrays or networks. Substantial relative displacement along the high-angle cracks is usually evident, indicating that the cracks have undergone shear (Figures 7 and 11). The overall impression is that more shear cracks originate from grain boundaries than from favorably oriented cleavages in biotite or feldspar.

The axial crack arrays in quartz and microcline are very closely spaced, forming slender column-like structures.

Figure 11

Coalescence of a crack array in quartz (qtz) and a crack network in plagioclase (pg) with a grain boundary (g) to form a throughgoing fault in P7. The long axial cracks in quartz outline slender columns that were continuous and have "buckled" during the instability process, whereas not many well-defined elongated columns can be traced in the plagioclase grain. At high magnification, the longer cracks in the latter can be seen to be joining up with pores. Note the crushing into fine-grained particles along the fault. Maximum compression was vertical, and the scale bar at the top is 50 μm long.

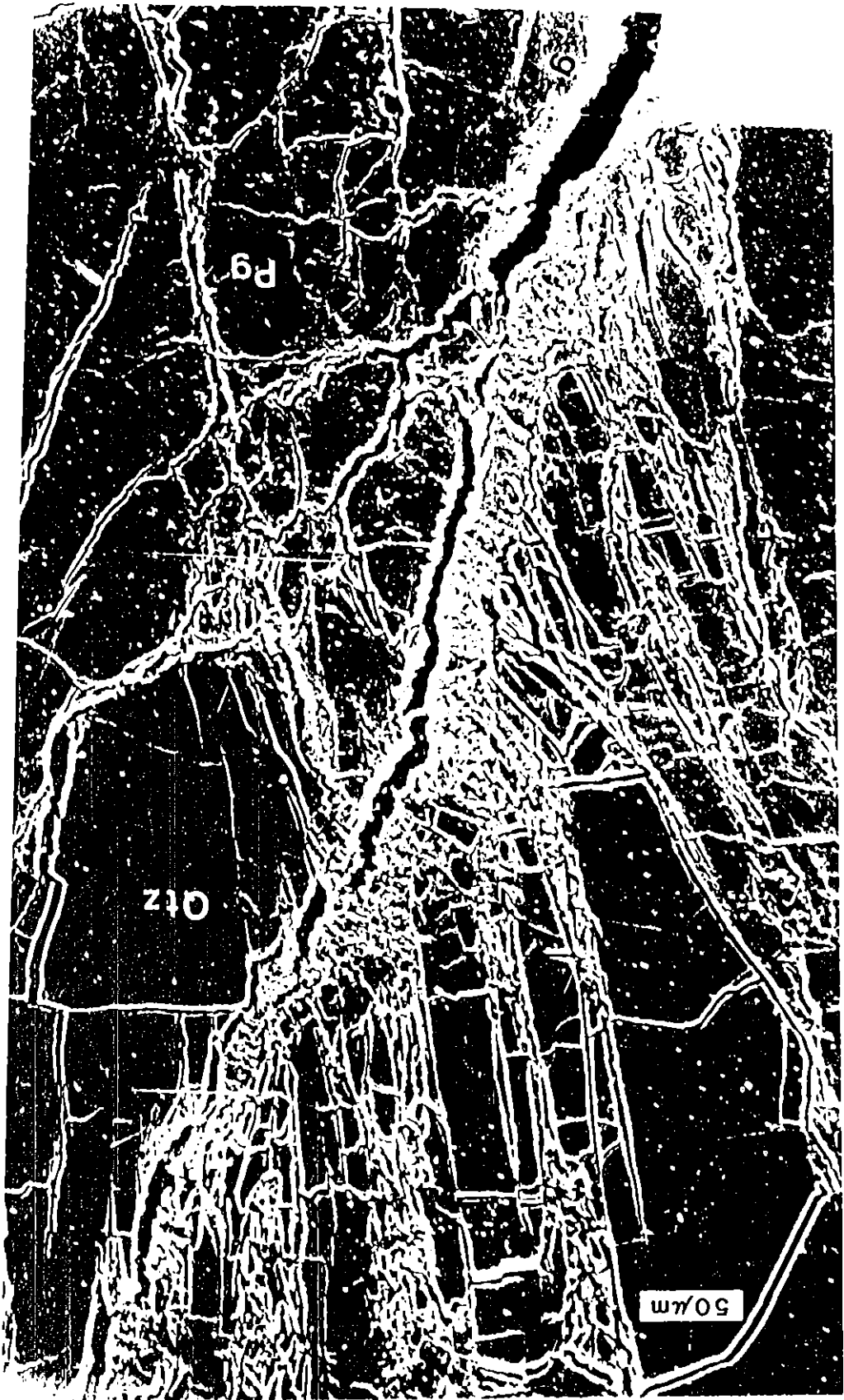


Figure 12

Coalescence of an axial crack array in a microcline grain to form part of the incipient fault in P7. At high magnification, the cracks can be seen to have propagated in a step-like manner, indicating that they are cleavage cracks. Maximum compression was vertical, and the scale bar at the top is 50 μm long.



Some finally reached an unstable configuration, and coalesced with the shear cracks. As shown in Figures 11 and 12, the mode of instability seems to be analogous to the buckling of columns, as was suggested by Peng & Johnson [28]. Extensive crushing into fine-grained particles occurred during and after coalescence.

On the other hand, not many well-defined elongated columns can be observed in plagioclase; instead, structures with almost equi-dimensional blocks separated by a complex crisscrossing crack network were usually observed (Figures 11 and 13). The mode of rupture seems to be more analogous to that of a discontinuous jointed structure in engineering geology (Goodman [29]) in which the shear zone propagation is accommodated by extensive rotation and crushing of the joint-blocks.

Kinking in biotite was quite commonly observed in P6, P7 and P8. It principally occurred in grains close to the localized zones, and is similar in appearance to Figure 5 of Tapponier & Brace [8].

P8 has a throughgoing fault with extensive gouge. Systematic electron microscopy work has been conducted on faulted Westerly granite by Stesky [30] and Tullis & Yund [31]; we therefore did not study this sample in great detail.

Figure 13

A complex crack network in plagioclase in P5. Notice how the cracks tend to join up with the pores. Two potential localized zones, one to the right and the other to the left of the scale bar, are seen to have formed diagonally across the grain. Maximum compression was vertical, and the scale bar at the top is 15 μm long.



DISCUSSION

Influence of anisotropy on development of stress-induced cracks

It is clear from our SEM observations on a complete suite of pre- and post-failure samples that several distinct micromechanical processes dependent on mineralogy and grain orientation are operative in faulting. Before discussing how the high-angle shear cracks and the low-angle crack arrays and networks can coalesce into a fault, it is important to first understand how they can initiate and develop.

Tapponier & Brace [8] have discussed how the SEM observations of low-angle transgranular cracks may be explained in term of internal stresses induced by grain scale inhomogeneity in elastic properties. They did not address the question of grain scale anisotropy, but Kranz [36] recently argued that most of the crack and pore morphology can be interpreted by linear elastic fracture mechanics results for an isotropic medium, and that anisotropy may not have significant consequence.

We show that in microcline, the more closely spaced axial crack arrays are usually along cleavages which suggests that at least for this mineral, anisotropy may have significant influence. We did a theoretical analysis to explore this; the mathematical details are given in the Appendix. We consider the internal stresses induced in an

anisotropic inclusion (with elastic moduli appropriate for quartz, plagioclase, or microcline) constrained by an isotropic matrix (with elastic moduli of Westerly granite). The ambient stress is fixed at $\sigma_1 - \sigma_3 = 4P$, $\sigma_2 = \sigma_3 = P$. The dependence of the induced stresses on orientations as predicted by the model is illustrated in Figure 14.

Among the three major minerals in the rock, microcline is the most anisotropic, followed by plagioclase and quartz. The calculation shows that the induced stress in microcline has the strongest dependence on orientation and the widest range of values. There are two perfect cleavages in the feldspars: (001) and (010); our calculation shows that the maximum differential stress is usually set up when one of the perfect cleavage planes is aligned parallel to σ_1 .

Several additional factors are involved in the development of stress-induced cracks. Given a stress field and a crack geometry, whether the crack will propagate or not depends on the value of the specific surface energy Γ . To our knowledge, two studies of specific surface energy in feldspars have been made: Brace & Walsh's [33] measurement on orthoclase and Atkinson's [32] on microcline, both of which show values at least twice those in quartz. Crack extension is therefore more favorable in quartz from a simplistic energetic consideration. However, it was concluded in both [8] and [9] that the extent of cracking is

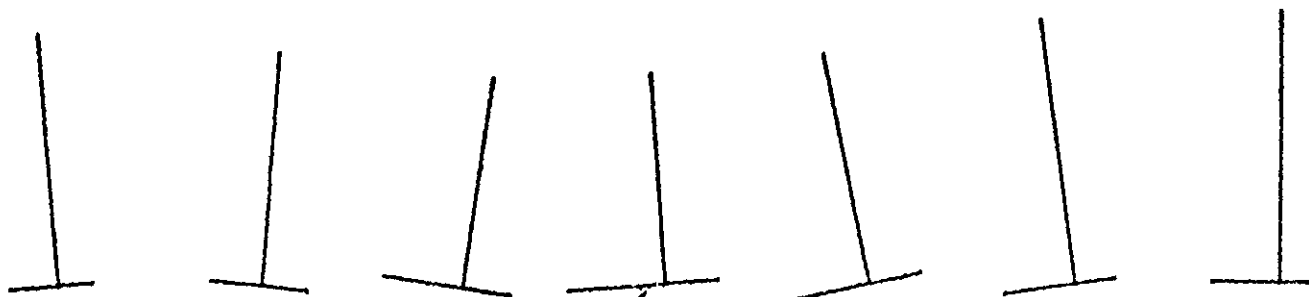
Figure 14.

The internal stresses induced in an anisotropic inclusion (of the three major minerals in Westerly granite). The scale is given by the ambient stress assumed in the calculation: $\sigma_1=5P$, $\sigma_2=\sigma_3=P$. At 15° increments of the angle of rotation (as defined in Table III), the principal stress values are represented by the three arms of an inverted T. The longest arm, which represents the maximum compression induced in the inclusion, is shown inclined to the vertical by the angle θ (also defined in Table III).

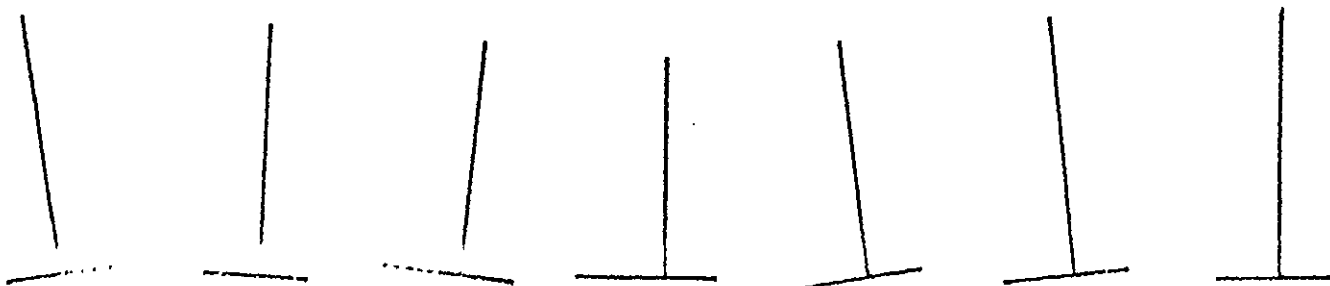
AMBIENT STRESS - Westerly granite



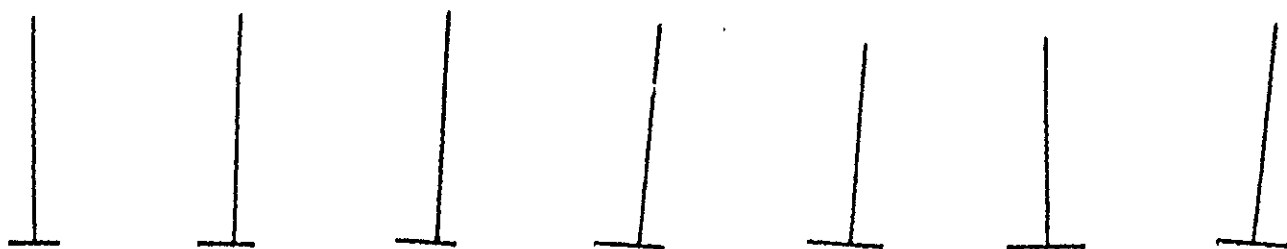
INTERNAL STRESS - Microcline



- Plagioclase



- Quartz



0

15

30

45

60

75

90

is about the same in the three major minerals, and our observations actually show that microcline seem to have longer and more closely spaced axial cracks.

Brace & Walsh [33] pointed out that the cleavage experiments on orthoclase usually result in "frayed splintery cleavage surfaces", and therefore the process may be too complicated for Gilman's theory they used to be applicable. Indeed, anisotropic fracture mechanics [34] shows that for a crack in a two-dimensional anisotropic body, the stress intensity factor is the same as in the isotropic case, but if the crack is close to the boundary of a finite body, the two are different and the anisotropic intensity factor is orientation dependent. In a cleavage experiment the dimensions are finite and the above effect is more pronounced as the crack lengthens. In a polycrystalline rock, many of the transgranular cracks start from grain interfaces and the influence of the boundary can also be appreciable. For the three-dimensional case, the situation is even more complicated, as illustrated by the recent theoretical analysis by Hoenig [35] of a penny-shaped crack in an anisotropic medium.

One would expect cleavage along the (001) or (010) plane to require a lower Γ than along other planes. The indentation data of Atkinson [32] show that, even between the perfect cleavages, microcline has a wide variation of specific surface energy: Γ is 2.27 Jm^{-2} for (001) and 4.92 Jm^{-2} for (010). It is likely that an even wider variation in Γ exists if all possible orientations are considered.

One can conclude that axial cracking along one of the perfect cleavages is a favorable mode of stress-induced crack development in the feldspars. Microcline is more anisotropic and we expect the effect to be more pronounced. However, a high anisotropy in elastic moduli coupled with an orientation dependence in Γ render it extremely difficult to predict the initiation and propagation path of stress-induced cracks for other grain orientations, and conclusions based on rule-of-thumb calculations useful in isotropic cases may not be applicable. A systematic study of the correlation between crack morphology and grain orientation using both optical and electron microscope, and refined measurements of Γ of the common minerals in different orientations should be useful in furnishing us a better understanding of this complicated problem.

The influence of pores in plagioclase

The analysis of the effects of elastic anisotropy discussed above is expected to be less applicable to plagioclase because it is less anisotropic than microcline. Few arrays of long axial cracks can be seen in plagioclase; instead, many thin cracks were observed emanating from pores and linking up to form complex networks. This suggests that the pores, most of which are found in plagioclase [3] may play a significant role. Model experiments on elastic plates were cited in [36] to interpret crack-pore

interaction. Recently, there have been a number of theoretical studies in ceramics science on this aspect. We shall summarize the relevant results and discuss how they may be useful in providing a unified picture of the possible roles of pores.

Walsh's [37] analysis shows that the effect of pressure on pores is small relative to that due to the differential stress in the range we are interested. Consider the effect of a differential stress $S = \sigma_1 - \sigma_3$: elastic analysis of a spherical pore loaded with remote uniaxial stress (e.g. [38]) shows that the maximum compressive hoop stress is at 90° to σ_1 direction equal to $\frac{24-15\nu}{14-10\nu} S$ and the minimum is at 0° equal to $-\frac{3(1+5\nu)}{2(7-5\nu)} S$ (negative sign indicates tension). Taking the Poisson ratio ν to be 0.2, the hoop stresses assume the values of $2S$ and $-0.5S$. Lajtai & Lajtai [39] performed model experiments in plaster blocks to illustrate such a stress concentration effect: tensile cracks parallel to σ_1 emanates from the top and bottom of a cavity, whereas compressive stress concentration along the equator results in localized cataclasis.

A crack emanating from a pore is similar to an edge crack in a half space: both have a high stress intensity factor K_I because the presence of a cavity surface enhances crack opening. Evans et al [40] and Green [41] analyzed the case of an annular crack of length a emanating from a spherical pore of radius r and subjected to a

tensile stress σ . They found that the normalized stress intensity factor K_I/K_p (where $K_p = 2\sigma\sqrt{a}/\sqrt{\pi}$ is the stress intensity factor of a penny-shaped crack of radius a) has a high asymptotic value of 3.52 when a/r is small and drops to 1 when a/r becomes greater than about 1. The stress field around a spherical pore drops off like $(\rho_0/\rho)^3$ (where ρ_0 is radius of the pore and ρ is radial distance from the center), and so the influence of the pore in perturbing both the stress-field and stress intensity factor becomes insignificant by the time the crack length reaches the dimension of the pore. Therefore pore-emanated cracks longer than a few pore dimensions can be treated as an ordinary crack.

However, there is an additional complication that the crack may be blunted by meeting another pore. Lange [42] analyzed this problem, and he showed that if the crack front of a penny-shaped crack (of radius a) is "pinned" by two impenetrable obstacles, the specific surface energy is increased to $(1 + 2a/3d)\Gamma$ where Γ is the intrinsic specific surface energy, and d the obstacle spacing. The value represents an upper bound for our case because a pore is not completely impenetrable and the effective blocking diameter is uncertain. For a fixed spacing of pores, we expect a penny-shaped crack with a large radius to have a higher probability of intersecting the pores,

and the increase in specific surface energy proportional to a/d acts as an energy barrier for further propagation. The stress concentration effect discussed above suggests that a large number of cracks will be found emanating from pores, and because of the enhancement of specific surface energy, these cracks will be relatively short.

We have suggested that some of the prominent microstructures in microcline and plagioclase can be interpreted as a consequence of the high elastic anisotropy in the former and the abundance of pores in the latter, and the absence of similar features in quartz can be explained by the relative isotropy and the absence of preferred cleavages or pores. In both analyses, we emphasize one type of inhomogeneity, and average the surrounding inhomogeneities by assuming an isotropic matrix. To what extent such an approach is appropriate, especially with respect to some of the more delicate features, remains to be investigated further.

The effects of pressure and temperature

The crack density data in Table II show that a higher proportion of high-angle cracks was observed at a higher pressure and temperature. Previous optical and SEM work at room temperature [10,14] concluded that application of pressure alone can also increase the number of high-angle cracks. Because the pressures used in these previous studies are both lower than what we used, and furthermore, the

crack counting procedures are different from ours, a quantitative comparison is not possible. The relative contribution of temperature and pressure towards the development of high-angle cracks can not be determined.

A semi-brittle mechanism such as high local tensile stresses induced by dislocation pile-up is usually proposed to be the process controlling the initiation of cleavage cracks in metals [43]. A theoretical analysis by Francois & Wilshaw [44] on the effect of pressure on this mechanism is sometimes cited in rock mechanics literature to interpret the effect of pressure on high-angle cleavage cracks. No evidence of plastic deformation was found by Durham & Martin [45] in quartz undergoing crack propagation at temperatures up to 250°C. Stesky [30] observed a marked increase in dislocation density in quartz above 500°C, and saw no sign of plasticity in feldspar in faulted samples of Westerly granite deformed at 250 MPa. Tullis & Yund [31] reported extensive dislocation motion at 300°-400°C for quartz and 550°-650°C for feldspar in faulted Westerly at pressures above 500 MPa. Most of the high-angle cleavage cracks we observed are in the feldspars, and the highest pressure and temperature we used is 400 MPa and 350°C respectively. On the basis of the transmission electron microscope work mentioned above, we can conclude that mechanisms involving dislocation pile-up should not

be important in our specimens, except possibly in grains neighboring biotite which yields at very low stress [46].

Even if we take into consideration the possible rotation of the stress tensor induced by grain scale anisotropy (see the Appendix), it is unlikely that the high-angle cleavage cracks up to 60° can form in a purely tensile mode. Not much is known about shear crack growth as a purely brittle process. Presumably the frictional coefficient along grain boundaries or cleavages and the specific surface energy under shear are two crucial parameters. The former can fluctuate according to experimental conditions [13], whereas to our knowledge no measurement exists for the latter. It is generally assumed in the engineering literature that the shear value should be higher, but a limited amount of data [47] presented recently suggests that it can be either higher or lower. The complications associated with interface cracks [48] may also be important for shear cracks along grain boundaries.

We expect that larger differential stresses are required for propagation of axial cracks at high pressures and that the frictional resistance along potential shear cracks would probably also increase. Indentation measurements of surface energy of quartz in one orientation by Atkinson [32] show no systematic variation of Γ with temperature: Γ decreases at 100°C and then increases with temperature up to 200°C . The effect of

temperature on friction is also unknown. The increase in high-angle cracks with pressure and temperature apparently depends on the trade-off among the various factors and the relative magnitude of specific surface energy in shear and in tension. Most of these is poorly understood, and further work is necessary before we can have a better understanding of the SEM observation.

The micromechanics of faulting

One major unsettled question regarding brittle fracture in rock is: how do the microcracks interact and coalesce into a macroscopic fault? Several conclusions can be drawn from our study of a complete suite of pre- and post-failure samples.

First, it is evident from our observations that brittle failure is a localization process. The more intense deformation features, such as the collapse of slender columns in quartz and microcline, the rotation and crushing of "joint-blocks" in plagioclase, the kinking in biotite, and the fine-grained gouge are all located in a zone 3-4 grains wide forming an incipient fault. Most of the microcracking in the post-failure region resolvable under the SEM is still in an axial direction. At later stages of deformation in the post-failure region, extensive crushing of particles into fine-grained gouge seems to be the principal energy

dissipation process. A more thorough analysis of the energetics of post-failure deformation is given in [27].

Second, we conclude that both axial and shear cracks both play significant roles in the localization process. We believe that we have identified most of the brittle failure mechanisms in Westerly granite by studying the deformation at a higher temperature and pressure than previous work. As emphasized above, we do not have specific information on the relative importance of the two types of cracks at a different pressure and temperature; however, the various mechanisms dependent on mineralogy and grain orientation we outline here should be quite general and can be operative as long as the deformation is in the brittle field.

An attempt to isolate one single dominating mechanism independent of mineralogy, and pressure, temperature condition as responsible for brittle faulting in rock is probably not a useful approach. In previous optical microscopy work on post-failure samples, Hallbauer et al [15] concluded that stress-induced cracks are predominantly *en echelon* cracks at low angles. This is understandable because the rock is monominerallic (a quartzite), and axial cracks are the only type of transgranular cracks we observed in quartz. Friedman et al [16] made optical observation on an incipient fracture extending 4.0 mm from one end of a test sample of Westerly granite loaded uniaxially to just before failure.

Over 75% of the incipient fault was parallel to cleavage planes or grain boundaries; for this reason, Friedman et al suggested that an incipient fault is formed by "irrational links between *en echelon* inclined grain boundaries and cleavages". Although the gross features in our sample P5 are similiar to their observations, we obtained a more comprehensive notion of the relative roles of the shear and axial cracks. A clearer picture of the process is possible because better resolution was achieved by ion-thinning the samples and by making both optical and SEM observations. Friedman et al's sample was retrieved immediately before failure, whereas P5 was obtained after failure. Rice [49] recently pointed that if shear constraint is high, the local stress field in the end region of a sample is closer to a plane strain condition than to an axi-symmetric compression, and theoretical calculation predicts that pre-failure localization is possible. In an uniaxial configuration the end constraint problem is more critical and it is therefore not surprising that a localized zone was found near the end of a pre-failure sample.

Third, an understanding of how the shear and axial cracks can interact mechanically is important for the formulation of a general theory of brittle fracture. Numerous attempts have been made to derive a fracture criterion for

rock, by only considering either isolated shear cracks (e.g. McClintock & Walsh [50]) or isolated set of *en echelon* axial cracks (e.g. Peng & Johnson [28]). The results are useful for understanding how instability comes about for the individual mechanism, but an assessment of the relative significance of the various mechanisms and understanding of their interactions is crucial if we are to understand the brittle failure of a polyminerallic rock over a wide range of temperature and pressure.

On the basis of our microscopic observations, we suggest the following sequence of failure in Westerly granite at 250 MPa, 150°C:

1. Most of the shear cracks at 15° to 45° to maximum compression direction have overcome the frictional resistance and extended to full length at some point in the pre-failure region.
2. Most of the axial crack arrays and networks can, however, still sustain differential stress, and act as "barriers" to linking up of a set of almost coplanar shear cracks. Any additional load imposed is supported solely by the "barriers". At failure, some "barriers" have reached an unstable configuration and those with the most critical geometry coalesce with neighboring shear cracks to form a localized zone.
3. The collapse of each "barrier" results in a stress drop, and the differential stress is transferred to other

"barriers" next to the localized zone, inducing some of them to collapse also, and the process is repeated.

4. After a "barrier" links up with neighboring shear cracks, the geometric irregularities that will interrupt the propagation of a planar throughgoing fault are crushed into fine-grained gouge. The process reduces the frictional resistance and results in further stress drop until finally the residual stress level is reached along the entire localized zone spanning the sample.

We cannot offer a detailed description of the instability mechanism for the axial crack arrays and networks. The bent geometry of the slender columns and the rotation within the networks strongly suggests that geometric instability is involved. An analysis requires some knowledge of the local stress field and the geometry. If interaction of shear and axial cracks proceeds as suggested above, most of the differential stress applied near failure is sustained by the "barriers", and the local stress can therefore be much higher than the ambient stress. Furthermore, it is well known that unloading can result in tension cracks almost perpendicular to σ_1 [51]. Since our control technique involves several unloading-loading cycles, some of the perpendicular cracks we observed may be due to the unloading and not to bending. It is difficult to obtain an unambiguous assessment of the critical geometry for instability on the basis of our SEM observation.

The question of localization

The theoretical analysis of strain localization in a continuum has been actively pursued in solid mechanics in the past decade. Rudnicki & Rice [19] generalized the constitutive equation of rock by incorporating a frictional (shear) and dilatational component in the inelastic strain. They showed that localization occurs well into the post-failure region at a steep softening slope for a wide range of frictional and dilatational parameters if the loading is axi-symmetric. Holography [17] and acoustic emission [18] work, however, revealed local concentration in strain and acoustic emission activity at the site of the eventual macroscopic failure just before peak stress. The SEM observation of this study also indicates strain localization almost immediately after failure.

Rice [49] suggested that shear constraint at the sample-piston interface can result in pre-failure localization. As discussed above, the effect may be significant in cases for which an incipient fault emanates from the end region, but the localized zones we observed are mostly away from the end. One possible explanation of the apparent discrepancy between theory and observation lies in the inadequacy of the continuum description. The constitutive equation formulated by Rudnicki & Rice [19] can be considered a good approximation over a continuum element large enough such that the inelastic strain can be characterized by just two parameters (shear and dilatation).

We observed a variety of mechanisms is involved in the failure process of Westerly granite, and so such a representative element has to include a combination of the major minerals and grain boundaries. Within this framework, localization occurs when a continuous shear band has formed in one representative element. As pointed out above, instability of crack arrays in quartz which makes up about one-third of the rock is not observed until at P6, and in this sense, localization did not occur at P5 but well into the post-failure region somewhere between P5 and P6.

Nevertheless, a continuum theory of shear localization such as that formulated in [19] has proved to be useful in presenting a unified view of faulting in rock and its dependence on elastic and inelastic parameters. It should be interesting to incorporate some of the new observations into a more elaborate constitutive equation, and hopefully, formulate a more comprehensive theory of brittle faulting.

CONCLUSION

(1) Our pre-failure samples show two different modes of deformation. Numerous transgranular cracks at low angles to the maximum compression direction were observed, similar to previous observation at room temperature. However, we also observed high-angle transgranular cracks, mostly

in feldspars and biotite, which often occur as an array of parallel cracks along cleavage planes. High angle cracks are absent in quartz.

(2) Stereological analysis of the crack count data shows that a sample deformed under high pressure, temperature condition has more high-angle cracks.

(3) A localized zone in a post-failure sample consists of almost coplanar shear cracks at angles of 15° to 45° to maximum compression direction. The shear cracks follow favorably oriented grain boundaries, or cleavages of feldspars and biotite. Elsewhere, arrays of axial cracks in the form of slender columns extend through entire grains. In plagioclase, complex networks of short cracks link up the abundant pores. Both arrays and networks interrupt the shear cracks; with further deformation, these "barriers" finally coalesce with the shear cracks into a fault. Kinking and folding are observed in the biotite, principally in grains close to the fault.

(4) Other than grain scale inhomogeneity cited in previous studies to explain local stress concentration, elastic anisotropy and pores both can influence the local stress field significantly, especially in the feldspars.

(5) Apparently the four minerals in Westerly granite all behave differently during faulting. An attempt to isolate one single dominating mechanism as responsible for brittle faulting may not, therefore, be a useful approach for this

rock. The limitation in a continuum description for such a complex process has also to be kept in mind if the theoretical predictions are to be applied in a meaningful way.

APPENDIX

Theoretical analysis of the effect of anisotropy on internal stresses

We describe here the inclusion model we used to determine the possible influence of anisotropy on the stress field within a grain of arbitrary orientation. We consider a spherical anisotropic inclusion with stiffness L_{ijkl} embedded in an effective medium with elastic stiffness L_{ijkl} . The medium is assumed to be isotropic:

$$L_{ijkl} = (K - 2G/3) \delta_{ij} \delta_{kl} + G (\delta_{ik} \delta_{jl} + \delta_{il} \delta_{jk})$$

where K and G are the bulk and shear modulus respectively, and δ_{ij} is the Kronecker delta.

On the basis of Eshelby's classic work [52], it can be shown that if a remote stress σ_{ij}^{∞} is imposed, the induced stress field would be homogeneous within such an inclusion, and is given by:

$$\sigma_{ij} = L_{ijkl} A^{-1}_{klmn} L^{-1}_{mnpq} \sigma_{pq}^{\infty}$$

where $A_{klmn} = I_{klmn} - S_{klmn} + S_{kl\alpha\beta} L^{-1}_{\alpha\beta\gamma\delta} L_{\gamma\delta mn}$

and A^{-1} and L^{-1} are inverses of the corresponding tensor satisfying the relationship $A_{klmn} A^{-1}_{mnpq} = I_{klpq} = 1/2 (\delta_{kp} \delta_{lq} + \delta_{kq} \delta_{lp})$; the S tensor is as defined by Eshelby, and for our case of a spherical inclusion in an isotropic medium, it takes the

simple form of:

$$15(1-\nu) [S_{jjjj}, S_{jjkk}, S_{jkjk}] = [7-5\nu, 5\nu-1, 4-5\nu]$$

(no summation).

There are several limitations in such a model. First, a sphere is by no means a realistic representation of the grain geometry. The actual internal stress field should therefore be more complicated than the homogeneous solution we obtained. Second, the actual constraint set up by the neighboring grains is also, much more complicated than the isotropic effective medium we assume here. However, since we are concerned only with the influence of anisotropy and grain orientation, it is justified to smooth out the geometric irregularities of the host grain and the inhomogeneity in elastic properties of the neighboring grains. The stress field we calculate should be useful for comparison purpose.

For the effective medium, we choose the following representative values of bulk behavior of Westerly granite: Young's modulus 70 GPa and Poisson ratio .2; the remote stress is assumed to be $\sigma_{11}^{\infty} = 5P$ and $\sigma_{22}^{\infty} = \sigma_{33}^{\infty} = P$. The three major minerals are all considered, and the elastic stiffness of quartz, microcline, and plagioclase (24%An) are from data compiled by McSkimin et al. [53] and Simmons & Wang [54] respectively.

A comprehensive treatment of the problem requires computation of the stress tensor (6 distinct components) over

all possible orientations (2 angles), and is too involved for our purpose. For the feldspars, we consider the rotation on a plane containing both the tensor x_2 and x_3 axes; the x_2 axis coincides with the crystallographic b axis, and since microcline and plagioclase are both pseudo-monoclinic with $\alpha = 90^\circ 18'$ and $93^\circ 10'$ [26], we can take the tensor x_3 axis to be the c axis for most practical purposes. This plane was chosen because the perfect cleavages in feldspar are on (001) and (010) and therefore they fall very closely to the x_1x_2 and x_1x_3 planes, In quartz, we consider rotation on the x_2x_3 plane. The x_3 plane coincides with the crystallographic c-axis. Brace [55] pointed out that in trigonal crystals, the x_2x_3 plane shows the widest variation in compliance.

Several aspects of this set of data are worth mentioning. First, a wider range of principal stress values is to be expected in microcline, to be followed by plagioclase and quartz. The differential stresses in microcline range from 2.6P to 6.1P, whereas for quartz the range is from 4P to 5.4P. A more anisotropic inclusion results in a stronger orientation dependence for the internal stress. Second, the maximum compression direction in the more anisotropic feldspars can be rotated by as much as 10° towards the closest cleavage plane. Furthermore, the highest differential stresses are found where σ_1 is almost parallel to one of the perfect cleavages. Third, the absolute values of the stresses are higher in the feldspars in our sample calculation. This comes in as a result of the effective medium moduli we chose

and the contrast in average elastic properties between the inclusion and the effective medium. Fourth, we have not considered the azimuthal rotation of the minimum compression direction which, judging from our preliminary calculations, can be significant for certain grain orientations with less symmetry. Lastly, elastic anisotropy by itself is not enough to induce a local tensile stress field within a spherical inclusion. Development of axial tensile cracks most probably depends on the local tensile stress field set up by local geometric irregularities together with elastic anisotropy.

TABLE I : Stress history of SEM samples

Sample *	σ_3 (MPa)	Temperature ($^{\circ}$ C)	$\sigma_1 - \sigma_3$ (GPa)
P0	250	151	0
P1	"	151	0.90
P2	"	151	1.16
P3	"	153	1.23
P4	"	150	1.22
P5	"	150	1.21
P6	"	151	1.15
P7	"	151	1.10
P8	"	152	0.77
H0	400	350	0
H1	"	349	1.27
H2	"	353	1.40
H3	"	355	1.50

* All specimens are 35 mm long and 19 mm in diameter, except for the post-failure samples (P4-8) which are 16 mm in diameter.

TABLE II : Crack density data

Sample	L^* , mm	$P_{L'}^{\perp}$ /mm	$P_{L'}^{\parallel}$ /mm	L_A , mm/mm ²	Ω_{12}
T8	63	3.61	2.62	5.11	.19
P3	100	5.43	4.38	7.94	.13
H3	38	8.06	6.86	11.97	.10

* Total length of test array.

TABLE III

A. The calculated induced stresses in feldspars

Angle of rotation*	$\sigma_{\alpha}/P\#$	σ_{β}/P	σ_{γ}/P	θ [@]
<i>Microcline</i>				
0°	1.2	0.9	6.2	4.5°
15°	1.3	1.2	5.9	-4.5°
30°	2.0	1.2	5.3	-7.7°
45°	2.5	1.3	5.1	3.7°
60°	2.1	1.3	5.8	11.7°
75°	1.8	1.0	6.6	7.7°
90°	1.7	0.8	6.9	0°
<i>Plagioclase</i>				
0°	1.4	1.3	6.5	9.4°
15°	1.6	1.3	6.3	-2.0°
30°	2.1	1.3	5.8	-5.8°
45°	2.5	1.3	5.4	0.8°
60°	2.1	1.3	5.8	7.9°
75°	1.7	1.3	6.4	6.0°
90°	1.5	1.2	6.6	0°

* The rotation is on the tensor x_2 - x_3 plane of the feldspars. The angle is measured between the x_3 and σ_1 directions: at 0° σ_1 is parallel to x_3 and therefore also parallel to the (010) cleavage plane; at 90° σ_1 is parallel to x_2 which is identical to the crystallographic \hat{b} axis.

Principal component of the induced stress tensor which is almost perpendicular to the plane of rotation.

@ Angle between the maximum compression induced within the feldspar inclusion (σ_{γ}) and the maximum ambient stress σ_1 : a positive value of θ indicates that σ_{γ} is rotated towards the x_2 (or \hat{b}) axis, and a negative value towards the x_3 axis.

TABLE III

B. The calculated induced stresses in quartz

Angle of rotation*	$\sigma_{\alpha}/P^{\#}$	σ_{β}/P	σ_{γ}/P	$\theta^{\textcircled{a}}$
0°	.6	.6	5.8	0°
15°	.8	.4	5.8	-0.6°
30°	1.0	.3	5.7	-2.7°
45°	1.1	.5	5.4	-4.7°
60°	1.1	.8	5.1	-4.0°
75°	.9	1.0	5.0	0.6°
90°	.8	.9	5.3	-5.0°

* The rotation is on the tensor x_2 - x_3 plane of quartz. The angle of rotation is measured between the x_3 (the crystallographic \hat{c}) axis and σ_1 direction: at 0° σ_1 is parallel to the \hat{c} axis, and at 90° σ_1 is parallel to the x_2 axis.

Principal component of the induced stress tensor which is exactly perpendicular to the plane of rotation.

Ⓐ Angle between the maximum compression induced within the quartz inclusion (σ_{γ}) and the maximum ambient stress σ_1 : a positive value of θ indicates that σ_{γ} is rotated towards the x_2 axis, and a negative value towards the \hat{c} axis.

REFERENCES

1. Brace, W.F., Silver, E., Hadley, K., and Goetze, C. A closer look at cracks and pores. Science, 178, 162-163 (1972).
2. Sprunt, E., and Brace, W.F. Direct observation of microcavities in crystalline rocks, Int.J.Rock Mech.Min.Sci., 11, 139-150 (1974).
3. Montgomery, C.W., and Brace, W.F., Micropores in plagioclase, Contrib. Miner. Petrol. 52, 17-28 (1975).
4. Richter, D., and Simmons, G., Microcracks in crustal igneous rocks: microscopy in The Earth's Crust, A.G.U. monograph 20 (1977).
5. Hadley, K., Comparison of calculated and observed crack densities and seismic velocities in Westerly granite, J. Geophys. Res., 81, 3484-3494 (1976).
6. Brace, W.F., Permeability from resistivity and pore shape, J. Geophys. Res. 82, 3343-3349 (1977).
7. Sprunt, E., and Brace, W.F., Some permanent structural changes in rocks due to pressure and temperature, Proc. 3rd Intl. Cong. Rock Mechanics, Denver, Vol. II, Part A, 524-529 (1974).
8. Tapponier, P., and Brace, W.F., Development of stress-induced microcracks in Westerly granite, Int.J.Rock Mech. Min.Sci., 13, 103-112 (1976).
9. Kranz, R.L., Crack growth and development during creep in Barre Granite, Int.J.Rock Mech.Min.Sci., 16, 23-26 (1979).

10. Kranz, R.L., The effects of confining pressure and stress difference on static fatigue of granite, J. Geophys. Res., 85, 1854-1866 (1980).
11. Batzle, M., Simmons, G., and Siegfried, R.W., Microcrack closure in rocks under stress, in press J. Geophys. Res. (1980).
12. Brace, W.F., Direct observation of dilatant voids in rock, in The Effects of Voids on Material Deformation, A.S.M.E. monograph I-12 (1976).
13. Paterson, M.S., Experimental Rock Deformation - The Brittle Field, Springer Verlag, N.Y. 254pp (1978).
14. Wawersik, W.R., and Brace, W.F., Post-failure behavior of granite and diabase, Rock Mech., 3, 61-78 (1971).
15. Hallbauer, D.K., Wagner, H., and Cook, N.G.W., Some observations concerning the microscopic and mechanical behavior of quartzite specimens in stiff triaxial compression tests, Int. J. Rock Mech. Min. Sci., 10, 713-726 (1973).
16. Friedman, M., Perkins, R.D., and Green, S.J., Observation of brittle deformation features at the maximum stress of Westerly granite and Solenhofen limestone, Int. J. Rock Mech. Min. Sci., 7, 297-306 (1970).
17. Soga, N., Mizutani, H., Spetzler, H., and Martin, R.J. III, The effect of dilatancy on velocity anisotropy in Westerly granite, J. Geophys. Res., 83, 4451-4458 (1978).
18. Lockner, D.A., and Byerlee, J.D., Microfracturing and velocity changes during creep in granite, E/S, Trans. Am. Geophys. Union, 59, 1207 (1978).

19. Rudnicki, J.W., and Rice, J.R., Conditions for the localization of deformation in pressure sensitive dilatant materials, J.Mech.Phys.Solids, 23, 371-394 (1975).
20. Wong, T.F., The effects of temperature and pressure on failure and post-failure behavior of Westerly granite, [Chapter 1] (1980).
21. Aufmuth, R.E., and Aleszka, J.C., A SEM investigation of statically loaded foundation material, Bull.Asso.Engr. Geol., 13, 137-147 (1976).
22. Brace, W.F., Some new measurements of linear compressibility of rocks, J.Geophys.Res., 70, 391-398 (1965).
23. van der Molen, I., Some physical properties of granite at high pressure and temperature, Ph.D.thesis, Aust. Nat.Univ. (1979).
24. Wong, T.F., and Brace, W.F., Thermal expansion of rocks: some measurements at high pressure, Tectonophysic, 57, 95-117 (1979).
25. Hadley, K., Dilatancy in rock at elevated temperatures, EoS Trans.Am.Geo.Union, 56, 1060 (1975).
26. Deer, W.A., Howie, R.A., and Zussman, J., An Introduction to The Rock-forming Minerals, 528 pp, Longman, London (1975).
27. Wong, T.F., Shear fracture energy of Westerly granite from post-failure behavior, [Chapter 3] (1980).
28. Peng, S.S., and Johnson, A.M., Crack growth and faulting in cylindrical specimens of Chelmsford granite, Int.J.Rock Mech.Min.Sci., 9, 37-86 (1972).

29. Goodman, R.E., Methods of Geological Engineering, 472 pp, West, St.Paul, (1976).
30. Stesky, R.M., Mechanism of high temperature frictional sliding in Westerly granite, Can.J.Ear.Sci., 15, 361-375, (1978).
31. Tullis, J. and Yund, R.A., Experimental deformation of dry Westerly granite, J.Geophys.Res., 82, 5705-5718 (1977)
32. Atkinson, B.K., Compilation of Experimentally Determined Fracture Mechanics Parameters for Geological Materials, Final technical report to U.S.Natl.Earthquake Hazards Reduction Program (1979).
33. Brace, W.F., and Walsh, J.B., Some direct measurements of the surface energy of quartz and orthoclase, Am.Minera., 47, 1111-1122 (1962).
34. Cook, T.S., and Rau, C.A.Jr., A critical review of anisotropic fracture mechanics, in Prospects of Fracture Mechanics, Noordhoff, Leyden (1974).
35. Hoenig, A., The behavior of a flat elliptical crack in an anisotropic elastic body, Int.J.Solids Structures, 14, 925-934 (1978).
36. Kranz, R.L., Crack-crack and crack-pore interactions in stressed granite, Int.J.Rock Mech.Min.Sci., 16, 37-48 (1979).
37. Walsh, J.B., The effect of cracks on the compressibility of rocks, J.Geophys.Res., 70, 381-389 (1965).
38. Varḍar, O., Finnie, I., Biswas, D.R., and Fulrath, R.M., Effect of spherical pores on the strength of a polycrystalline ceramic, Int.J.Fracture, 13, 215-223 (1977).

39. Lajtai, E.Z., and Lajtai, V.N., The collapse of cavities, Int. J. Rock Mech. Min. Sci., 12, 81-86 (1975).
40. Evans, A.G., Biswas, D.R., and Fulrath, R.M., Some effects of cavities on the fracture of ceramics: I, Cylindrical cavities; II, Spherical cavities, J. Am. Ceram. Soc., 62, 95-106 (1979).
41. Green, D.J., Stress intensity factor estimates for annular cracks at spherical voids, J. Am. Ceram. Soc., 63, 342-344 (1980).
42. Lange, F.F., The interaction of a crack front with a second-phase dispersion, Phil. Mag., 22, 983-992 (1970).
43. Lawn, B.R., and Wilshaw, T.R., Fracture of Brittle Solids, 204pp, Cambridge U.P., Cambridge (1975).
44. Francois, D., and Wilshaw, T.R., The effect of hydrostatic pressure on the cleavage fracture of polycrystalline materials, J. App. Phys., 39, 4170-4177 (1968).
45. Martin, R.J. III and Durham, W.B., Mechanism of crack growth in quartz, J. Geophys. Res., 80, 4837-4844 (1975).
46. Etheridge, M.A., Hobbs, B.E. and Paterson, M.S., Experimental deformation of single crystals of biotite, Contrib. Miner. Petrol., 38, 21-36 (1973).
47. Liebowitz, H., Eftis, J., and Jones, D.L., Some recent theoretical and experimental developments in fracture mechanics, Fracture Vol. I, ICF 4, Canada, 695-727 (1977).
48. Comninou, M., and Schmueser, D., The interface crack in a combined tension-compression and shear field, J. App. Mech., 46, 345-348 (1979).

49. Rice, J.R., The mechanics of earthquake rupture, Proc. of Intl. School of Physics "Enrico Fermi", Course LXXVIII, on Physics of the Earth's Interior, E. Boschi, ed. (1979).
50. McClintock, F.A., and Walsh, J.B., Friction on Griffith cracks in rocks under pressure, Proc. 4th U.S. Natl. Congr. Appl. Mech., New York, A.S.M.E., 1015-1021 (1962).
51. Boland, J.N., and Hobbs, B.E., Microfracturing processes in experimentally deformed peridotite, Int. J. Rock Mech. Min. Sci., 10, 623-626 (1973).
52. Eshelby, J.D., The determination of the elastic field of an ellipsoidal inclusion, and related problems, Proc. Roy. Soc. London, Ser. A., 241, 376-396 (1957).
53. McSkimin, H.J., Andreatch, P., Jr., and Thurston, R.N., Elastic moduli of quartz versus hydrostatic pressure at 25°C and -195.8°C., J. Appl. Phys., 36, 1624-1630 (1965).
54. Simmons, G., and Wang, H., Single Crystal Elastic Constants and Calculated Aggregate Properties: A Handbook, 370 pp. M.I.T. Press, Cambridge (1971).
55. Brace, W.F., Orientation of anisotropic minerals in a stress field: Discussion, GSA Memoir 79, 9-20 (1960).

CHAPTER 3

SHEAR FRACTURE ENERGY OF WESTERLY GRANITE FROM POST-FAILURE
BEHAVIOR

INTRODUCTION

One of the important goals of both seismology and rock mechanics is a better understanding of faulting. Seismologists have traditionally characterized the faulting process by a number of "source parameters", such as permanent slip, rupture velocity, or rise time, the values of which are determined through inversion of seismic data. Such an approach has greatly enhanced our understanding of certain aspects of the seismic source, but it has a major shortcoming of being only a kinematic description: the parameters are not directly related to the physics of the rupture process, and some of the slip functions, although they can fit observations, are physically unacceptable [Aki & Richards, 1980].

To address the source dynamics directly, one is hampered by the limited knowledge of the actual failure process. Nevertheless, a number of theoretical results have been obtained by adapting techniques from fracture mechanics and assuming physically plausible fracture criteria. These have helped to establish a more precise conceptual framework for the analyses of the source mechanism. As reviewed by Freund [1979], Aki & Richards [1980] and Rudnicki [1980] such an approach has been shown to be useful on a number of dynamic and quasi-static problems in fault mechanics.

A fundamental quantity used in all these models is the

fracture energy or critical energy release rate, G . Physically, this quantity represents the energy flux for "breakdown" processes at a crack tip, and is the crucial parameter that constrains the energetics at the crack tip [Rice, 1979]. Lacking detailed knowledge of the rupture process, the value of G is the minimum amount of information required for any meaningful modelling of the source dynamics.

Unfortunately, laboratory studies have not been of much help in placing bounds on the magnitude of the shear fracture energy. With engineering applications in mind, most fracture mechanics techniques have been developed for the tensile mode [Freiman, 1979]. Likewise the measurements on minerals and rocks are done in tension (Table IB). Rice [1979] recently suggested that the shear G can be evaluated by performing an appropriate integration under the post-failure stress-displacement curve. He further showed that values so determined from room temperature data are closer to seismologically inferred values (Table IA) than the laboratory measurements obtained in tension, although a maximum discrepancy of three orders of magnitude may still exist.

Can temperature effect account for this discrepancy? How about the effects of pressure and strain rate? It would clearly be of interest to apply the technique to a variety

of rocks under geologically interesting conditions. We have recently completed a series of experiments on the post-failure behavior of Westerly granite at temperature to 700°C and pressure to 250 MPa (Chapter 1); here we shall discuss the results on \underline{G} as determined from our data using Rice's scheme, and compare the values with others evaluated from existing room temperature post-failure data.

If \underline{G} so determined truly represents the shear fracture energy for the failure processes, a portion of it should be attributed to processes associated with microcracking. The \underline{G} values determined by Rice for both intact and pre-fractured samples at room temperature were of the order 10^4 Jm^{-2} (Table II), whereas previous measurements invariably showed that the tensile fracture energy for minerals is of the order 1 Jm^{-2} and for pre-cracked rock samples of the order 10 Jm^{-2} (Table IB). An estimate of the microcrack surface area created in the post-failure stage is available from our previous scanning electron microscope work (Chapter II). This area multiplied by the single crystal fracture energy gives an estimate of the total energy input for microcracking processes, which should be a lower bound on \underline{G} . How do the two independent estimates compare? Can we gain some insight into the energetics of faulting in initially intact samples by making such a comparison?

There has been a certain amount of confusion in the literature concerning the physical meaning of tensile fracture energy measurements with respect to seismologically inferred G values; hopefully, the discussion here will clarify the relationship between the tensile and shear fracture energy, and between laboratory measurements and seismologically inferred values.

THEORY

Inelastic energy dissipation in pre-failure region

To put the latter discussion of fracture energy in perspective, we first estimate the energy associated with pre-failure inelastic processes. Let the stress field be given by σ_{ij} . For an increment of strain $d\epsilon_{ij}$, part of which ($d e_{ij}$) is attributed to elastic deformation and the rest to inelastic deformation, energy input per unit volume for inelastic processes will be given by:

$$dW = \sigma_{ij} (d\epsilon_{ij} - d e_{ij})$$

In a triaxial test, with maximum compression given by σ_1 and $\sigma_2 = \sigma_3 = P$ the above relation becomes:

$$\begin{aligned} dW &= \sigma_1 (d\epsilon_1 - d e_1) + 2P(d\epsilon_3 - d e_3) \\ &= \sigma (d\epsilon_1 - d e_1) + P(d\epsilon_v - d e_v) \end{aligned}$$

where the differential stress $\sigma = \sigma_1 - \sigma_3$, and the volumetric strain $\epsilon_v = \epsilon_1 + 2\epsilon_3$, $e_v = e_1 + 2e_3$. Note that ϵ_v is positive for compression and negative for dilatation; compressive stress is taken to be positive.

For most brittle rocks, the onset of dilatancy marks the point beyond which $d\varepsilon_{ij}$ and de_{ij} are significantly different. Following the notation in Brace et al [1966], if C' denotes the differential stress at the onset of dilatancy, C the fracture stress, and D the inelastic dilatation at failure, then the total inelastic energy input per unit volume in the pre-failure stage is given by:

$$W = \int_{C'}^C \sigma (d\varepsilon_1 - de_1) - P \cdot D \quad (1).$$

Determination of G from post-failure curve

Most previous studies of post-failure behavior interpreted the results in term of a classification first proposed by Wawersik [Wawersik & Fairhurst, 1970; Wawersik & Brace 1971], who showed that the post-failure response of certain rock types is so unstable that the load-displacement curves can actually turn over so far as to take on a positive slope. Wawersik categorised this type of behavior as class II, in contrast to the more stable class I behavior with persistently negative post-failure slope. Whereas class I behavior can be observed in a stable manner by using a sufficiently stiff machine, class II rocks will fail explosively even if the stiffness is infinitely high, unless steps are taken to servo-control the testing machine, either mechanically by a feedback loop [Hudson et al, 1972] or manually [Wawersik & Brace 1971].

Such a classification of the post-failure behavior is in essence a scheme to differentiate between two types of machine-sample interaction in terms of the relative magnitudes of stiffness. Does a critical change in sample stiffness represent a qualitative transition in physical characteristics? It is generally accepted that the stiffness is the natural parameter for characterizing the elastic deformation in the testing system; for the rock sample, however, the situation is not so clear. The stiffness is a quantity that depends on the Young's modulus and sample geometry, and even for the pre-failure deformation it is generally accepted that the stress-inelastic volumetric strain curve is preferred to the axial stress-strain curve for characterizing the physical processes. For the post-failure deformation, the strain field can be highly heterogeneous. Consider a sample stressed triaxially as shown in Figure 1. Previous microscope [Wawersik & Brace, 1971; Hallbauer et al 1973], acoustic emission [Lockner & Byerlee, 1978], and holography [Soga et al, 1978] studies have shown that close to the peak stress, a localized zone F is formed at an angle θ to the maximum compression direction (σ_1).

The question of whether localization occurs in the pre- or post-failure stage is not yet settled [Rice, 1979]; with this reservation in mind, we shall assume for convenience in the analysis below that it occurs right at the peak stress.

Most of the deformation is taken up by shear along F, and it seems logical to characterize the post-failure processes by the stress and slip along the localized zone (which is, of course, the routine procedure for the analysis of friction in pre-fractured specimens). The shear traction along F (Figure 1a) is given by:

$$\tau = \frac{\sigma_1 - \sigma_3}{2} \sin 2\theta$$

whereas the relative slip Δu at a point B (Figure 1b) can be expressed in term of the post-failure axial displacement $\Delta \ell$ by:

$$\Delta u = \Delta \ell / \cos \theta.$$

The calculation of $\Delta \ell$ is based on the observation that up to the failure stress, the unloading response can be approximated by the elastic modulus in most cases [Wawersik & Brace, 1971]. At the high pressures we used, the initial loading curve is linear and can be used to estimate the modulus.

The transformation of a post-failure stress-strain record to a $\tau - \Delta u$ plot is outlined in Figures 1b and 1c. It can easily be shown that the transition from class I to II occurs when the slope reaches the critical magnitude:

$$(\tau / \Delta u)^* = (E / \ell) \sin^2 \theta \cos \theta$$

where E is Young's modulus and ℓ the sample length. Within such a framework, the slope of the $\tau - \Delta u$ curve is always negative, and the class I to II transition is merely a gradual change.

The "slip-weakening" concept has been proposed to model the mechanics of this broad class of materials for which the shear strength degrades with relative slip. Generalizing Barenblatt's [1962] "cohesive zone" model originally intended for tensile cracks, Ida [1972] and Palmer & Rice [1973] independently suggested the use of analogous fracture mechanics ideas in the analysis of slip propagation under shear. A succinct discussion of the topic has been recently given by Rice [1979]; there is no need to repeat the details here. Applying rigorous arguments involving J-integral [Rice, 1968] to the "slip-weakening" model, it can be shown that the shear fracture energy

$$\underline{G} = \int_0^{\Delta u^*} [\tau(\Delta u) - \tau^f] d(\Delta u) \quad (2)$$

where Δu^* is the relative slip corresponding to the final residual stress τ^f . A graphic representation of this relation is shown in Figure 1c: \underline{G} is simply the hatched area under the τ - Δu curve. (Note \underline{G} is twice the specific surface energy as used in previous laboratory [Brace & Walsh, 1962] and seismological [Husseini et al, 1975; Aki & Richards, 1980] work.)

The derivation of \underline{G} assumes a crack-like mode, with breakdown processes at the tips given by the derived τ - Δu relation, whereas the situation in cm-size specimens,

whether initially intact or pre-fractured, is closer to an almost simultaneous slip along the localized zone or pre-existing fault (Figure 2). It has been suggested that the latter may involve the breakdown of asperities [Byerlee, 1967], whereas our SEM observations on post-failure samples (deformed at 250 MPa and 150°C) also indicated that the failure process involved slip along an array of shear cracks interrupted by "barriers" of *en echelon* axial cracks (Chapter 2). The expression, though an approximation, should be valuable for order-of-magnitude estimates. Note also that τ^f is explicitly subtracted from the integrand, and therefore \underline{G} does not include any contribution from the residual shear stress.

Two other parameters can be determined from the post-failure curves. A characteristic length for the breakdown slip $\overline{\Delta u}$ can be defined by the following (Figure 2):

$$\underline{G} = (\tau^p - \tau^f) \overline{\Delta u} \quad (3)$$

and the breakdown zone size ω_0 is given by:

$$\omega_0 = \frac{9\pi}{16(1-\nu)} \overline{\Delta u} \frac{\mu}{\tau^p - \tau^f} \quad (4)$$

where μ and ν are shear modulus and Poisson's ratio respectively. Unlike \underline{G} and $\overline{\Delta u}$, ω_0 is strongly dependent on the geometry and details of the slip-weakening process; the above expression for ω_0 is valid for slip propagation at the tip of a semi-infinite fault, with a further assumption that the τ - Δu relation is linear.

Estimation of the energy for stress-induced cracking

If we have a means of estimating the surface area per unit volume (S_V) of stress-induced cracks, the product of S_V with twice the specific surface energy (2Γ) gives an estimate of energy input per unit volume for microcrack formation.

A direct measurement of S_V is not practical since it would require three-dimensional observation of microcracks at high resolution. Most microscopic studies are performed on plane sections, and one has to resort to geometric probability theory [Kendall & Moran, 1963; Underwood, 1970] to estimate S_V from measurement of crack length per unit area (L_A) on sections. The measurement of L_A has been described in Chapter 2, and the stereological formulae relating the SEM data to S_V are summarized in the Appendix.

As noted above, $\underline{G} = 2\Gamma$ by definition; we shall use Γ here only for the values associated with microcrack extension, and reserve \underline{G} to denote the energy for macroscopic shear fault formation. For brittle deformation, most of the stress-induced cracks observed under SEM form in tension [Tapponier & Brace, 1976; Kranz, 1979; Chapter 2], and therefore specific surface energy measurements on single crystals in the tensile mode [Brace & Walsh, 1962; Atkinson, 1979] are the appropriate values to input for Γ . However,

we also pointed out in Chapter 2 that at higher pressures and temperatures, a larger portion of shear cracks was observed, and that to our knowledge, no measurement of Γ in shear has been made. It was also suggested by Friedman et al [1972] that Γ for grain boundary cracks might be lower, but again no measurement is available. Nevertheless, it is unlikely that in either of these cases, the value would be different from the tensile value by orders of magnitude. The estimate below gives the energy required to create the stress-induced crack surfaces observed under SEM, and does not include energy dissipation from sources such as friction along the crack surfaces.

If we denote the crack surface per unit volume in a virgin sample by S_V^0 , and that in a pre-failure stressed sample by S_V , then the energy per unit volume for microcracking will be:

$$M = 2\Gamma (S_V - S_V^0) \quad (5)$$

Let the crack surface per unit volume in a sample retrieved immediately after failure be S_V^f and that in a post-failure sample be S_V^p , the measurements being made in representative sections perpendicular to the localized zone. If the zone can be approximated by a planar zone with thickness w , then an estimate of the microcracking energy per unit area along the localized zone will be:

$$M^1 = 2\Gamma (S_V^p - S_V^f) w \quad (6)$$

Note that M is in Jm^{-3} whereas M^1 is in Jm^{-2} .

Determination of G of earthquakes

Rice [1979], Aki & Richards [1980] and Rudnicki [1980] have discussed in some length how to determine \underline{G} from seismological data. One formula frequently used is of the form:

$$\underline{G} = \frac{R (\Delta\tau)^2}{\alpha \pi \mu} \quad (7)$$

where R is the characteristic radius of the fault;

$\Delta\tau$ is the stress drop;

μ is the shear modulus.

This is the equation used by both Hussein et al. [1975, 1976] and Aki [1980] to determine \underline{G} for the Parkfield earthquake. α is a constant dependent on the details of the faulting process. Hussein et al. took $\alpha = 1$, whereas Aki determined α from a relationship involving the rupture velocity, seismic compressional and shear velocities.

A number of techniques have been proposed for determining the input parameters in equation (7). Hussein et al. estimated the two parameters, R and $\Delta\tau$, from seismic moment and corner frequency on the basis of Brune's [1970, 1971] model. Aki determined R from spatial distribution of after-shocks and assumption of existence of barriers along the fault, and $\Delta\tau$ from strong motion data.

Approaches different from (7) can also be used, e.g. Rice & Simons [1976] determined \underline{G} from the spatial distribution of slip for a fault creep event, and Rudnicki [1980] determined \underline{G} for the initiation of the 1857 California earthquake from geodetic data and historical record of earthquake recurrence time.

RESULTS

Pre-failure data

As shown in equation (1), to determine the inelastic energy input for pre-failure deformation one needs measurements of both the axial and volumetric strain; the latter was not monitored in our high temperature experiments, and hence we can only consider room temperature results. Since some detailed SEM data are available from Tapponier & Brace's [1976] study of Westerly at 50 MPa pressure, we will make the comparison on the basis of their data.

Following the notation of (1) and referring to Figure 1 of Tapponier & Brace [1976], we have $C'=250$ MPa, $C=530$ MPa, $P=50$ MPa and $D=3 \times 10^{-3}$. They did not show the axial stress-strain curve, but since the inelastic axial strain does not vary as much as D from sample to sample, we estimated the integral in (1) based on a similar experiment at $P=51$ MPa and with $C'=360$ MPa, $C=620$ MPa. The integral was estimated to be $2.1 \times 10^5 \text{ Jm}^{-3}$, and substituting into (1) we obtain a value for W of $6 \times 10^4 \text{ Jm}^{-3}$. Brace et al [1966] pointed out the determination of C is accurate to a few percent and of C' 10 to 15%, and D probably only to a factor of 2. Considering the additional error in computing the integral, we assign an uncertainty of 50% to the calculation of W .

We reproduce Tapponier & Brace's SEM data on a virgin sample (T0) and a sample close to failure (T5) in Table III.

They counted the number of crack intersections per unit length perpendicular (P_L^\perp) and parallel (P_L^\parallel) to σ_1 . Note that their measurements on T5 are higher than ours as tabulated in the Appendix because we used a larger array spacing and the pores were excluded in our counts. We show in the Appendix that the crack orientations in pre-failure samples can be approximated quite well with an axisymmetric distribution with one single preferred orientation (σ_1), and that the crack surface per unit volume can be estimated from the equation : $S_V = 1.571P_L^\perp + .429P_L^\parallel$. The calculated values are shown in Table III; referring to equation (5), we therefore have: $S_V = 16.35 \text{ mm}^2/\text{mm}^3$ and $S_V^0 = 9.68 \text{ mm}^2/\text{mm}^3$. 2Γ in quartz and feldspars ranges from 1 Jm^{-2} to 10 Jm^{-2} [Brace & Walsh, 1962; Atkinson, 1969]. A reasonable estimate of M is therefore 6.67×10^3 to $6.67 \times 10^4 \text{ Jm}^{-3}$.

Post-failure data

Two series of post-failure experiments at 80 MPa and 250 MPa were performed; the details have been described in Chapter 1. In addition, a number of room temperature post-failure studies has been reported in the literature. G for Westerly granite [Wawersik & Brace, 1971; Chapter 1] and Oshima granite [Sano, 1978] were calculated by us; that for Fichtelgebirge granite [Rummel et al, 1979] was calculated by Rice [1979]. (Table II and Figure 3) Values of $\overline{\Delta u}$ and ω_0 were also computed; all calculations are based on equations (2), (3), and (4).

The lower limit of integration in (2) depends on our picks of the residual stress level (τ^f). As is evident from the post-failure data in Chapter 1, the transition to stable sliding is rather gradual owing to the tendency of the jacket to hinder the sliding motion. This is the major source of experimental error. Taking into consideration the error due to numerical integration, we judge the estimation of \underline{G} to be accurate probably within a factor of two.

To independently determine a lower bound for \underline{G} , we counted the cracks under the SEM for three post-failure samples from our previous study (Chapter 2). The samples P4, P6 and P7 were all deformed at 150°C and 250 MPa; the SEM data are analyzed in the Appendix and tabulated in Table IV. Referring to Figure 1 in Chapter 2, P4 is a sample retrieved immediately after failure, whereas P6 and P7 experienced a differential stress drop of about 75 MPa and 120 MPa respectively. The total stress drop to reach the residual stress level is about 350 MPa.

In P4, several areas with intergranular cracking extending over 3 or 4 grains can be located. We counted the cracks in a mosaic covering a localized zone of length of about 2.3 mm. A more detailed description of this

area was given in Chapter 2; as pointed out there, the zone was the most extensive one we located in the sample, and the crack counts should be higher than the average value in the sample. We chose for P6 a representative area along one of the two prominent localized zones, which is comprised of a mixture of shear cracks, and crack arrays and networks. It was obvious at high magnification (above 1,000X) that crushing into fine-grained particles started to occur along portions of the localized zone in P6, and extensive crushing in P7 was obvious even at 300X. For P7, we counted the cracks as seen on two more "intact" areas along the incipient fault comprising of all three major minerals. An unambiguous count of the cracks at a reasonable magnification along the "crushed up" areas is impossible, and we expect our estimates for both P6 and P7 to be lower than the average value along the localized zone.

As discussed in the Appendix, the crack intersections per unit length data in the post-failure samples P4 and P6 can be reasonably represented as

$$P_L(\theta) = a + b\sin\theta + c \sin|\theta - \omega|$$

where θ is the angle between the test array and σ_1 , and ω that between the localized zone and σ_1 . Since the count in P7 was done on areas not quite representative of the localized zone (most of which tended to be more

crushed) , a detailed knowledge of $P_L(0)$ as seen on the mosaic would not be of much physical significance. We therefore only measured P_L in two orthogonal directions and used equation (A4) to estimate the crack length per unit area (L_A). For P4 and P6 we used the following relationship: $L_A = \pi a/2 + b + c$; the crack surface per unit volume was then estimated by $S_V = L_A$. (For details, refer to the Appendix).

The calculated values are tabulated in Table IV and referring to equation (6), we have: $S_V^f = 15.91 \text{ mm}^2/\text{mm}^3$, $S_V^p = 24.13$ and $58.30 \text{ mm}^2/\text{mm}^3$ respectively for P6 and P7. As discussed in Chapter 2, a localized zone is seldom more than 4 grains wide, and since the areas covered by our mosaics were from 2 to 3 grains wide, we shall use a value of 3 times the grain size for the zone width. Since the average grain dimension of Westerly granite is .75 mm, we have $w \approx 2.25 \text{ mm}$. Substituting all these values into (6), we conclude that a reasonable estimate of a lower bound on M^1 is from 1.85×10^1 to $1.85 \times 10^2 \text{ Jm}^{-2}$ for P6, and 9.54×10^1 to $9.54 \times 10^2 \text{ Jm}^{-2}$ for P7 (Table IV and Figure 3).

In addition to the problem of resolving power of the SEM (which is limited to be above $.02\mu\text{m}$) the major source of error in the determination of both M and M^1 is from the

stereological procedures. When we counted the cracks, did we make the optimum choice of array spacing and angle increments to obtain a statistically meaningful sample of crack intersections? To what extent do the samples deviate from the type of symmetry in crack distribution we assumed? It is difficult at the present moment to precisely determine the error in these procedures on the basis of our limited experience with the stereological methods. Techniques exist for exploring these questions [Underwood, 1970], and it would be useful to investigate the problem more thoroughly in the future.

Seismologically inferred values

In the past decade, a number of studies have been made to determine \underline{G} from seismological data; these results are compiled in Table 1A for comparison.

In addition, we determine \underline{G} from McGarr et al.'s [1979] data on tremors in a deep gold mine (E.R.P.M.) of the Witwatersrand in South Africa. Equation (7) is used with $\alpha = 1$. We can estimate R and $\Delta\tau$ from two ways. Following Hussein et al.'s [1975] approach, and referring to Table 3 of McGarr et al. [1979], we get $R = 215$ m and $\Delta\tau = 75$ MPa solely on the basis of seismic data. On the other hand, if, as suggested by McGarr et al., we use the seismic moment and underground measurement of the average slip to infer R and $\Delta\tau$, we get $R = 48$ m and $\Delta\tau = 69.5$ MPa. Values of \underline{G} so determined by us from these two sets of estimates are included in Table 1A.

DISCUSSION

The role of microcracking in pre- and post-failure deformation

The data shown in the last two columns of Table III and IV confirm our suggestion earlier in the paper that the energy associated with microcracking (M and M^1) should represent a lower bound on the total energy input for pre-failure (W) and post-failure (G) deformation. Other than microcracking, processes such as frictional heating and acoustic emission may act as energy sinks. Our data also show that the ratio of M/W is significantly higher than M^1/G . Several factors may contribute to this difference. First, the location of the mosaics for the post-failure samples was deliberately chosen such that our estimates of S_V^P and S_V^f (equation (6)) would be lower and upper bounds respectively; therefore, our estimates are lower bounds on M^1 , whereas for the pre-failure sample, the estimate is a representative value for M as seen in the SEM. Second, the pressure and temperature were higher in P4-7, possibly resulting in relatively more energy dissipation by processes other than microcracking. Third, if the two effects above are not significant, then the variation is probably due to intrinsic difference between the energy budget for pre-failure deformation and that for post-failure deformation.

The closeness in values for the two energy terms in the pre-failure sample T5 indicates that most of the stress-induced cracks are resolvable under the SEM. It was concluded by Hadley [1976] that pre-existing voids in Westerly granite may be seriously underestimated with SEM observation. However, if the tip of a given crack has taken up an appreciable amount of the energy input, it results in both widening and extension of the crack. Such cracks are more readily observed under the SEM.

Although we conclude from our SEM observations (Chapter 2) that extensive microcracking is involved in the faulting process and that a large portion of the cracks are axial ones formed in tension, the tensile fracture energy measurements are not the appropriate values for characterizing the shear fault formation.

The data in Table IV show that for a sample that is only about one-third of the way into the post-failure region, the use of the tensile values would have underestimated the energy for microcracking alone by one to two orders of magnitude, depending on whether the single crystal or pre-cracked rock value is used. The pre-cracked rock tensile measurements are, of course, very useful for engineering applications such as hydraulic fracturing; our calculation here also shows that the use of single crystal tensile measurements to characterize cracks in a microscopic scale

gives results consistent with the constraints on energy dissipation placed by the macroscopic stress and strain.

Comparison of laboratory measurements and seismologically inferred values of the shear fracture energy G

Several aspects of the values of G compiled in Tables I and II are worth noting. First, the values from seismology (Table IA) can vary widely. For the 1966 Parkfield earthquake, which is unquestionably one of the best documented earthquakes, Hussein et al.'s [1976] estimate of G is $2.3 \times 10^3 \text{ Jm}^{-2}$, whereas Aki's [1980] estimate is $1.6 \times 10^6 \text{ Jm}^{-2}$. (We correct here a typographical error in the former paper which gives a low G value of one order of magnitude). Hussein et al. estimated the rupture area by corner frequency analysis, which involves considerable uncertainty. The limitation of this approach was discussed in some detail by Rice [1979]; Aki [1980] also argued that this approach is biased towards an underestimate. On the other hand, Aki's estimate of rupture area hinges on the assumption of the barrier model, and the high value may be a consequence of this assumption [Rudnicki, 1980].

Considerable discrepancy also exists between two estimates of G for the 1857 Fort Tejon earthquake. Aki [1979] determined G for this large earthquake to be $2 \times 10^6 \text{ Jm}^{-2}$, whereas Rudnicki's [1980] estimate is $3.8 \times 10^6 \text{ Jm}^{-2}$. As

discussed above, we calculated \underline{G} for seismic events in E.R.P.M., South Africa. The two estimates are $1.0 \times 10^3 \text{ Jm}^{-2}$ and $4.2 \times 10^6 \text{ Jm}^{-2}$ respectively (Table IA). This set of values is particularly interesting because the seismicity is not associated with pre-existing faults, and should, in this sense, be very similar to brittle fracture of intact samples in the laboratory (McGarr et al., 1979]. The country rock at E.R.P.M. is Witwatersrand quartzite. We determined \underline{G} from laboratory measurements of post-failure behavior presented by Spottiswoode [1980]. Using equation (2), values of \underline{G} for the quartzite from the post-failure curves are .8 and $1.3 \times 10^4 \text{ Jm}^{-2}$ respectively. The laboratory values fall between the two seismologically inferred values.

Second, the experimental values determined from post-failure curves (Table II) for both initially intact and pre-fractured samples are all of the order 10^4 Jm^{-2} . The shear \underline{G} value determined experimentally is therefore roughly two orders of magnitude higher than the tensile measurements. The former compares more favorably with the seismologically inferred values, but the discrepancy can still amount to three orders of magnitude.

Third, the room temperature laboratory \underline{G} measurements can be separated into two groups: Westerly and Oshima granite, and Witwatersrand quartzite have lower \underline{G} , whereas

the "softer" Fichtelgebirge granite tends to have significantly higher values. At comparative pressures, the latter can be higher by one order of magnitude; this may be indicative of the extent of variation with rock type to be expected of \underline{G} .

Fourth, for the same rock type (Westerly granite), the effect of pressure and temperature can increase \underline{G} by an order of magnitude. We plot all the data on Westerly at 80 MPa and 250 MPa in Figure 3 to illustrate the variation of \underline{G} with temperature. At 80 MPa, \underline{G} first increases with temperature and then decreases. At 250 MPa and temperatures above 350°C, the relative increase in slip and reduction in stress drop accompanying a temperature increase compensate for each other, so that \underline{G} as determined from the integral in (2) remains roughly constant. We want to point out, however, that (2) may not be applicable at temperatures above about 600°C. At 250 MPa, the fracture and frictional strength curves cross over at about 600°C (Chapter 1) and Stesky [1978] also reported that in faulted samples deformed at 250 MPa, a sharp increase in dislocation density was observed at about 500°C. We did not investigate the dislocation structures in our samples; if

extensive dislocation activities are involved, analyses of plastic instability such as that by Argon [1973] may be a more appropriate approach to take.

We have data at only two pressures, and it would be too speculative to generalize on pressure effects. As for the room temperature data, no systematic trend can be detected from Wawersik & Brace's [1971] data, although Rummel et al's [1978] results show a two-fold increase of \underline{G} from 55 MPa to 157 MPa, similiar to the increase with pressure in our 150°C data.

Fifth, if we try to determine \underline{G} from the post-creep failure curves with the assumption that localization occurs at the onset of tertiary creep and that equation (2) applies, then the \underline{G} values for the two creep specimens (PFW 17 and PFW 27) with different loading history (Chapter 1) agree quite well. The creep values are lower than that for PFW16 deformed at same temperature and pressure but at constant displacement rate. The first comparison is complicated by the uncertainty and arbitrariness usually associated with the location of the transition point from secondary to tertiary creep. The second comparison may not be appropriate because two different assumptions have been made concerning the point of localization for the two different types of loading.

CONCLUSION

In recent years, extensive work has been done on these four separate areas: the estimation of shear fracture energy from seismological data, the laboratory study of post-failure behavior in triaxial compression, the measurement of tensile fracture energy of single crystals, and the observation of stress-induced microstructures under the SEM. On the surface they seem to be unrelated. Our calculation above shows how from energetic considerations the four types of measurement can actually be related to one another.

Previous work has shown that quantitative information on the effects of cracks on physical quantities such as velocity [Hadley,1976] and permeability [Brace,1978] can be extracted from careful SEM observation. The present study shows that SEM observation is useful for the estimation of energy associated with the microcracking process. We also demonstrate the feasibility of a systematic application of stereological techniques for acquisition of reasonably accurate crack area data.

The fracture energy concept has long been proved to be a powerful tool in engineering fracture mechanics, and the potential for application of similar concepts to fault

mechanics is evident in the numerous recent attempts to use fracture mechanics in theoretical models. We conclude on the basis of our study of post-failure behavior (Chapter 1) that the variability of the load-displacement curve due to both loading history and statistical differences among specimens suggest the use of a global physical quantity such as \underline{G} for the characterization of post-failure behavior.

However, even in the laboratory context, there still exist several difficulties in applying the concept. For initially intact samples, the question of pre- versus post-failure localization has to be settled, and probably a better understanding of the "slip-weakening" process on a microscopic level is necessary before we can model the complex process better and obtain a more accurate estimate of \underline{G} . Rice's calculation shows that \underline{G} of a pre-fractured sample is of the same order as that of an initially intact sample. However, it is only fair to say that unlike the case of post-failure behavior of initially unfractured rock, the dependence of details of frictional behavior on testing machine characteristics and the relationship of stick-slip with respect to machine stiffness are questions not fully understood [Byerlee & Brace, 1968; Ohnaka, 1975; Ida, 1975; Goodman & Sundaram, 1978]. The principal problem for application of Rice's theory to

pre-fractured samples may, therefore, not lie with the location of the first integration limit in (2) (the point of localization) but with the second limit, namely, the question of whether the sample has "overshot" and what the residual stress level should be.

Nevertheless, an estimate of the fracture energy under shear in a triaxial configuration is clearly more realistic for fault mechanics application than values measured in a tensile mode. That the laboratory \underline{G} measurements in shear agree more favorably with seismologically inferred values than the tensile measurements is encouraging. The data compiled by us show that the effects of temperature and pressure, and different rock types can change \underline{G} by an order of magnitude. It will be useful to investigate this in greater detail and see to what extent we can generalize the effect of pressure and temperature to pre-fractured samples and over a broad range of rock types. To what extent these data can be applied to field situations of course still hinges on a better understanding of the important problem of scaling.

APPENDIX

A summary of useful stereological concepts

Our scheme involves three steps: (1) A set of parallel lines at fixed angles (θ) to the maximum compression (σ_1) direction, called a test array, is placed on a photo-mosaic taken under the SEM. The number of intersection points of the test array with cracks is counted and the average number per unit length (P_L) is obtained. (2) From orientation dependence of the measurements (i.e. P_L as a function of θ), one tries to estimate the average length of crack per unit area (L_A) as seen on the mosaic. (3) On the basis of symmetry in the macroscopic strain field, one then tries to relate L_A to the crack surface per unit volume (S_V). Details of the procedure for step 1 has been described in Chapter 2; the data of $P_L(\theta)$ for three pre-failure samples and two post-failure samples are compiled in Table IV.

A general analysis of the problem in step 2 was presented by Hilliard [Hilliard, 1962; Philofsky & Hilliard, 1969; Hilliard 1967]. By simple geometric argument, it can be seen that for a crack at an angle θ to σ_1 , the number of intersections with a test array at angle ω to σ_3 ($(\pi/2 - \omega)$ to σ_1) should be proportional to $\cos(\theta - \omega)$: when $\theta = \omega$, the test array is perpendicular to the crack and therefore makes the maximum number of intersections, whereas when $\theta = \omega + \pi/2$, they are parallel and no intersection is possible. Therefore,

$$P_L(\omega) = \int_{\omega-\pi/2}^{\omega+\pi/2} L_A(\theta) \cos(\theta-\omega) d\theta \quad (\text{A1})$$

or in a differential form:

$$L_A(\theta) = 1/2 \left(P_L + \frac{d^2 P_L}{d\omega^2} \right) \Big|_{\omega=\theta+\pi/2} \quad (\text{A2})$$

The total crack length per unit area is then given by

$$L_A = \int_0^\pi L_A(\theta) d\theta$$

Several features of the above relations are worth noting. First, it is not practical to try to obtain a detailed description of L_A as a function of θ . Two approaches have been suggested: one can either solve (A2) as a difference equation, or fit the $P_L(\theta)$ measurements to a Fourier series and solve for $L_A(\omega)$ in term of the Fourier coefficients. (The latter approach can actually be generalized to determine S_V directly in term of spherical harmonics). Both approaches demand an enormous amount of counting at small increments of ω for a reasonable degree of accuracy. Second, a number of studies [e.g. Wawersik & Brace, 1971; Kranz, 1979; Kranz 1980] estimated crack orientation distribution by measuring the angles of cracks encountered in a single set of traverses placed perpendicular to σ_1 ; such a procedure systematically biases towards cracks at high angle to σ_1 and thereby exaggerates the degree of anisotropy. Third, L_A can easily be determined for certain simple cases of high symmetry. If the cracks have only one preferred orientation, we have

$$P_L(\theta) = a + b \sin\theta \quad (\text{A3})$$

where θ is the angle between the preferred orientation and the test array. The first term (the constant a) represents a system of randomly oriented cracks and the second those at the preferred orientation. If the array is placed first parallel and then perpendicular to the preferred orientation, with the number of intersections given by P_L^{\parallel} and P_L^{\perp} , then it can be shown that [Underwood, 1970]:

$$a = P_L^{\parallel}, \quad b = P_L^{\perp} - P_L^{\parallel}$$

and
$$L_A = P_L^{\perp} + (\pi/2 - 1)P_L^{\parallel} \quad (\text{A4})$$

A measure of the degree of anisotropy for such an oriented structure is given by

$$\Omega_{12} = \frac{P_L^{\perp} - P_L^{\parallel}}{P_L^{\perp} + (\pi/2 - 1)P_L^{\parallel}} \quad (\text{A5})$$

If the sample has axisymmetry, and if P_L^{\perp} and P_L^{\parallel} are obtained in a plane section passing through the axis of symmetry, then an estimate of crack surface per unit volume is

$$S_V = \pi/2 P_L^{\perp} + (2 - 2/\pi)P_L^{\parallel} \quad (\text{A6})$$

The "roses" for the data of three pre-failure samples deformed close to fracture at different temperatures and pressures are plotted in Figure 4, with σ_1 taken as the preferred orientation. There seems to be no systematic trend for $P_L(\theta)$ to be higher or lower than $P_L(\pi - \theta)$ (Table V); to reduce the scatter, we averaged the two values and plot

the rose from 0° to 90° only. The data were least-square fitted to an equation of the form (A3), and the theoretical curves are included in the figure. Considering the scatter in the measurements, the agreement is quite good. Hence for a pre-failure sample, the crack distribution can for most purposes be approximately represented as an axisymmetric one with a single preferred orientation parallel to σ_1 ; to estimate S_V , (A6) is the appropriate relation to use.

The situation for the post-failure samples is more complicated. As Figure 5 shows, there appears to be a systematic trend for one side of the "rose" to be larger. Because the cracks are longer and more numerous in these samples, the scatter is less. Compared with (A3), a better fit can be obtained by using two preferred orientation:

$$P_L(\theta) = a + b \sin\theta + c \sin|\theta - \omega| \quad (A7)$$

where $\omega = 30^\circ$ and 20° were respectively the angles between the localized zone and σ_1 as seen on the mosaics for the two samples. Both theoretical curves for (A3) and (A7) are shown in Figure 5 for comparison. Note that the estimate L_A is not sensitive to the assumptions of preferred orientations; if we assume one preferred orientation, L_A equals 15.7 and 24.2 mm/mm^2 , whereas if we assume two, the values are 15.9 and 24.1 mm/mm^2 respectively. The second set of values will be used for the calculation of S_V .

Localization in a post-failure sample results in azimuthal variation in strain and renders axisymmetry to be no longer valid; (A6) is therefore not applicable for the evaluation of S_V . For a planar structure such as the localized zone, if we assume the variation in a direction parallel to σ_2 is small, then L_A measured on a random section perpendicular to the localized zone will be related to S_V simply by [Underwood,1970]:

$$S_V = L_A \quad (A7).$$

TABLE I

Fracture energy, G

A. Seismological estimate

G (Jm^{-2})	Method	Reference
10^7	From rupture propagation time	Takeuchi & Kikuchi [1973]
10^7	From strong motion data (maximum velocity and acceleration)	Ida [1973]
10^2	From spatial distribution of slip during fault creep estimated from data of King, Nason & Tocher [1973]	Rice & Simons [1976]
10^1 - 10^4 "frictional"	From stress drop and fault dimension	Husseini et al. [1976]
10^4 - 10^5 "fresh fracture"		
10^6 - 10^8	From rupture velocity; based on barrier model	Das [1976]
10^6 - 10^8	From stress drop and fault dimension estimated from strong motion data, spatial distribution of after-shocks, and geologic evidence	Aki [1979]
10^6	From geodetic data and earthquake recurrence rate for San Andreas	Rudnicki [1980]
10^3	From McGarr et al.'s [1979] seismic data for a South African gold mine	This study
10^6	From McGarr et al.'s [1979] determination of seismic moment and underground measurement of average slip	This study

B. Laboratory: Tension

1-10	Single crystals under tension	Brace & Walsh [1962]
10 - 10^2	Pre-cracked rock samples under tension	Atkinson [1979]

TABLE II

Laboratory Measurement of Shear Fracture Energy G

Sample	σ_3 (MPa)	T (°C)	Fracture angle	$\frac{G}{10^4 \text{ Jm}^{-2}}$	$\tau^p - \tau^f$ (GPa)	$\frac{\Delta u}{\Delta l}$ (mm)	ω^e (m°)	Reference
<i>Fichtelgebirge granite</i>								
	470	room	36°*	4.5 #	.13	.34	.18	Rummel et al (1978)
	55	room	"	4.7	.11	.44	.29	" "
	300	room	"	7.3	.15	.49	.24	" "
<i>Witwatersrand quartzite</i>								
	14	room	25°*	0.8	.05	.15	.21	Spottiswoode (1980)
	28	room	"	1.3	.08	.16	.14	" "
<i>Oshima granite</i>								
452	room	room	25°*	1.0	.06	.17	.20	Sano (1978)
<i>Westerly granite</i>								
	room	room	25°*	.7	.08	.09	.08	Wawersik & Brace (1971)
	room	room	"	.8	.08	.10	.09	" "
	20	room	"	.6	.10	.06	.04	" "
	20	room	"	.8	.11	.07	.05	" "
	80	room	"	.3	.08	.04	.04	" "
	80	room	"	.7	.10	.07	.05	" "

Sample	σ_3 (MPa)	T (°C)	Fracture angle	G (10^4 Jm^{-2})	$\tau^p - \tau^f$ (GPa)	$\overline{\Delta u}$ (mm)	ω_o^e (m)	Reference
<i>Westerly granite</i>								
PFW22	80	150	25°	3.3	.14	.24	.12	This study
PFW23	80	350	31°	2.3	.10	.23	.16	"
PFW13	250	150	30°	5.1	.15	.34	.16	"
PFW16	250	350	31°	2.2	.10	.22	.15	"
PFW17 [§]	250	350	30°	1.7	.08	.22	.19	"
PFW27 [§]	250	350	32°	1.3	.07	.19	.19	"
MTW 7	250	550	34°	2.3	.09	.26	.21	"
MTW 8	250	668	38°	2.3	.05	.45	.64	"

@ Calculated with the following input values: $\nu = .25$ and $\mu = 30$ GPa.

* Fracture angles assumed.

Polished sawcut sample.

§ Calculated from post-creep failure curve.

TABLE III

Crack density data of Westerly granite at 50 MPa, room pressure

Sample	$P_L^I, /mm^*$	$P_L^{II}, /mm^*$	$S_V, mm^2/mm^3 \#$	$M, 10^4 Jm^{-3} @$	$W, 10^4 Jm^{-3} @$	Comments
T0	4.82	4.91	9.68	0	0	Virgin sample
T5	8.85	5.71	16.35	.67 - 6.67	5 ± 3	Sample retrieved just before failure

* Data of Tapponier & Brace [1976]

Calculated from equation (A6)

@ Calculated from equations (5) and (1) respectively

TABLE IV

Crack density data of Westerly granite at 250 MPa, 150°C

Sample	L*, mm	$P_L(\theta)$, /mm	S_V , mm ² /mm ³ §	M^1 , 10 ² Jm ⁻² §	\underline{G} , 10 ³ Jm ⁻² #
P4	65	$7.95 + 2.30\sin\theta + 1.12\sin \theta - 30^\circ $	15.91	0	0
P6	100	$9.22 + 4.89\sin\theta + 4.76\sin \theta - 20^\circ $	24.13	.19-1.85	2.7
P7	24	$19.29 + 28.00\sin\theta$	58.30	.95-9.54	7.4

* Total length of test array. Magnification of the mosaics were 300X, and the spacing between adjacent traverses was 33µm

Calculated from equation (2) with fracture angle 30°. \underline{G} estimated from the complete post-failure curve was $5.1 \times 10^4 \text{ Jm}^{-2}$

§ Calculated from equations (A7) and (6) respectively

TABLE V

Orientation dependence of crack intersections per unit length

Sample	T, °C	σ_3 , MPa	$\sigma_1 - \sigma_3$, GPa	θ^*	$P_L(\theta)$, /mm
T8	23	50	0.53	0°	2.81
				15°	2.68
				30°	2.70
				45°	3.02
				60°	3.43
				75°	3.67
				90°	3.85
				105°	3.37
				120°	3.74
				135°	3.16
				150°	3.05
				165°	3.04
				P3	153
15°	4.66				
30°	4.93				
45°	5.07				
60°	5.43				
75°	5.50				
90°	5.71				
105°	5.31				
120°	4.91				
135°	4.71				
150°	4.91				
165°	4.46				
H3	355	400	1.50		
				15°	6.50
				30°	7.65
				45°	7.94
				60°	7.73
				75°	7.89
				90°	8.02

Sample	T, °C	σ_3 , MPa	$\sigma_1 - \sigma_3$, GPa	θ^*	$P_L(\theta)$, /mm
H3				105°	7.51
				120°	7.99
				135°	8.26
				150°	8.07
				165°	6.98
P4	150	250	1.22	0°	8.51
				15°	8.84
				30°	8.22
				45°	10.05
				60°	10.99
				75°	11.35
				90°	11.34
				105°	11.27
				120°	10.85
				135°	9.60
				150°	9.49
P6	151	250	1.15	0°	11.60
				15°	11.72
				30°	11.82
				45°	14.58
				60°	17.82
				75°	18.57
				90°	19.01
				105°	18.37
				120°	16.35
				135°	15.16
				150°	14.63
P7	151	250	1.10	0°	19.29
				90°	47.29

*Angle between the test array and maximum compression (σ_1)

FIGURE CAPTIONS

Figure 1: (a) Localization of an initially intact sample stressed triaxially.

(b) & (c) Transformation of post-failure data (of Westerly granite at 80 MPa, room temperature) to infer shear stress versus relative slip relation used in "slip-weakening" model. The dash-dotted line marked "T" in (c) shows the transition slope from class I to class II behavior.

Figure 2: Slip-weakening model as applied in field and in laboratory. The distribution of shear stress (τ) and slip displacement ($\Delta\mu$) with respect to a fault in the field is shown. The breakdown zone size w_0 is also indicated.

Figure 3: Variation of shear fracture energy \underline{G} with temperature at constant pressures of 80 MPa and 250 MPa. Bars are shown indicating estimated uncertainty in \underline{G} and temperature measurements. Values of \underline{G} and M^1 of the two post-failure samples P6 and P7 are also shown for comparison.

Figure 4: Roses of the number of crack intersections per unit length for three pre-failure samples. The least square fit of the data to equation (A3) is also shown as a continuous dashed curve.

Figure 5: Roses of the number of crack intersections per unit length for two post-failure samples. The continuous dark and dashed curves show the theoretical prediction based on equations (A7) and (A3) respectively.

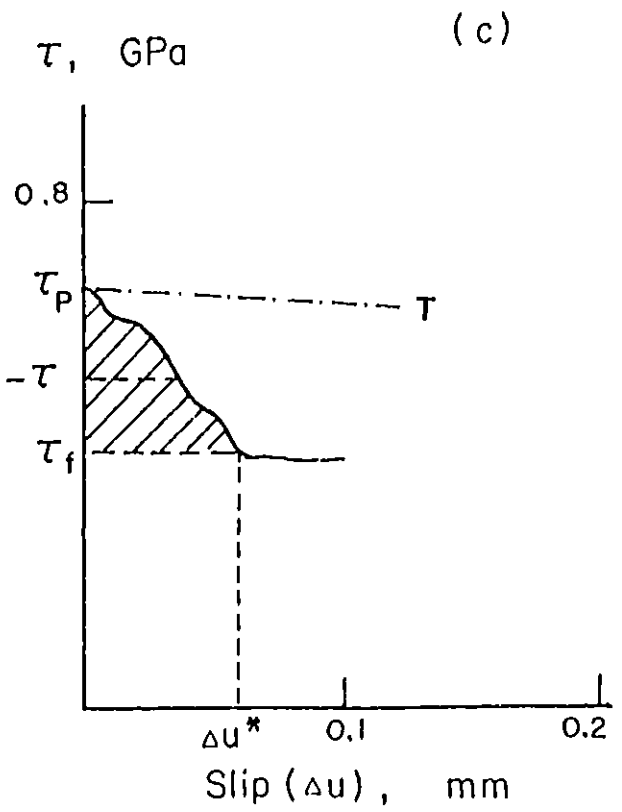
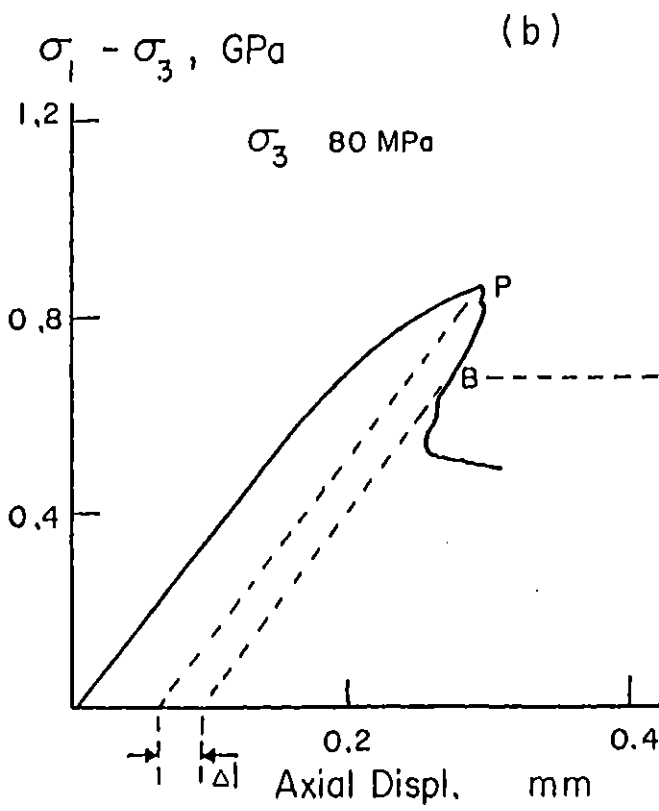
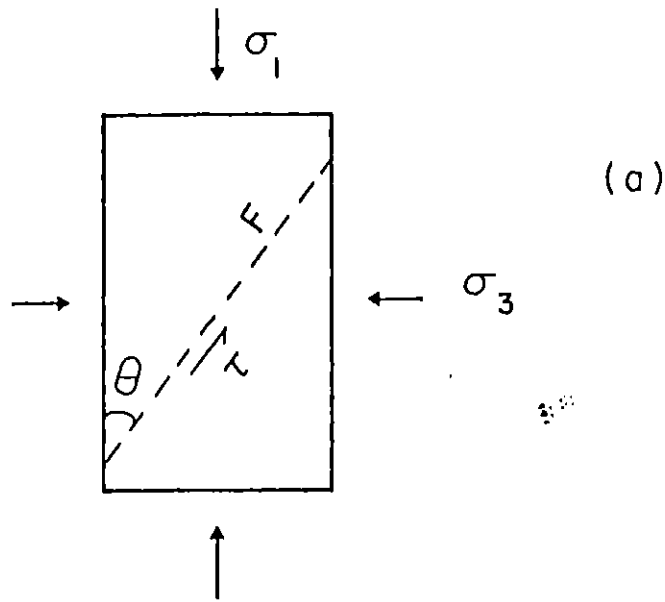
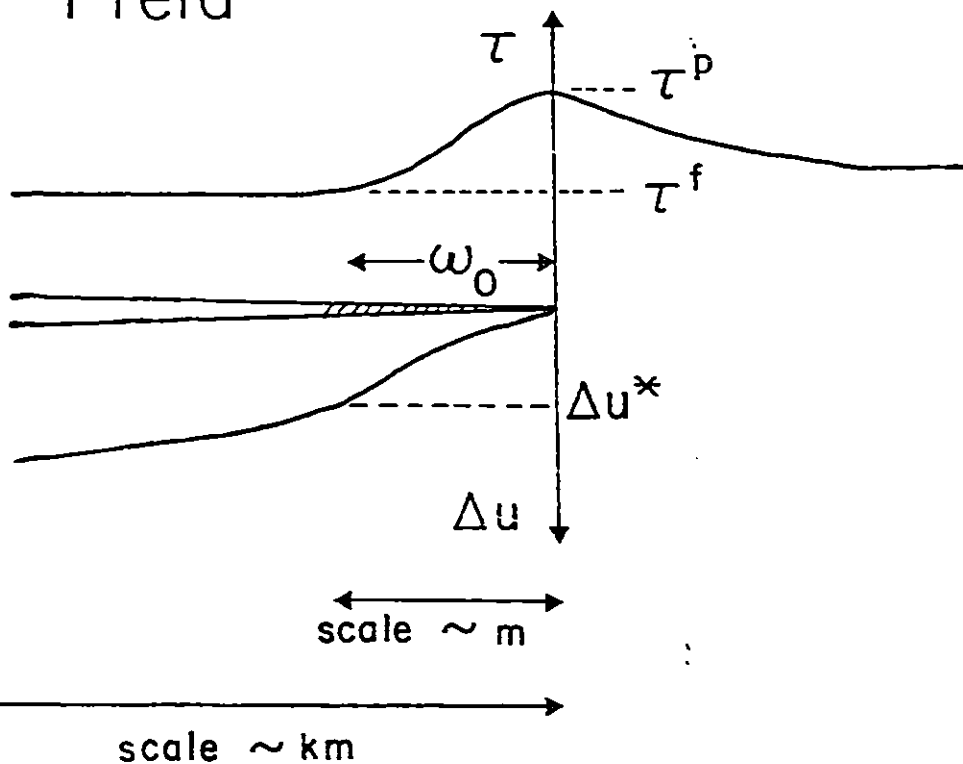
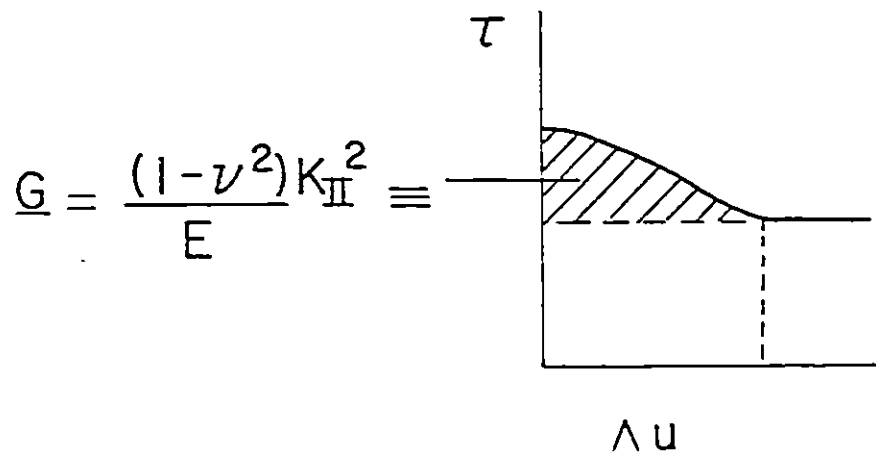
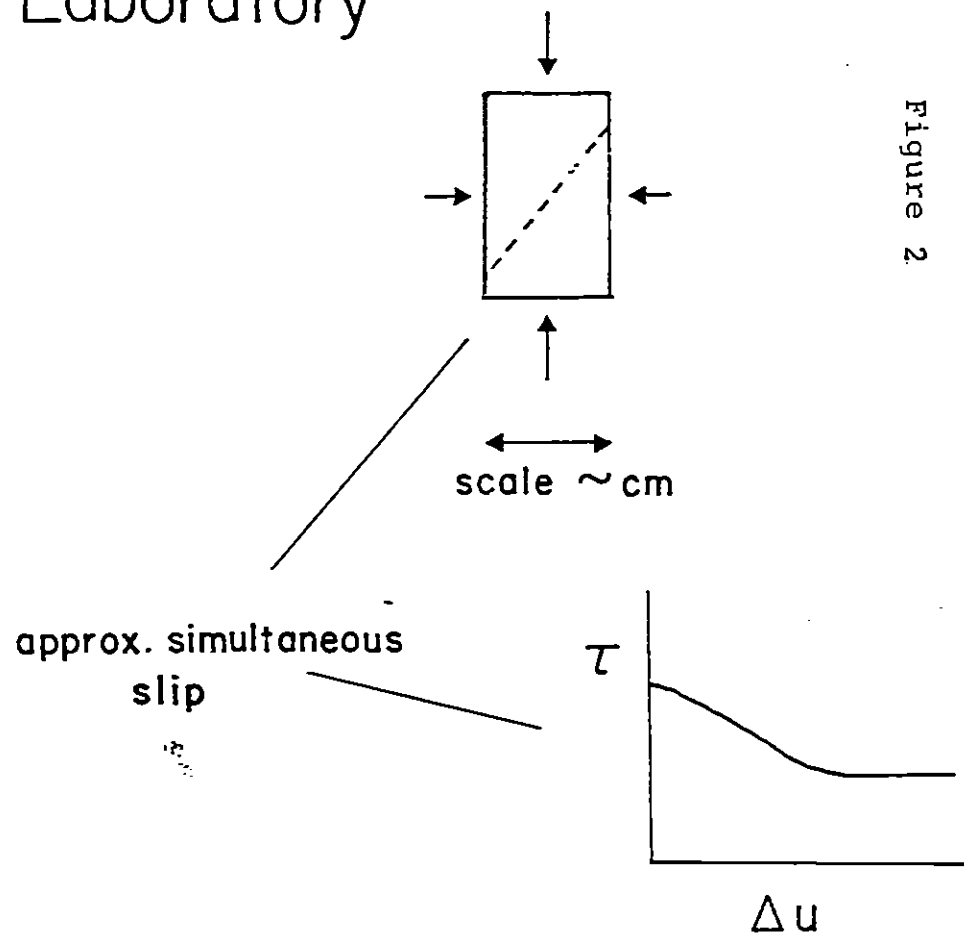


Figure 2

Field



Laboratory



ASSUMPTION:
Relation between shear stress (τ) and slip displacement (Δu) in laboratory same as in field

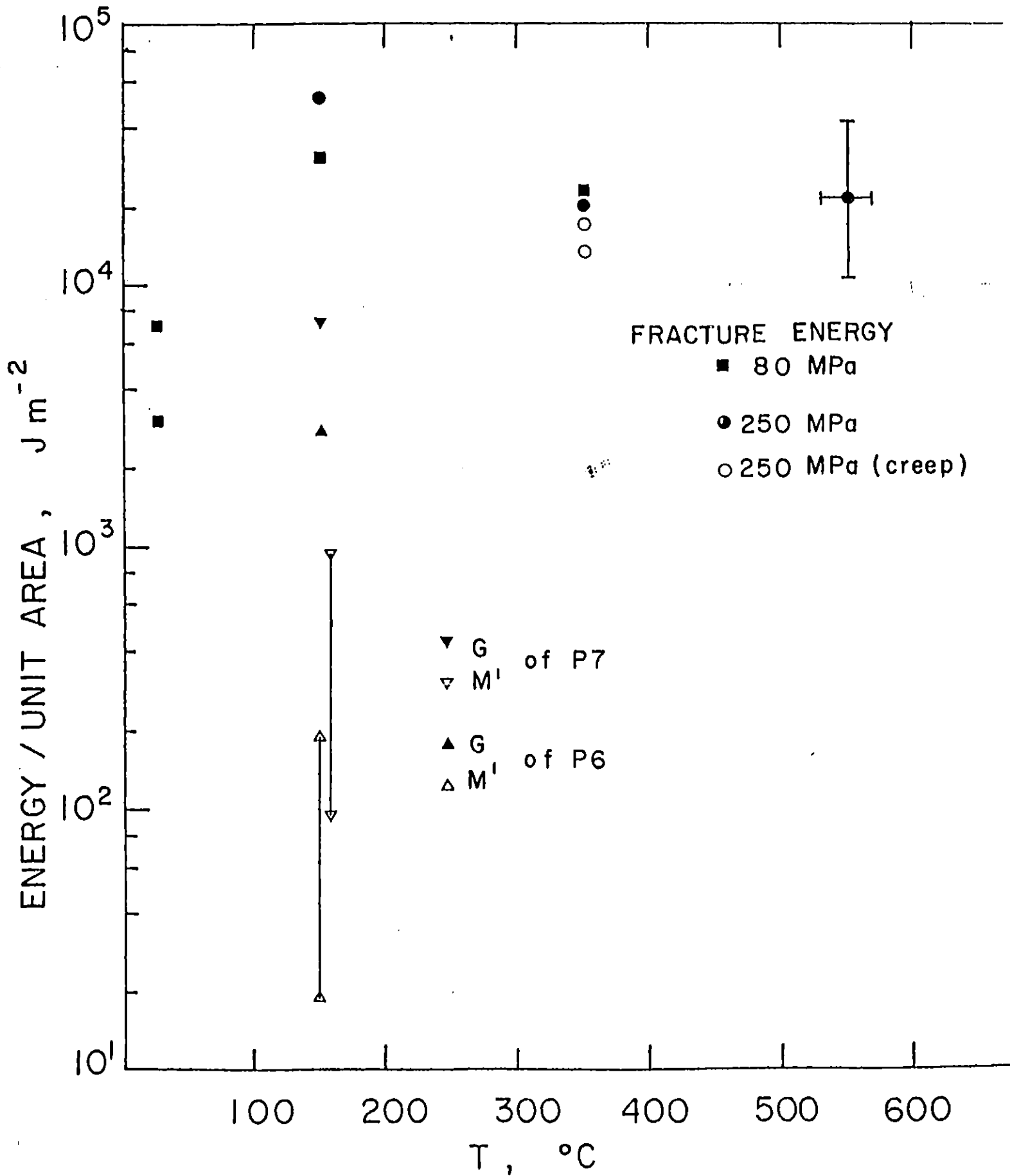


Figure 4

$R_L(\theta)$, /mm

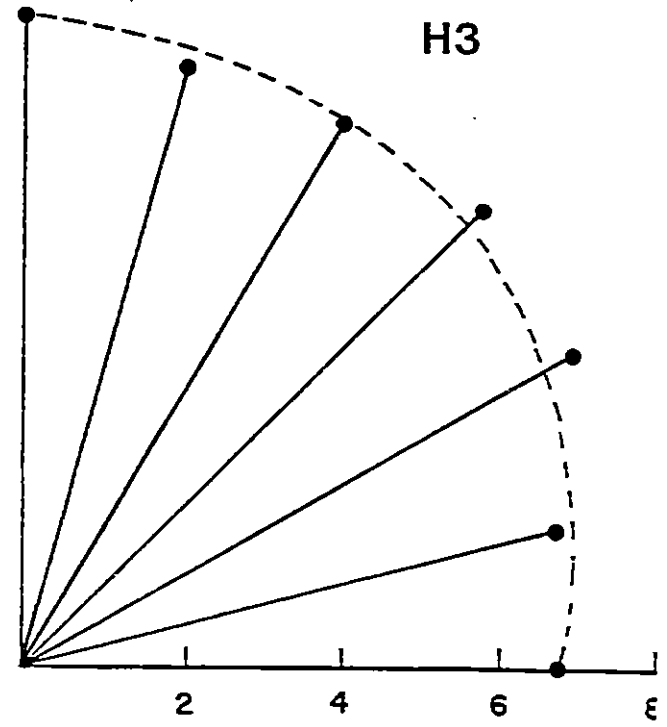
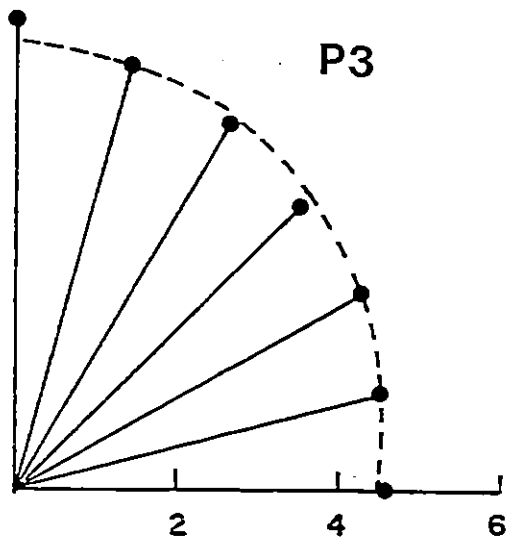
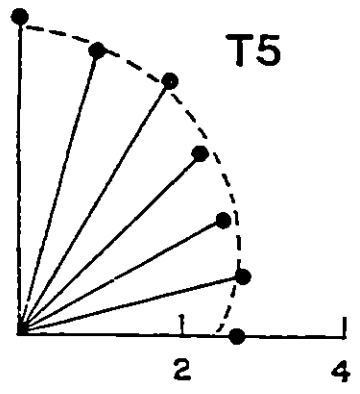
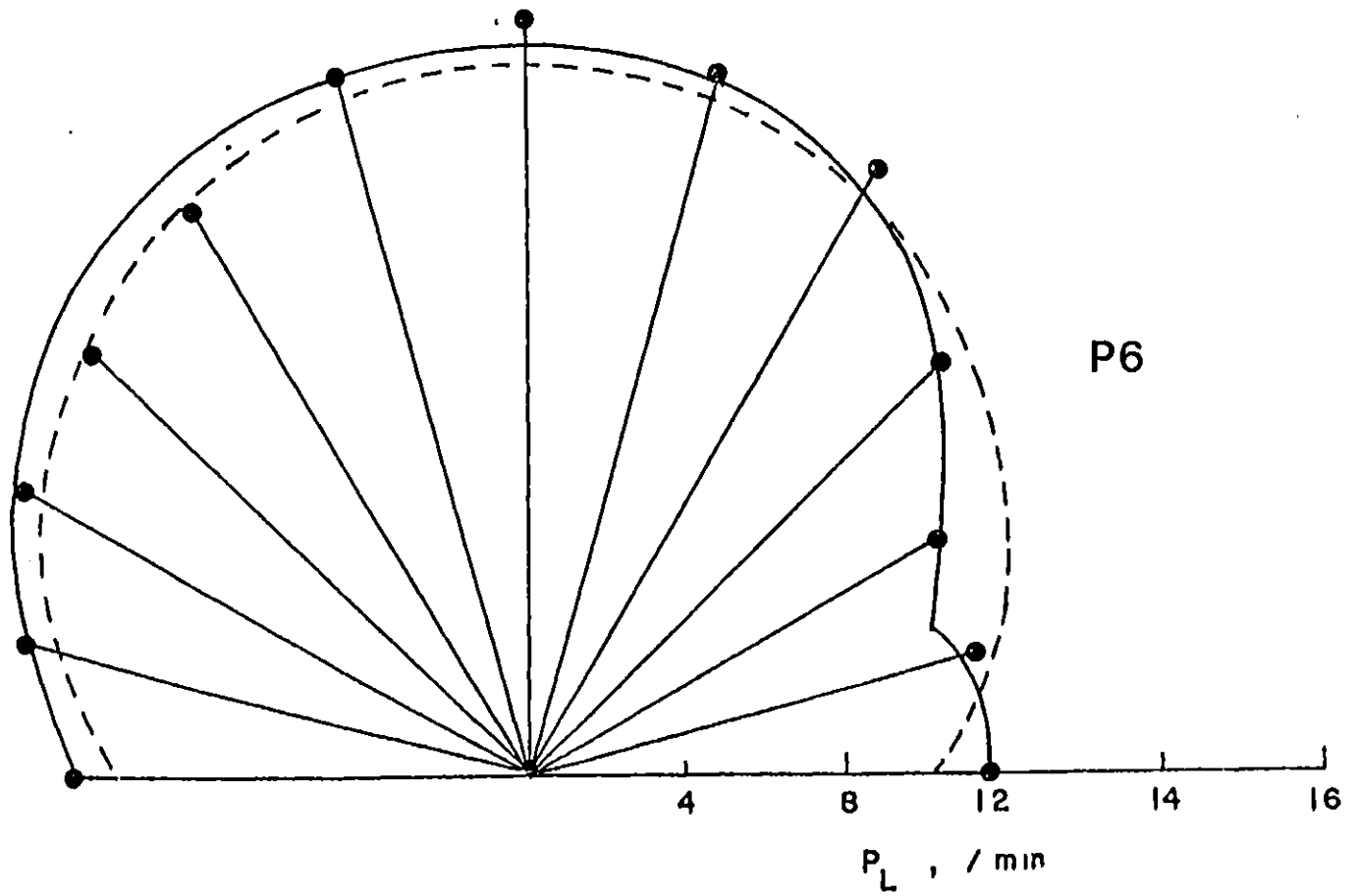
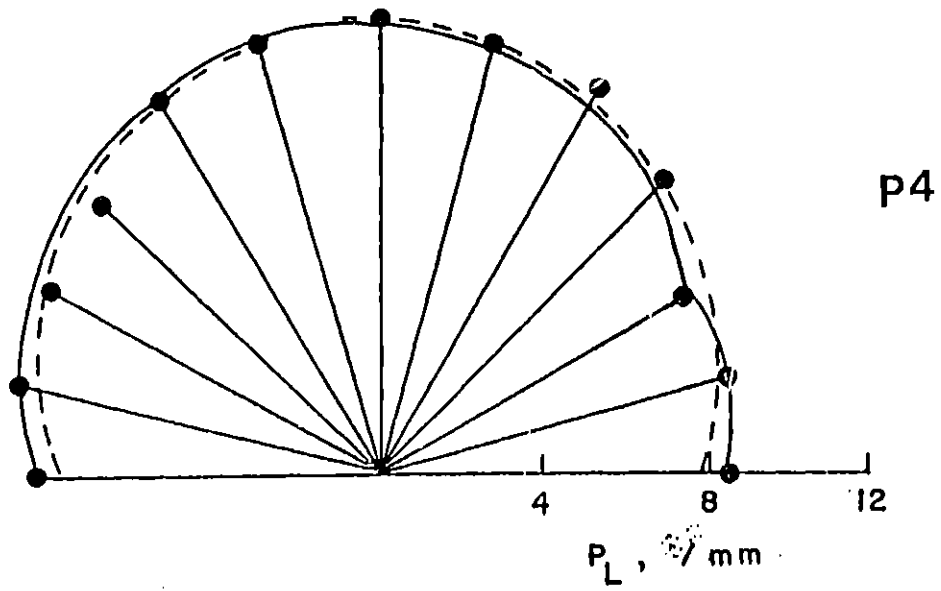


Figure 5



REFERENCES

- Aki, K., Characterization of barriers on an earthquake fault, J. Geophys. Res., 84, 6140-6148, 1979.
- Aki, K., and P.G. Richards, Quantitative Seismology, W.H. Freeman & Co., San Francisco, 1980.
- Argon, A.S., Stability of plastic deformation, in The Inhomogeneity of Plastic Deformation, A.S.M., 1973.
- Atkinson, B.K., Compilation of Experimentally Determined Fracture Mechanics Parameters for Geological Materials, Final Technical Report to U.S. Natl. Earthquake Hazards Reduction Program, 1979.
- Barenblatt, G.I., The mathematical theory of equilibrium cracks in brittle fracture, Adv. Appl. Mech., 7, 55-129, 1962.
- Brace, W.F., B. Paulding, and C.H. Scholz, Dilatancy in the fracture of crystalline rocks, J. Geophys. Res., 71, 3939-3954, 1966.
- Brace, W.F., Permeability from resistivity and pore shape, J. Geophys. Res., 82, 3343-3349, 1977.
- Brace, W.F., and J.B. Walsh, Some direct measurements of the surface energy of quartz and orthoclase, Amer. Mineral., 47, 1111-1122, 1962.
- Brune, J.N., Tectonic stress and the spectra of seismic shear waves from earthquakes, J. Geophys. Res., 75, 4997-5009, 1970.
- Brune, J.N., Corrections to J. Geophys. Res., 75, 4997-5009, 1970 - J. Geophys. Res., 76, 5002, 1971.
- Byerlee, J.D., Theory of friction based on brittle fracture, J. Appl. Phys., 38, 2928-2934, 1967.

- Byerlee, J.D., and W.F. Brace, Stick-slip, stable sliding and earthquakes - effect of rock type, pressure, strain rate, and stiffness, J. Geophys. Res., 73, 6031-6037, 1968.
- Das, S., A numerical study of rupture propagation and earthquake source mechanism, Ph.D. thesis, M.I.T., 1976.
- Freiman, S.W., Fracture Mechanics Applied to Brittle Materials, A.S.T.M., STP678, 1979.
- Freund, L.B., The mechanics of dynamic shear crack propagation, J. Geophys. Res., 84, 2199-2209, 1979.
- Friedman, M., J. Handin, and G. Alani, Fracture surface energy of rocks, Int. J. Rock Mech. Min. Sci., 9, 757-766, 1972.
- Goodman, R.E., and P.N. Sundaram, Fault and system stiffness and stick slip phenomena, PAGEOPH, 116, 873-887, 1978.
- Hadley, K., Comparison of calculated and observed crack densities and seismic velocities in Westerly granite, J. Geophys. Res., 81, 3484-3494, 1976.
- Hallbauer, D.K., H. Wagner, and N.G.W. Cook, Some observations concerning the microscopic and mechanical behavior of quartzite specimens in stiff, triaxial compression tests, Int. J. Rock Mech. Min. Sci., 10, 713-726, 1973.
- Hilliard, J.E., Specification and measurement of microstructural anisotropy, Trans. AIME, 224, 1201-1211, 1962.
- Hilliard, J.E., Determination of structural anisotropy, in Proc. 2nd Intl. Congress for Stereology, Chicago, 219-227, 1967.
- Hudson, J.A., E.T. Brown, and C. Fairhurst, Optimizing the control of rock failure in servo-controlled laboratory tests, Rock Mech., 3, 217-224, 1971.

- Husseini, M.I., D.B. Jovanovich, M.J. Randall, and L.B. Freund,
The fracture energy of earthquakes, Geophys. J. Roy. Astr.
Soc., 43, 367-385, 1975.
- Husseini, M.I., D.B. Jovanovich, and M.J. Randall, Fracture
energy and aftershocks, Geophys. J. Roy. Astr. Soc., 45,
393-406, 1976.
- Ida, Y., Cohesive force across the tip of a longitudinal
shear crack and Griffith's specific surface energy,
J. Geophys. Res., 77, 3796-3805, 1972.
- Ida, Y., The maximum acceleration of seismic ground motion,
Bull. Seismol. Soc. Amer., 63, 959-968, 1973.
- Ida, Y., Analysis of stick slip and earthquake mechanism,
Phys. Earth Plan. Int., 11, 147-156, 1975.
- Kendall, M.G., and P.A.P. Moran, Geometric Probability, Charles
Griffin & Co., London, 1963.
- Kranz, R.L., Crack growth and development during creep in
Barre granite, Int. J. Rock Mech. Min. Sci., 16, 23-36, 1979.
- Kranz, R.L., The effects of confining pressure and stress
difference on static fatigue of granite, J. Geophys. Res.,
85, 1854-1866, 1980.
- Lockner, D.A., and J.D. Byerlee, Microfracturing and velocity
changes during creep in granite, EOS Trans. Amer. Geophys.
Un., 59, 1207, 1978.
- McGarr, A., S.M. Spottiswoode, N.C. Gay, and W.D. Ortlepp,
Observations relevant to seismic driving stress, stress
drop, and efficiency, J. Geophys. Res., 84, 2251-2261, 1979.
- Ohnaka, M., Frictional characteristics of typical rocks,
J. Phys. Earth, 23, 87-112, 1975.

- Palmer, A.C., and J.R. Rice, The growth of slip surfaces in the progressive failure of over-consolidated clay, Proc. Roy. Soc. London, A332, 527-548, 1973.
- Philofsky, E.M., and J.E. Hilliard, On the measurement of the orientation distribution of lineal and areal arrays, Quart. App. Math., 27, 79-86, 1969.
- Rice, J.R., A path independent integral and the approximate analysis of strain concentration by notches and cracks, J. App. Mech., 35, 379-386, 1968.
- Rice, J.R., The mechanics of earthquake rupture, in Proc. Intl. School of Physics "Enrico Fermi", Course LXXVIII on Physics of The Earth's Interior, E. Boschi editor, 1979.
- Rice, J.R., and D.A. Simons, The stabilization of spreading shear faults by coupled deformation-diffusion effects in fluid-infiltrated porous materials, J. Geophys. Res., 81, 5322-5334, 1976.
- Rudnicki, J.W., Fracture mechanics applied to the earth's crust, Ann. Rev. Earth Pl. Sci., 8, 489-525, 1980.
- Rummel, F., H.J. Alheid and C. Frohn, Dilatancy and fracture-induced velocity changes in rock and their relation to frictional sliding, PAGEOGH, 116, 743-764, 1978.
- Sano, O., Fundamental study on the mechanisms of brittle fracture of rocks, D. Eng. thesis, Kyoto Univ., 1978.
- Soga, N., H. Mizutani, H. Spetzler, and R.J. Martin III, The effect of dilatancy on velocity anisotropy in Westerly granite, J. Geophys. Res., 83, 4451-4458, 1978.

- Spottiswoode, S.M., Fault gouge, driving stress, and seismic efficiency, submitted to J. Geophys. Res., 1980.
- Stesky, R.M., Mechanism of high temperature frictional sliding in Westerly granite, Can. J. Earth Sci., 15, 361-375, 1978.
- Takeuchi, H., and M. Kikuchi, A dynamical model of crack propagation, J. Phys. Earth, 21, 27-37, 1973.
- Tapponnier, P., and W.F. Brace, Development of stress-induced microcracks in Westerly granite, Int. J. Rock Mech. Min. Sci., 13, 103-112, 1976.
- Underwood, E.E., Quantitative Stereology, Addison-Wesley, Reading, 1970.
- Wawersik, W.R., and W.F. Brace, Post-failure behavior of a granite and a diabase, Rock Mech., 3, 61-85, 1971.

BIOGRAPHICAL NOTE

I was born to Yue-fan and Oi-lan Wong on May 4, 1952 in Macao. I attended primary and secondary school in Hong Kong. In August, 1970 I came to the United States and received my undergraduate education at Brown University, majoring in Applied Mathematics. I subsequently obtained a Master of Science degree in Applied Mechanics from Harvard University. From 1976 to 1980, I was in the Department of Earth and Planetary Sciences, M.I.T., studying experimental rock mechanics under Professor W.F. Brace.